BIOPHYSICAL CHARACTERIZATION OF P22 BACTERIOPHAGE AND ADENOASSOCIATED VIRUSES

by

Ravi Kant

A dissertation submitted in partial fulfillment
of the requirements for the degree

of

Doctor of Philosophy

in

Biochemistry

MONTANA STATE UNIVERSITY
Bozeman, Montana

May, 2016

©COPYRIGHT

by

Ravi Kant

2016

All Rights Reserved

DEDICATION

This work is dedicated to my dearest wife Pooja Chaudhary, my little princess Dhriti Chaudhary and my parents for their constant support.

ACKNOWLEDGEMENTS

I would like to express my deep and sincere gratitude to my advisor, Dr. Brian Bothner, whose continuous support, guidance and unfaltering encouragement made my thesis work possible. He always gave me intellectual freedom in my work and engaged me in diverse exciting projects during my PhD tenure. I have been extremely fortunate to have a mentor who has always shown keen interest in my work and has always been available to advise me. I am also thankful to him for helping me understand viral dynamics and mass spectrometry and enrich my ideas.

I would also like to acknowledge my graduate committee members, Dr. Valerie Copie, Dr. Blake Wiedenheft, Dr. Jennifer Dubois for research guidance and scientific collaborations. I am also thankful to all the faculty, staff and students of Montana State University with whom I have worked during my time here. I expand my thanks to Dr Trevor Douglas, Dr. Mavis Agbandje-McKenna for providing me virus samples and their scientific expertise. Additionally, I would like to thank Dr. Jonathan Hilmer and Jesse Thomas for mentoring me in the use of the mass spec facility.

I would like to express my heart-felt gratitude to my parents, wife, daughter and family for their constant source of love, concern, support and strength all these years.

TABLE OF CONTENTS

1. INTRODUCTION 1

Maturation in Icosahedral Viruses 3
Maturation in HK97 Bacteriophage 4
Maturation in P22 Bacteriophage 6
Methods for Studying Viruses in Solutions 8
Differential Scanning Fluorimetry (DSF) 8
Circular Dichroism (CD) 10
Hydrogen Deuterium Exchange Mass Spectrometry (HDX-MS) 10
Atomic Force Microscopy (AFM) 13
Quartz Crystal Microbalance with Dissipation (QCMD) 15
Summary 17
References 18

2. STABILITY, BIOMECHANICS AND STRUCTURAL CHANGES IN P22 BACTERIOPHAGE DURING MATURATION 23

Contribution of Authors and Co-Authors 23
Manuscript Information Page 24
Abstract 25
Introduction 26
Materials and Methods 30
Protein Purification of WT P22 30
Differential Scanning Fluorescence (DSF) 31
Circular Dichroic Spectroscopy (CD) 32
AFM Experiments 33
Hydrogen Deuterium Exchange Mass Spectrometry (HDX-MS) 34
Calculation of Solvent Excluded Surface Area 35
Results and Discussion 36
Differential Scanning Fluorescence Reveals Heat Triggered Structural Transitions 36
pH Affects Thermal Structural Transitions 39
Maturation Increases Resistance to Denature 42
Circular Dichroism is Inconsistent with Refolding during Maturation 45
AFM Analysis of the Mechanical Properties of P22 46
Hydrogen-Deuterium Exchange of P22 Capsids 49
Maturation Increases Solvent Excluded Area 51
Maturation Leads to a Decrease in Free Energy by Enhancing Quaternary Interactions 54
Conclusions 58
References 60

TABLE OF CONTENTS-CONTINUED

3. UNDERSTANDING OF P22 BACTERIOPHAGE MATURATION BY QCM-D 66

Contribution of Authors and Co-Authors 66
Manuscript Information Page 67
Abstract 68
Introduction 68
Materials and Methods 73
Protein Purification of WT P22 73
QCM-D Experiment 74
Viscoelastic Modeling 74
Results and Discussion 75
Capsid Rigidity Increases After Expansion 75
Voigt Viscoelastic Modeling 78
Expansion Increases the Shear Modulus 78
Expansion Leads to Increase in Viscosity 81
Expansion Leads to Increase in Thickness 82
Conclusions 84
References 85

4. PROLONGED INCUBATION WITH LIPOSOMES LEADS TO PLA2 ACTIVATION IN ADENO-ASSOCIATED VIRUSES 90

Contribution of Authors and Co-Authors 90
Manuscript Information Page 91
Abstract 92
Introduction 92
Materials and Methods 95
AAV Purification 95
Liposome Preparation 96
Liquid Chromatography-Mass Spectrometry 96
Results and Discussion 97
Development of LC-MS Method 97
Measuring AAV Lipase Activity by LC-MS Method 99
Activation of AAV2 Lipase Domain 101
Product Specificity Is Independent of The Mode of Lipase Activation 102
AAV9 Exhibit Lipase Activity after Prolonged Incubation 104
Conclusions 104
References 106

TABLE OF CONTENTS-CONTINUED

5. COMPARISON OF THE VISCO-ELASTIC PROPERTIES OF VIRUSES, VIRUS BASED NANOMATERIALS AND ACTIVE PROTEIN CAGES 112

Contribution of Authors and Co-Authors 112
Manuscript Information Page 113
Abstract 114
Introduction 114
Materials and Methods 118
QCM-D Experiments 118
Rigidity Modeling 119
Results and Discussion 121
Small Protein Cages Exhibits Higher Rigidity 121
Cross Linking Leads to High Capsid Rigidity 122
C Terminal Domain in HBV Leads to Increase in Protein-Protein Interactions 123
AAV5 Exhibits Highest Rigidity Among Tested Adeno-Associated Viruses 124
NωV Shows A High Rigidity Despite A Bigger Size 125
PBCV Exhibits Least Rigidity in the Library 126
Δf/ΔD Ratio Corroborates With the Proposed Theoretical Model with Some Outliers 126
Rigidity and Triangulation Numbers Shows No Direct Relationship 129
Conclusions 131
References 133

6. CONCLUDING REMARKS 136

REFERENCES CITED 138

APPENDICES 162

APPENDIX A: Supporting Information for Chapter 2 163
APPENDIX B: Supporting Information for Chapter 4 168

LIST OF TABLES

Table Page

2.1. Transition temperature from DSF analysis of P22 morphologies at different pHs 37

2.2. Transition temperature from DSF analysis of P22 samples 44

2.3. AFM measurements of P22 particles 49

3.1. QCM-D data of different P22 morphology 77

5.1. QCM-D library of protein cages…… 121

LIST OF FIGURES

Figure Page

1.1. Steps to understand virus maturation 4

1.2. Schematic of HK97 bacteriophage maturation event in *Escherichia Coli* 6

1.3. Schematic of P22 bacteriophage maturation event in *Salmonella Typhimurium* 7

1.4. Thermal unfolding of a protein in the presence of SYPRO dye 9

1.5. Circular dichroic spectra showing the absorption of different secondary structure 10

1.6. Types of exchangeable hydrogen in proteins 12

1.7. Three mechanisms of Hydrogen Deuterium exchange 13

1.8. Operational mode in AFM 14

1.9. Qsense D 300 instrument, relation of change in frequency and dissipation 16

2.1. Capsid forms and maturation of P22 27

2.2. Heat triggered maturation of P22 PC, ES, EX and WB 38

2.3. DSF thermal scan on PC, ES, EX & WB 41

2.4. DSF monitoring of chemical stability of P22 morphology 43

2.5. AFM analysis of P22 morphology 47

2.6. Intact protein hydrogen deuterium exchange mass spectrometry of P22 particles 51

2.7. Solvent excluded surface area (SESA) calculations 53

2.8. Schematic energy landscape of the Assembly intermediates of P22 55

LIST OF FIGURES

Figure Page

3.1. I*n-vitro* maturation of P22 morphology 71

3.2. Typical QCMD spectra representing the change in frequency and dissipation along with time.....76

3.3. Representation fit of QCMD raw data and modelled Voigt data across different P22 morphology 79

3.4. Shear modulus obtained from Voigt model is represented and compared across all morphology of P22 80

3.5. Modeled viscosity value obtained from Voigt model is represented for all four morphology of P22 82

3.6. Layer thickness value obtained from Voigt model is represented and compared across all morphology of P22.....83

4.1. LC-MS analysis of POPC and the lysoPC product generated by bvPLA2.....98

4.2. Mass spectra of the substrate and product generated by bvPLA2.....99

4.3. Production of lysoPC by AAV2 over time 100

4.4. Lipase activity of AAV2 after prolonged incubation with liposomes 102

4.5. Comparison of enzyme specificity of heat activated and non-heated activated (prolonged incubation) AAV2 lipase.....103

5.1. Virus and protein cage library.....117

5.2. Rigidity, size and T-number of the various samples used in the study.....124

5.3. A scatter plot of simulated rigidity versus simulated diameter 127

5.4. A scatter plot of rigidity ($|\Delta f/\Delta D|$) vs the Diameter of the samples seen in Figure 5.2. 128

ABSTRACT

The dsDNA tailed bacteriophages comprise the largest evolving life form in the biosphere. They are not only the most abundant organism on Earth, but also plausibly the most ancient. The ancient origin of phage suggests that they have had the ample opportunity to undergo the evolutionary changes necessary to perform intricate coordinated biological functions. Therefore, characterizing a tailed bacteriophage will help not only to understand biology, but also help us to establish a relationship between structure and function. Viruses display a dynamic equilibrium between structural conformations, stability, flexibility and rigidity which is essential for the perpetuation of life cycle. Understanding this complex biophysical relationship is a daunting task and requires a combination of multidimensional approaches. P22 is a tailed bacteriophage and displays a series of structural transitions during maturation. To understand the important biophysical changes in the P22 at different stages of maturation, we have introduced a suite of orthogonal techniques to address the distinct properties of intermediates. These include Differential Scanning Fluorimetry which probes the thermal stability of P22 capsids, Hydrogen-Deuterium Mass Spectrometry, which probes the conformational flexibility and Atomic Force Microscopy and Quartz Crystal Microbalance with dissipation, which probe the biomechanical transformation in the capsids. P22 investigation using these techniques reveals the large scale structural arrangements along with the expansion. Global rearrangement results in an increase in stability, rigidity and reduced dynamics. The sum results of these studies indicate that expansion is accompanied by large scale inter-subunit rearrangements which lead to the enhanced hydrophobic core at different quasi-equivalent axes. We have also studied Adeno-associated viruses, which is used as a gene delivery vehicle for the treatment of genetic disorders. AAVs lipase contains a lipase domain and its activation is important for the successful infection. Activation mechanism of lipase domain is not thoroughly understood. To understand the mechanism, we have developed a Liquid Chromatography-Mass Spectrometry assay sensitive enough to measure lipase products. This assay confirms that prolonged incubation of AAVs with liposome is able to activate the lipase domain without the involvement of receptors and co-receptors.

CHAPTER 1

INTRODUCTION

Viruses have been proposed to exist for billions of years and they are probably as old as cells. Viruses display the potential of rapid multiplication in different host cells. In general, multiplication and propagation in viruses occurs as a cyclic process. Infectious viruses first incorporate their genomic content into host machinery where it multiplies and, is released from the host in favorable conditions. These particles are ready to infect, multiply, and propagate in the new host cells under favorable circumstances. These repeated events are termed as the virus life cycle. Viruses are often considered as pathogens spreading disease to human beings. But, along with the advent of advanced molecular biology, viruses have become an important tool to understand the structure and function relationship in larger biomolecular complexes. Understanding this relationship is extremely important to characterize the stability, dynamics, and function of nano-size mega Dalton complexes. Currently, viruses are used as gene therapy vectors, nano-containers, vaccine development, and other bioinspired materials. Characterization of viruses will facilitate the understanding of biology as well as the exploitation of nano-containers with different cargo in the diverse range of *in-vivo* and *in-vitro* applications.

Among viruses, approximately 10^{31} tailed bacteriophages are present in the biosphere (1, 2). Many structural and genomic studies have argued that tailed bacteriophages were already present even before the time when the three domains of life diverged approximately 3 billion years ago (1, 3–5). Investigating structure function

relationship of the tailed bacteriophages is necessary to understand the complex and highly coordinated mechanism behind their assembly. Tailed bacteriophages have been evolved along with time, many of them adapted different sequences, structure and function. Therefore understanding of different tailed phages will help us to understand "why different phages have chosen different pathways of maturation?" Another question which arises is "what are the fundamental differences between the evolution of different phages?" Understanding of the assembly behavior will help scientists to discover a common recurring hypothesis between different viruses.

Tailed bacteriophages have been under investigation for decades and we have understood that capsid assembly across diverse groups of viruses (bacteriophages and adenoviruses) share a common fundamental assembly process (3, 6, 7). There are approximately 10^{31} viruses to be present in the biosphere (1) are the tailed double stranded DNA bacteriophage (8). Viruses display different shapes including filaments, bullet-shaped, irregular and spherical. Nearly 50% of the viruses are spherical, usually icosahedral, and they display a unique maturation mechanism (9). Assembly of an icosahedral capsid is regulated by sequential and highly coordinated inter-coat protein interaction. Large protein complex assembly is governed through the weak interactions to avoid kinetic traps during assembly. Weak contact energies between coat subunits result in the formation of a stable icosahedral intermediate. This intermediate is capable of encapsulating genomic material and other host proteins. This rate limiting step provides precise annealing of subunits and proper positioning to propagate the maturation process (10, 11).

Maturation in Icosahedral Viruses

Investigating the assembly mechanism of a virus requires an understanding about the assembly behavior of the particular class including the formation of oligomers or direct assembly into meta structural intermediates (8, 9, 12, 13, 14). Icosahedral capsid assembly is generally associated with a maturation event primarily involving quaternary level structural rearrangements. Icosahedral virus assembly often initiates as a spherical form but, along with maturation, it undergoes a series of structural intermediates to attain a mature icosahedral capsid form. Icosahedral viruses have been under investigation for many decades and HK 97 phage and P22 phage are the most studied model systems. (15–17) (14, 18, 19) . *In-vitro* assembly systems mimicking *in-vivo* mechanisms have provided us the window of opportunity to understand important biological processes. Investigating the poised relationship between stability, structural integrity, rigidity and dynamics in icosahedral viruses is not only a key to understanding biology but also can be helpful in characterizing the cargo bound synthetic capsid for nanomaterials applications. Understanding the differences between characteristics of individual capsids and the characteristics that are a result from averaging the structures across a diverse population set the platform to understand natural and cargo modified capsids (20). Icosahedral viruses have been studied in good detail. In this group, HK97 is the most thoroughly studied, and it undergoes structural transitions involving expansion similar to P22. HK97 and P22 both share a common structure with high α-helix content and the HK97 fold. This structural core lays the foundation of the recurrent theme of the icosahedral assembly (21, 15, 16). HK97 maturation involves the formation of cross linking in the mature capsid while in the P22

capsid, it mainly involves the large scale structural rearrangements without any crosslinking (15, 16) (18, 22–24). Both display structural transition, HK97 with crosslinking and P22 without crosslinking, but the resultant mature capsid is an icosahedral expanded capsid. Therefore, comparing the biophysical properties of these two bacteriophages will help us set a recurring theme among dsDNA bacteriophage maturation. The understanding of a virus can be classified into different steps (Figure 1.1).

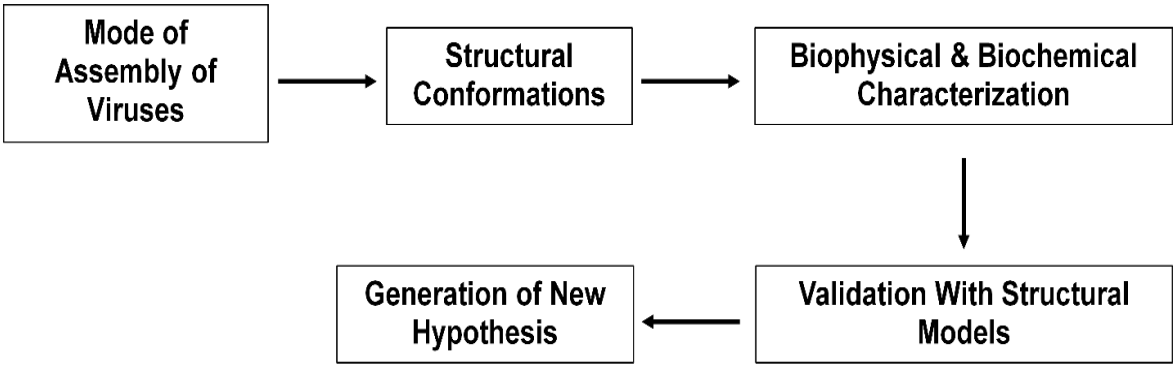


Figure 1.1. Steps to understand virus maturation

Maturation in HK97 Bacteriophage

HK 97 is an *Escherichia coli* phage isolated in 1977 in Hong Kong (25). *In vitro*, assembly of HK97 is initiated by expressing major capsid protein gp5. The capsid shell consists of 420 copies of subunits arranged into Prohead I. This structure is unstable when expressed with protease gp4. When co-expressed, gp4 cleaves the N terminus (102 residues) from each subunit resulting in a spherical morphology, Prohead II. At this stage, DNA begins to encapsulate inside causing the particle to expand and facet, resulting in

fully mature Head II. In the cross link mutant, final morphology is termed as Head-I (Figure 1.2). This transition results in major morphological changes from spherical to icosahedral shape. Change in shape results in intra- and inter-subunit arrangements (26, 27). In both mutant and wild type expansion several intermediates are proposed to exist along the maturation pathway. Among these intermediates, structural intermediate (EI) was trapped using acidic conditions (26, 28, 29). The transition to EI has a very short life span of approximately 3 minutes. E1 particles are cross linked hexamers with six fold symmetry. Approximately 60% of cross links are generated immediately after the formation of E1 intermediate. Formation of cross links follow a Brownian rachet process in which the loop containing K269 fluctuates until it forms the covalent bond with N356. Formation of sufficient cross links help the particle to overcome the energy barrier and the transition to EI-IV is observed. EII, III and EIV have the same morphology but with increased cross link interactions (Figure 1.2). By the EIV stage, 60 cross links were observed at pH 4.0. When pH is neutralized, pentamers also form the cross link to a final, mature particle with 65 nm diameter Mass spectrometry involving protease revealed the cross link between N356 and Lys169. It was proposed to form an isopeptide bond with release of NH_3. This cross linking is remarkable in a sense that it is autocatalytic in nature (30, 31).

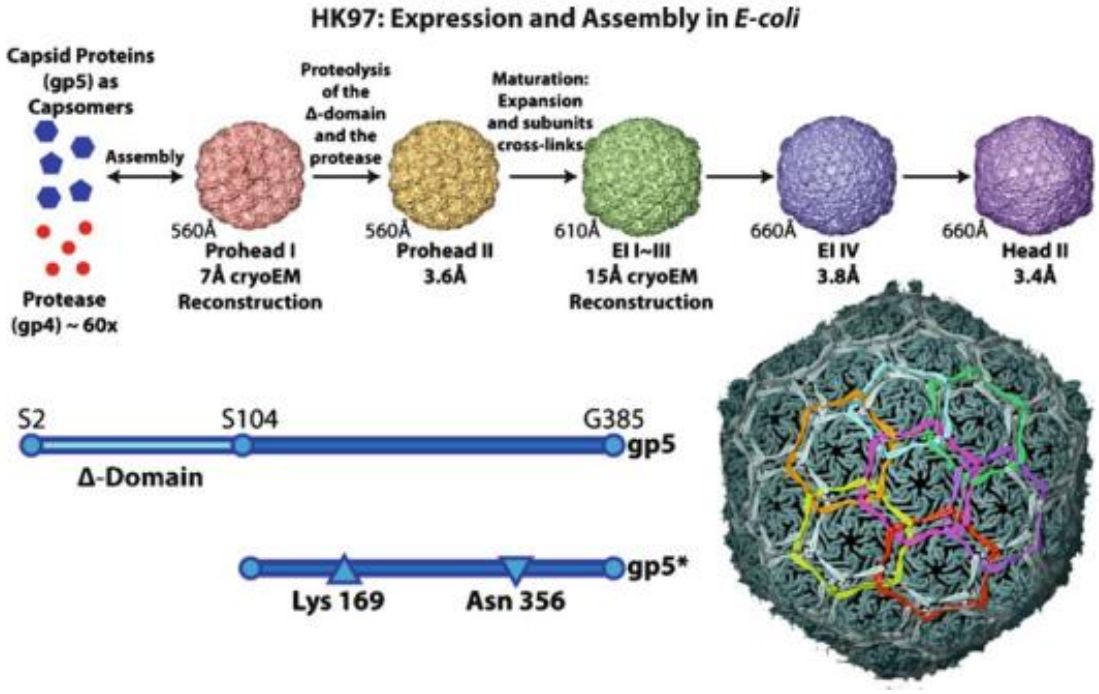


Figure 1.2. Schematic of HK97 bacteriophage maturation event in *Escherichia Coli* (21).

Maturation in P22 Bacteriophage

Bacteriophage P22 is a double stranded DNA phage of the Podoviridae family infecting *Salmonella typhimurium.* P22 is a T=7 model virus system used to understand macromolecular assembly in dsDNA icosahedral viruses. During capsid assembly and insertion of the genome into the capsid, P22 undergoes a series of structural transformations which result in maturation. Assembly of P22 is initiated by interaction and copolymerization of 420 molecules of coat proteins with 60-300 molecules of scaffold proteins along with 12 portal proteins and three ejection proteins to form a metastable procapsid (32–34). Scaffold protein plays an important role not only in initiation of

assembly but also for continuous polymerization. It maintains both assembly fidelity and activity (35). Packaging of phage DNA is mediated by action of ATP dependent terminase. Characteristic changes observed during packaging involve release of electrostatically bound internal scaffold proteins followed by readjustment in the lattice and expansion of the viral capsid. Lattice reorganization results in 10% increase in diameter along with the angular architecture of an icosahedral capsid (14, 36, 37). Once the DNA incorporation is complete, the portal is closed and the tail spike is associated to generate the infectious P22 particles (Figure 1.3). HK97 and P22 bacteriophage share the similarity of multiple structural transitions, but the principle behind biomechanical transformation is very different. Comparison of HK97 and P22 phage will help us to understand the underlying recurring theme in both phages.

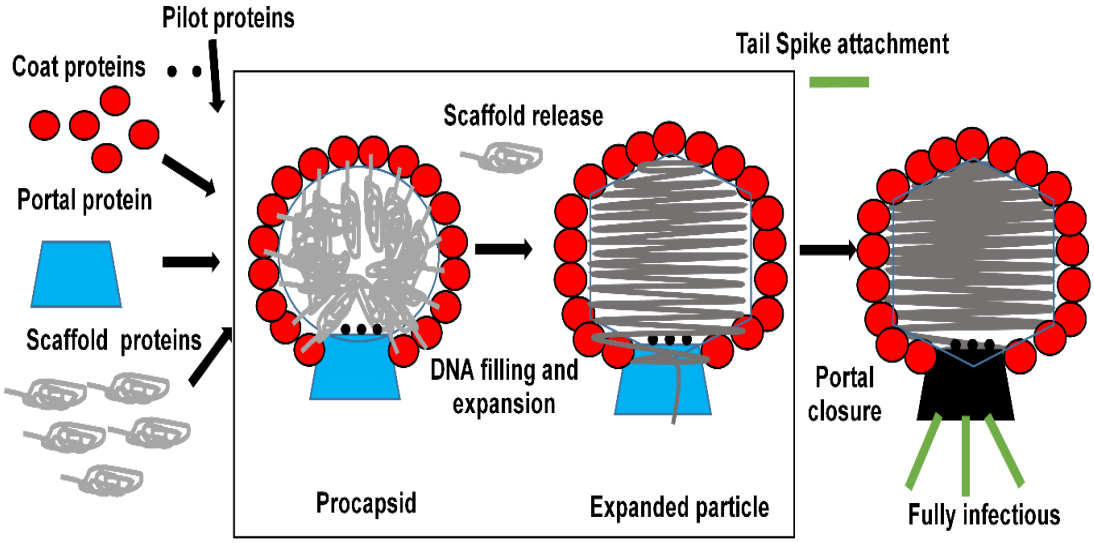


Figure 1.3. Schematic of P22 bacteriophage maturation event in *Salmonella typhimurium*.

Methods for Studying Viruses in Solution

We know primarily about viruses through capsid structure. Structural information was mainly derived through the capsid structure resolved by electron microscopy and X-ray crystallography. Understanding of assembly of icosahedral viruses resulted in the development of structural models which can be implemented to other categories of viruses. Along with the advancement of biophysical and biochemical tools, virologists began to ask questions about established models and started to pursue information beyond structural models. HK 97 virus has been studied for years, along with structural models various biophysical aspects have been studied. P22 has been under investigation for years, but the information regarding its maturation is not yet complete due to lack of biophysical and biochemical experimental data. In addition, P22's different morphologies are currently being used as supramolecular platforms for the vast variety of synthetic manipulations including bioinspired materials, MRI contrast agents to nano-medicine. Therefore, understanding the biophysical properties of P22 is important to implement as nano-container for nano-technological applications (41–45). We have introduced a suite of different techniques to understand the important biophysical changes in P22 along with maturation.

Differential Scanning Fluorimetry (DSF)

Differential scanning fluorimetry (DSF) also called Thermoflour is a rapid, sensitive, efficient and high throughput technique to detect step by step unfolding events of the protein or protein complexes. The basic principle behind this method is that the

unfolded protein with exposed hydrophobic residues can interact and bind with a hydrophobic sensitive fluorescent probe to generate high fluorescent intensity. When a protein starts to unfold due to high temperature, hydrophobic parts of the protein are exposed to the probe. The exposed hydrophobic parts of the protein bind to the fluorescent probe resulting in high fluorescent intensity as showed in Figure 1.4 (46–48). Generally, small molecule (ligand) binding can cause an increase in the free energy of unfolding which results in a positive shift in melting temperature (Tm). This positive shift in Tm is related to both the affinity and concentration of the respective ligand. Tm is calculated as the ratio of dF/dT from raw fluorescent data. Various probes are available to understand the different applications of DSF but SYPRO-orange dye is primarily used in many protein and ligand binding studies because of its perky fluorescence, high stability to chemicals, pH and other spectral features causing it to be effective and sensitive in the filter range of qPCR instrument (47). DSF is a well-established technique to characterize a megadalton viruses for example: Adeonoassociated viruses (49).

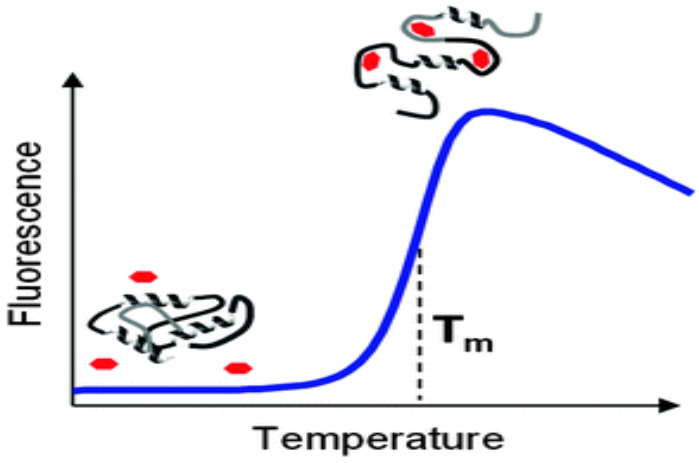


Figure 1.4. Thermal unfolding of a protein in the presence of SYPRO dye.

Circular Dichroism (CD)

Circular dichroism (CD) provides details more specific to secondary structure. This technique works on the principle of differential absorption of left and right circular polarized light by chiral molecules. CD can be used to study protein unfolding as a function of temperature or denaturants as well as local conformational events. (50–52). Alpha helices, beta sheets and random coil have a specific absorption of circular polarized light (Figure 1.5).

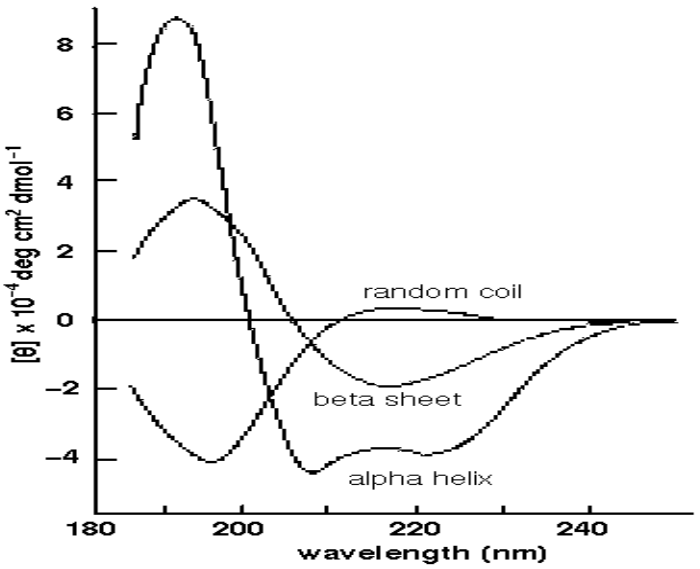


Figure 1.5. CD spectra showing the absorption of different secondary structure.

Hydrogen Deuterium Exchange
Mass Spectrometry (HDX-MS)

Proteins are dynamic molecules which undergo breathing and local or global folding/unfolding in real situations. HDX is a very important and effective tool to understand and quantitate these dynamic regions. The process of hydrogen deuterium

exchange in proteins is a chemical reaction in which labile hydrogen atoms are replaced with surrounding deuteriums. A number of studies have been done in recent years on protein folding events and protein-protein interactions (53). Based on the rate of exchange, replaceable hydrogens in proteins can be classified into three categories:

1. Amide hydrogens (NHs): Peptide back bone hydrogens can be replaced with deuterium in different time scales from a millisecond to days.
2. Fast replaceable hydrogens: Side chain hydrogens attached to Nitrogen, Oxygen, or Sulphur atoms can be exchanged with deuterium very fast in the scale of a microsecond.
3. Non-replaceable hydrogens: Hydrogen atoms bonded to carbon not exchange with deuterium in standard HDX conditions (Figure 1.6).

The mass shift (+1) due to deuterium exchange can be identified by liquid chromatography-mass spectrometry. There is always a possibility of back exchange of deuterium and it needs to be controlled very carefully. Hydrogen-deuterium exchange is governed by a number of critical factors such as temperature, pH, and quenching conditions.

High temperature can increase the back exchange by altering the ionization of H_2O molecules and also the rate of collisional diffusion. Rate of exchange is slowed down by an order of magnitude when the temperature drops down from room temperature to $0^{O}C$. pH is very critical in regulating the deuterium back-exchange. The minimum rate of exchange is reported to be in the range of pH 2.4-2.6. Other factors such as solvent

accessibility and hydrogen bonding can also determine the rate at which a peptide hydrogen is exchanged with a deuterium atom.

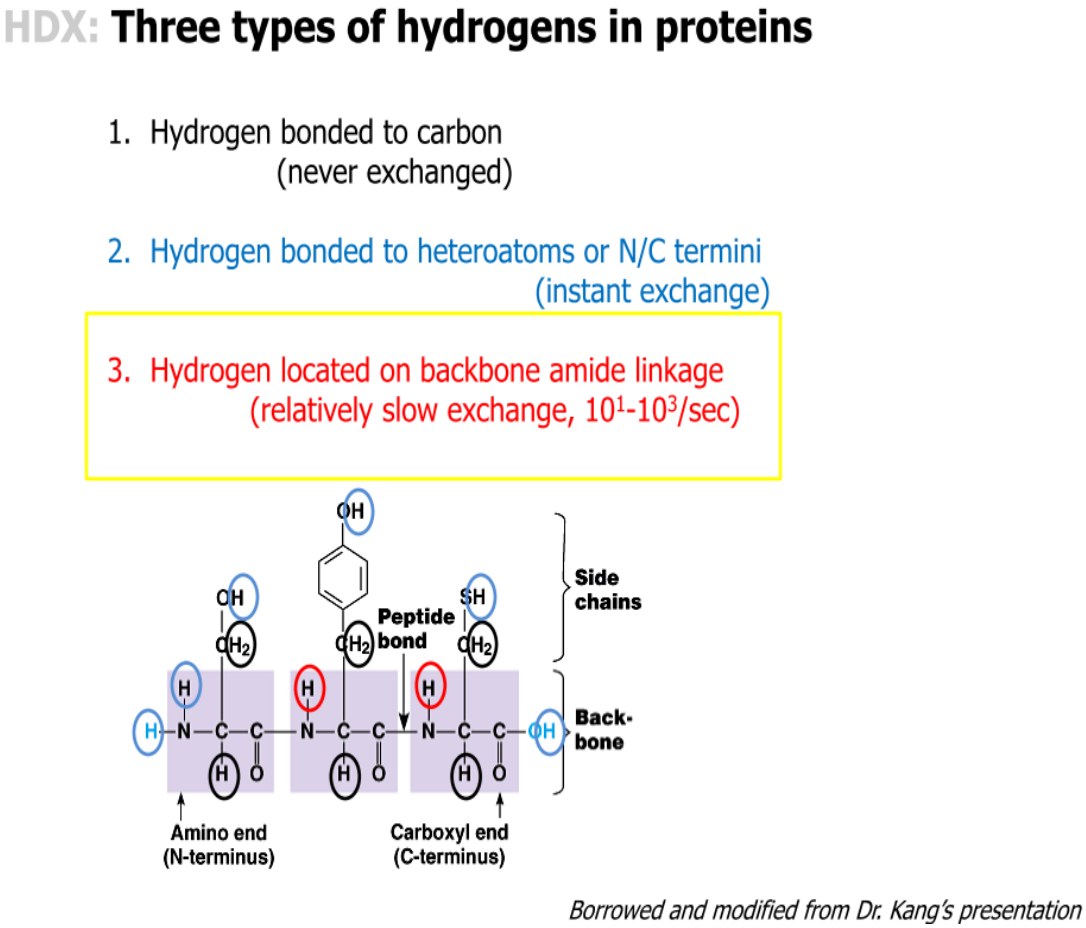


Figure 1.6. Types of exchangeable hydrogen in proteins.

In a folded protein, secondary structures like alpha helices and beta sheets where peptide NH atoms are involved in hydrogen bondings show more protection against deuterium exchange. Unstructured regions and loops are fairly accessible to deuterium and can exchange very fast. There are three possible mechanisms to explain HD exchange: fluctuations in folded state, local unfolding and global unfolding (Figure 1.7).

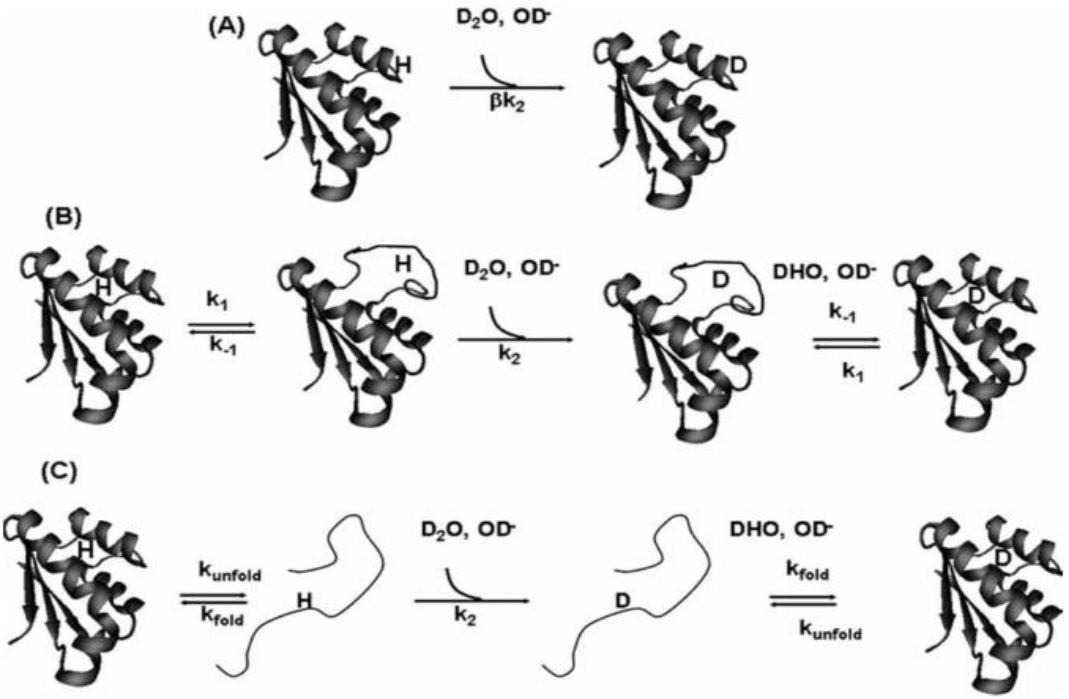


Figure 1.7. Three mechanisms of Hydrogen Deuterium exchange (54).

Atomic Force Microscopy (AFM)

AFM has been used for decades for the characterization of non-biological samples for example surface visualization of different silicon chips. In recent times, the AFM has been evolved to be applicable to biological materials. AFM instruments can be operated in either contact or tapping mode. In contact mode, the probe made up of either silicon or silicon nitride is in touch with the surface (for example P22 bacteriophage). The AFM probe is a sharp stylus with a very sharp radius of curvature. The probe is positioned at the end of cantilever (100-250 um length). The probe has a low spring constant to minimize the force between tip and material. Scanning is accomplished by moving the sample

underneath the probe tip with the help of a piezoelectric crystal positioned x-y stage. Interactions of the probe with material sub structure results in vertical displacement of tip as the probe tip moves across. This very small displacement is amplified by the deflection of a laser beam which is reflected from the top surface of cantilever. Deflections are detected and tracked by a split photodiode. A photoelectric circuit translates the deflection signal to height. All results are combined to generate a topographical image. Contact mode data can be collected in either height or deflection. In height mode, the surface and probe tip is positioned at a fixed distance. The observed deflection is very small. In deflection mode, the sample position is fixed and cantilever deflection data are recorded. Advanced cantilevers exert the force in the range from 10^{-9} to 10^{-12} N/m. The resolution of AFM is dependent upon the applied force by tip probe, but the greater force may damage the adsorbed material. By applying higher forces, relative comparison of rigidity can be obtained by determining the forces required by different materials to damage the surfaces.

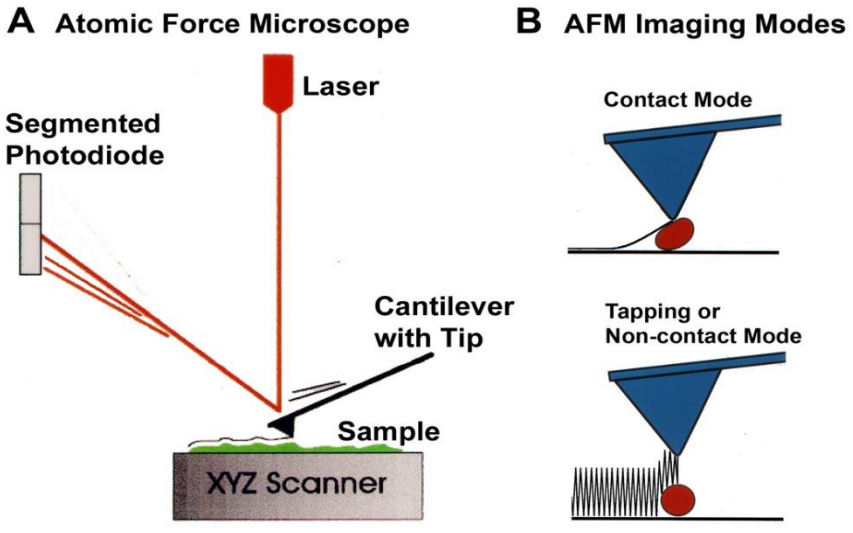


Figure 1.8. Operational mode in AFM. A) Basics of AFM and B) Operational modes in AFM.

Icosahedral viruses can be characterized in terms of rigidity by calculating the threshold force required before it collapses onto the bound surface. In tapping mode, the probe tip is not in continuous touch rather it oscillates up and down as it walks over the surface. In this mode, vertical position of sample is adjusted by a feedback system which maintains the amplitude of freely oscillating probe constant. This mode minimizes the lateral forces between sample and tip (55, 56). Tapping mode has emerged as a major tool for imaging and characterization of soft biological samples that would otherwise be too fragile to withstand contact mode operations (Figure 1.8).. AFM has already been used to determine the rigidity of wide class of viruses (57–61).

Quartz Crystal Microbalance with Dissipation (QCMD)

Piezoelectricity is a phenomenon in which a material generates electric potential when a mechanical stress/strain is applied to it. The Quartz Crystal Microbalance with Dissipation technology is based on the concept of piezoelectricity which measures the frequency and dissipation from an oscillating gold quartz coated crystal. It is a piezoelectric crystal which can oscillate at fundamental frequency as well as on different overtones (resonating frequencies) in response to applied mechanical stress. When any molecule is adsorbed on the quartz gold crystal the oscillation frequency decreases in response to the mass applied to it. The loaded mass of rigid material can be calculated by the Saurbey equation which correlates frequency change (Δf) and loaded mass (Δm) (62).

$$\Delta m = \frac{C}{n}\,\Delta f, \qquad C = \frac{t_q \rho_q}{f_n}$$

t_q = thickness of quartz, ρ_q = density of quartz and n= harmonic number

Q-Sense D300 can measure both change in frequency and dissipation at different overtones. The damping factor (or Dissipation) is the ratio of the Energy dissipated in each oscillation to the total energy stored. $D = \frac{E_{dissipated}}{2\pi E_{stored}}$ Dissipation is measured by periodically stopping the drive oscillation and measuring the decline in frequency to calculate the damping factor.

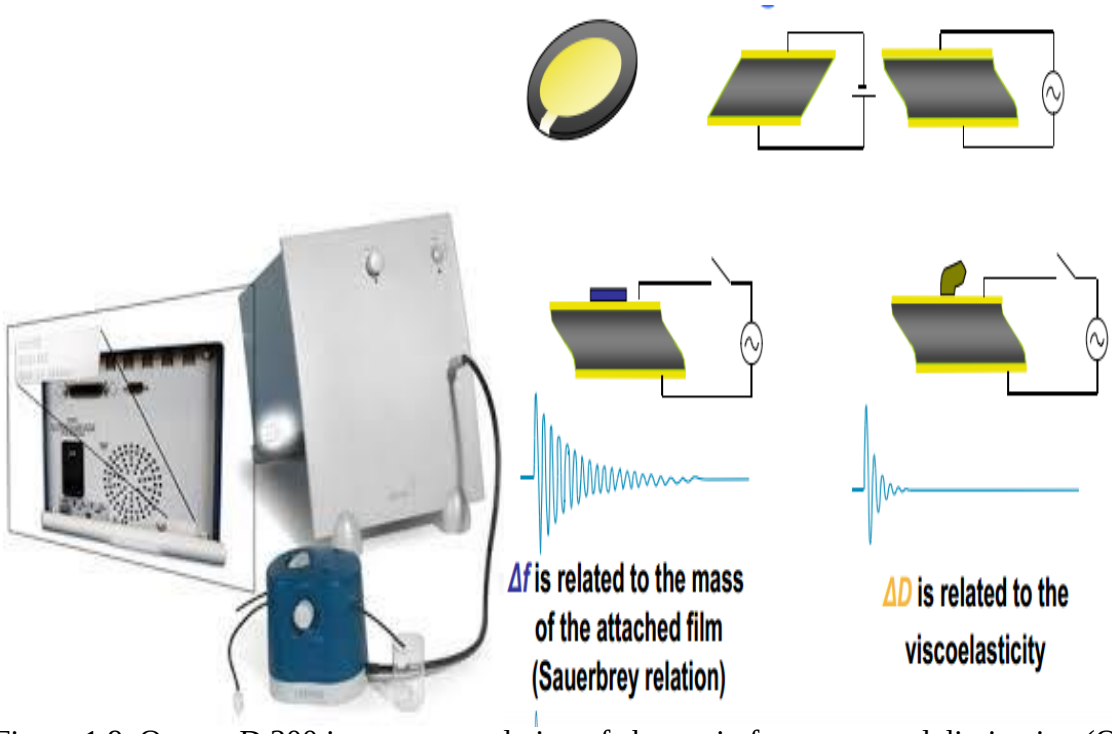


Figure 1.9. Qsense D 300 instrument, relation of change in frequency and dissipation (Q sense).

A soft material can undergo more deformation which results in partial uncoupling with the oscillation of the crystal. The more structural deformation, the more energy lost and the higher the dissipation value (Figure 1.9). By calculating the dissipation, we can measure and compare the relative rigidity of biomolecules (63). This technique can be used

as a complement to atomic force microscopy (AFM), though AFM uses nano-dentation to calculate the elastic modulus. This can be an alternative to AFM for the calculation of the elastic modulus used to calculate the rigidity of proteins. This technique is useful to investigate the relative structural changes in conformation in response to different solution conditions. The Q-Sense D300 instrument can measure both the fundamental frequency and dissipation of resonant energy at different overtones (15MHz, 25MHz and 35MHz). The damping factor calculation will provide an insight about the rigidity of the different proteins.

Summary

Investigations of virus particles in solution are mandatory to understand the *in-vivo* behavior. Biophysical and biochemical approaches are critical to comprehend the relationship between the structure and function. Comparison of biophysical data and informations from structural models set the recurring theme for the virus assembly. Understanding assembly of virus models will be critical to implement them as an effective nano-container for wide variety of applications.

References

1. Suttle C 2007. Marine viruses--major players in the global ecosystem. Nat Rev Microbiol 5:801–812.

2. Hendrix RW. 2002. Bacteriophages: Evolution of the Majority. Theor Popul Biol 61:471–480.

3. Baker ML, Jiang W, Rixon FJ, Chiu W. 2005. Common ancestry of herpesviruses and tailed DNA bacteriophages. J Virol 79:14967–70.

4. Holmes EC. 2011. What does virus evolution tell us about virus origins? J Virol 85:5247–5251.

5. Hendrix RW. 1999. Evolution: The long evolutionary reach of viruses. Curr Biol 9:914–917.

6. Duda RL, Hendrix RW, Huang WM, Conway JF. 2006. Erratum: Shared architecture of bacteriophage SPO1 and herpesvirus capsids (Current Biology (2006) 16 (R11-R13)). Curr Biol 16:440.

7. Johnson JE. 2010. Virus particle maturation: Insights into elegantly programmed nanomachines. Curr Opin Struct Biol 20:210–216.

8. Veesler D, Johnson JE. 2012. Virus maturation. Annu Rev Biophys 41:473–96.

9. Zlotnick A. 2005. Theoretical aspects of virus capsid assembly. J Mol Recognit 18:479–490.

10. Caspar DL. 1980. Movement and self-control in protein assemblies. Quasi-equivalence revisited. Biophys J 32:103–38.

11. Sarah K, Zlotnick A. 2009. The thermodynamics of virus capsid assembly. Met Enzymol. 455: 395–417.

12. Tuma R, Tsuruta H, French KH, Prevelige PE. 2008. Detection of intermediates and kinetic control during assembly of bacteriophage P22 procapsid. J Mol Biol 381:1395–406.

13. Bothner B, Taylor D, Jun B, Lee KK, Siuzdak G, Schultz CP, Schlutz CP, Johnson JE. 2005. Maturation of a tetravirus capsid alters the dynamic properties and creates a metastable complex. Virology 334:17–27.

14. Galisteo ML, King J. 1993. Conformational transformations in the protein lattice of phage P22 procapsids. Biophys J 65:227–35.

15. Wikoff WR, Liljas L, Duda RL, Tsuruta H, Hendrix RW, Johnson JE. 2000. Topologically linked protein rings in the bacteriophage HK97 capsid. Science 289:2129–2133.

16. Duda RL. 1998. Protein chainmail: Catenated protein in viral capsids. Cell 94:55–60.

17. Gertsman I, Gan L, Guttman M, Lee K, Speir JA, Duda RL, Hendrix RW, Komives EA, Johnson JE. 2009. An unexpected twist in viral capsid maturation. Nature 458:646–650.

18. Parent KN, Khayat R, Tu LH, Suhanovsky MM, Cortines JR, Teschke CM, Johnson JE, Baker TS. 2010. P22 coat protein structures reveal a novel mechanism for capsid maturation: stability without auxiliary proteins or chemical crosslinks. Structure 18:390–401.

19. Tuma R, Prevelige PE, Thomas GJ. 1998. Mechanism of capsid maturation in a double-stranded DNA virus. Proc Natl Acad Sci U S A 95:9885–9890.

20. Uchida M, Douglas T. 2013. Unravelling capsid transformations. Nat Chem 5:444–445.

21. Hendrix RW, Johnson JE. 2012. Viral Molecular Machines 726:351–363.

22. Chen D-H, Baker ML, Hryc CF, DiMaio F, Jakana J, Wu W, Dougherty M, Haase-Pettingell C, Schmid MF, Jiang W, Baker D, King J a, Chiu W. 2011. Structural basis for scaffolding-mediated assembly and maturation of a dsDNA virus. Proc Natl Acad Sci U S A 108:1355–1360.

23. Teschke CM, McGough A, Thuman-Commike P a. 2003. Penton release from P22 heat-expanded capsids suggests importance of stabilizing penton-hexon interactions during capsid maturation. Biophys J 84:2585–92.

24. Jiang W, Li Z, Zhang Z, Baker ML, Prevelige PE, Chiu W. 2003. Coat protein fold and maturation transition of bacteriophage P22 seen at subnanometer resolutions. Nat Struct Biol 10:131–5.

25. Dhillon EK, Dhillon ES, Lai AN, Linn S. 1980. Host range, immunity and antigenic properties of lamdoid coliphage HK97. J Gen Virol 50:217–220.

26. Gan L, Speir JA, Conway JF, Lander G, Cheng N, Firek BA, Hendrix RW, Duda RL, Liljas L, Johnson JE. 2006. Capsid Conformational Sampling in HK97 Maturation Visualized by X-Ray Crystallography and Cryo-EM. Structure 14:1655–1665.

27. Lee KK, Gan L, Tsuruta H, Moyer C, Conway JF, Duda RL, Hendrix RW, Steven

AC, Johnson JE. 2008. Virus Capsid Expansion Driven by the Capture of Mobile Surface Loops. Structure 16:1491–1502.

28. Gertsman I, Fu C-Y, Huang R, Komives EA, Johnson JE. 2010. Critical Salt Bridges Guide Capsid Assembly, Stability, and Maturation Behavior in Bacteriophage HK97. Mol Cell Proteomics 9:1752–1763.

29. Veesler D, Quispe J, Grigorieff N, Potter CS, Carragher B, Johnson JE, Structure 20:1384–1390.

30. Duda RL, Martincic K, Xie Z, Hendrix RW. 1995. Bacteriophage HK97 head assembly. FEMS Microbiol Rev 17:41–46.

31. Bonds SI, Kang HJ, Coulibaly F, Clow F, Proft T, Baker EN. Stabilizing Isopeptide Bonds Revealed in Gram-Positive Bacterial Pilus Structure, 2007, Science.318.

32. Earnshaw W, Casjens S, Harrison SC. 1976. Assembly of the head of bacteriophage P22: X-ray diffraction from heads, proheads and related structures. J Mol Biol 104:387–410.

33. Casjens S, Adams MB, Hall C, King J. 1985. Autogenous Modulation of Bacteriophage 123:174–179.

34. Tatnall M, King J. 1981. Purification of the Coat and Scaffolding Procapsids of Bacteriophage P22 Virology 529–547.

35. Prevelige PE, Thomas D, King J. 1988. Scaffolding protein regulates the polymerization of P22 coat subunits into icosahedral shells in vitro. J Mol Biol 202:743–57.

36. Casjens S, Wyckoff E, Hayden M, Sampson L, Eppler K, Randall S, Moreno ET, Serwer P. 1992. Bacteriophage P22 portal protein is part of the gauge that regulates packing density of intravirion DNA. J Mol Biol 224:1055–1074.

37. Parker MH, Casjens S, Prevelige PE. 1998. Functional domains of bacteriophage P22 scaffolding protein. J Mol Biol 281:69–79.

38. Galisteo ML, King J. 1993. Conformational transformations in the protein lattice of phage P22 procapsids. Biophys J 65:227–35.

39. King J, Botstein D, Casjens S, Earnshaw W, Harrison S, Lenk E. *Phil. Trans.R.Soc.Lond*. B. 1976. 276, 37-49

40. Parker MH, Prevelige PE. 1998. Electrostatic interactions drive scaffolding/coat protein binding and procapsid maturation in bacteriophage P22. Virology 250:337–49.

41. Usselman RJ, Qazi S, Aggarwal P, Eaton SS, Eaton GR, Russek S, Douglas T. 2015. Gadolinium-Loaded Viral Capsids as Magnetic Resonance Imaging Contrast Agents. Appl Magn Reson 46:349–355.

42. Patterson D, Edwards E, Douglas T. 2015. Hybrid Nanoreactors: Coupling Enzymes and Small-Molecule Catalysts within Virus-Like Particles. Isr J Chem 55:96–101.

43. Bedwell GJ, Zhou Z, Uchida M, Douglas T, Gupta A, Prevelige PE. 2015. Selective Biotemplated Synthesis of TiO2 inside a Protein Cage. Biomacromolecules 16:214–218.

44. Patterson DP, Schwarz B, Waters RS, Gedeon T, Douglas T. 2014. Encapsulation of an enzyme cascade within the bacteriophage P22 virus-like particle. ACS Chem Biol 9:359–365.

45. Patterson DP, Rynda-Apple A, Harmsen AL, Harmsen AG, Douglas T. 2013. Biomimetic antigenic nanoparticles elicit controlled protective immune response to influenza. ACS Nano 7:3036–3044.

46. Lo M, Aulabaugh A, Jin G, Cowling R, Bard J, Malamas M, Ellestad G. 2004. Evaluation of fluorescence-based thermal shift assays for hit identification in drug discovery Anal Biochem.332:153–159.

47. Vedadi M, Niesen FH, Allali-Hassani A, Fedorov OY, Finerty PJ, Wasney GA, Yeung R, Arrowsmith C, Ball LJ, Berglund H, Hui R, Marsden BD, Nordlund P, Sundstrom M, Weigelt J, Edwards AM. 2006. Chemical screening methods to identify ligands that promote protein stability, protein crystallization, and structure determination. Proc Natl Acad Sci U S A 103:15835–40.

48. Niesen FH, Berglund H, Vedadi M. 2007. The use of differential scanning fluorimetry to detect ligand interactions that promote protein stability. Nat Protoc 2:2212–21.

49. Rayaprolu V, Kruse S, Kant R, Venkatakrishnan B, Movahed N, Brooke D, Lins B, Bennett A, Potter T, McKenna R, Agbandje-McKenna M, Bothner B. 2013. Comparative Analysis of Adeno Associated Virus Capsid Stability and Dynamics. J Virol. 01415-13

50. Greenfield NJ. 2006. Using circular dichroism spectra to estimate protein secondary structure. Nat Protoc 1:2876–90.

51. Ranjbar B, Gill P. 2009. Circular dichroism techniques: biomolecular and nanostructural analyses- a review. Chem Biol Drug Des 74:101–20.

52. Kelly SM, Jess TJ, Price NC. 2005. How to study proteins by circular dichroism. Biochim Biophys Acta 1751:119–39.

53. Englander SW, Mayne L, Bai Y, Sosnick TR. 1997. Hydrogen exchange : The modem legacy of Linderstrom-Lang Prot Sci. 6:1101–1109.

54. Tsutsui Y, Wintrode PL. 2007. Hydrogen/deuterium exchange-mass spectrometry: a powerful tool for probing protein structure, dynamics and interactions. Curr Med Chem 14:2344–58.

55. Hansma PK, Cleveland JP, Radmacher M, Walters DA, Hillner PE, Bezanilla M, Fritz M, Vie D, Hansma HG, Prater CB, Massie J, Fukunaga L, Gurley J, Elings V. 1994. Tapping mode atomic force microscopy in liquids. Appl Phys Lett 64:1738–1740.

56. Kuznetsov YG, McPherson A. 2011. Atomic Force Microscopy in Imaging of Viruses and Virus-Infected Cells. Microbiol Mol Biol Rev 75:268–285.

57. Kuznetsov YG, McPherson A. 2011. Atomic force microscopy in imaging of viruses and virus-infected cells. Microbiol Mol Biol Rev 75:268–285.

58. Kuznetsov YG, Gurnon JR, Van Etten JL, McPherson A. 2005. Atomic force microscopy investigation of a chlorella virus, PBCV-1. J Struct Biol 149:256–263.

59. Michel JP, Ivanovska IL, Gibbons MM, Klug WS, Knobler CM, Wuite GJL, Schmidt CF. 2006. Nanoindentation studies of full and empty viral capsids and the effects of capsid protein mutations on elasticity and strength. Proc Natl Acad Sci U S A 103:6184–6189.

60. Roos WH, Gertsman I, May ER, Brooks CL, Johnson JE, Wuite GJL. 2012. Mechanics of bacteriophage maturation. Proc Natl Acad Sci 109:2342–2347.

61. Roos WH, Ivanovska IL, Evilevitch a., Wuite GJL. 2007. Viral capsids: Mechanical characteristics, genome packaging and delivery mechanisms. Cell Mol Life Sci 64:1484–1497.

62. Dixon MC. 2008. Quartz crystal microbalance with dissipation monitoring: enabling real-time characterization of biological materials and their interactions. J Biomol Tech 19:151–8.

63. Rayaprolu V, Manning BM, Douglas T, Bothner B. 2010. Virus particles as active nanomaterials that can rapidly change their viscoelastic properties in response to dilute solutions. Soft Matter 6:5286.

CHAPTER 2

STABILITY, BIOMECHANICS AND STRUCTURAL CHANGES IN P22 BACTERIOPHAGE DURING MATURATION

Contribution of Authors and Co-Authors

Manuscript in Chapter 2

Author: Ravi Kant

Contributions: Optimized and established the method, collected and analyzed data, prepared the manuscript

Co-Author: Aida Llauro

Contributions: AFM data collection.

Co-Author: Vamseedhar Rayaprolu

Contributions: Structural bioinformatics study.

Co-Author: Shefah Qazi

Contributions: P22 sample preparation.

Co-Author: Pedro J. de Pablo

Contributions: Aided in critical discussion of AFM data.

Co-Author: Trevor Douglas

Contributions: Aided in critical discussion of data and editing of the manuscript

Co-Author: Brian Bothner

Contributions: Obtained funding, discussed the results and implications and edited the manuscript.

Manuscript Information Page

STABILITY, BIOMECHANICS AND STRUCTURAL CHANGES IN P22 BACTERIOPHAGE DURING MATURATION

Authors: Ravi Kant, Aida Llauro, Vamseedhar Rayaprolu, Shefah Qazi, Pedro J. de Pablo, Trevor Douglas, Brian Bothner

Status of Manuscript:
_X _ Prepared for submission to a peer-reviewed journal
____ Officially submitted to a peer-review journal
____ Accepted by a peer-reviewed journal
____ Published in a peer-reviewed journal

Publisher:

Issue in which Manuscript Appears: In Preparation

CHAPTER 2

STABILITY, BIOMECHANICS AND STRUCTURAL CHANGES IN P22 BACTERIOPHAGE DURING MATURATION

Abstract

The capsid of P22 bacteriophage undergoes a series of structural transitions during maturation that guide it from a spherical to an icosahedral morphology. These transitions include the release of scaffold proteins and subsequent capsid expansion. Though P22 maturation has been under investigation for decades, a unified model that incorporates thermodynamic and biophysical properties is not available. Therefore a thorough, understanding of stability, rigidity, and structural changes during maturation is essential. To understand these changes and to establish a structural model describing the maturation process, we harnessed the integrated power of differential scanning fluorimetry, atomic force microscopy, circular dichroism, and hydrogen-deuterium exchange mass spectrometry. We show that P22 maturation mechanism is driven by small scale structural rearrangements. Our results show that the release of the scaffold proteins does not induce a major biophysical or structural change. However, after maturation, the coat proteins enter a quasi-equivalent environment and this results in increased thermal and chemical stability, higher structural rigidity and brittleness, lesser solvent accessibility and an enhanced hydrophobic core. We show that the maturation event increases the thermodynamic stability and drives the two mature forms, the expanded shell and the wiffle ball, to a lower free energy state. We also show that two different mature forms, expanded shell and wiffle

ball are different structures. Wiffle ball is structurally more elastic and solvent accessible than EX.

Introduction

Many important biological processes are carried out by supramolecular-protein complexes. These complexes require assembly, the directions for which are programmed into the amino acid sequence and coordinated via allosteric interactions. Icosahedral virus capsids are excellent systems for studying the process of assembly. In viruses, assembly of a symmetric capsid is orchestrated through a balance of polar and nonpolar interactions of asymmetric subunits (1–3). Viral capsids often utilize conformational switching to coordinate assembly (4–7). The subunit organization associated with capsid maturation from spherical to quasi-equivalent icosahedral symmetry can be classified into global and local rearrangements. Large global reorganizations are for the most part irreversible and often involve the crossing of a significant energy barrier on the conformational landscape. This is initiated by a specific stimulus, for example, genome packaging, receptor binding, and pH. Local reorganizations are transient, resulting from the sampling of different conformations and have been referred to as capsid breathing (8–10). There are an increasing number of protein-based nano-compartments in the field of applied nanotechnology (11, 12). These compartments are assembled from multiple subunits and this self-assembly property can be exploited to incorporate different active molecules inside it. Viruses are pertinent examples of a precise, self-assembling and highly stable

nanoparticles. Knowledge and understanding of a virus and its assembly mechanism can be helpful to engineer a nanoparticle for a variety of bioinspired applications (12, 13).

Among icosahedral viruses, P22 capsid is a well-studied model of assembly and maturation. P22 capsid has T=7 icosahedral symmetry. During assembly of the capsid and packaging of the genome, P22 undergoes a series of structural transformations through which a spherical procapsid adopts icosahedral symmetry (Figure 2.1).

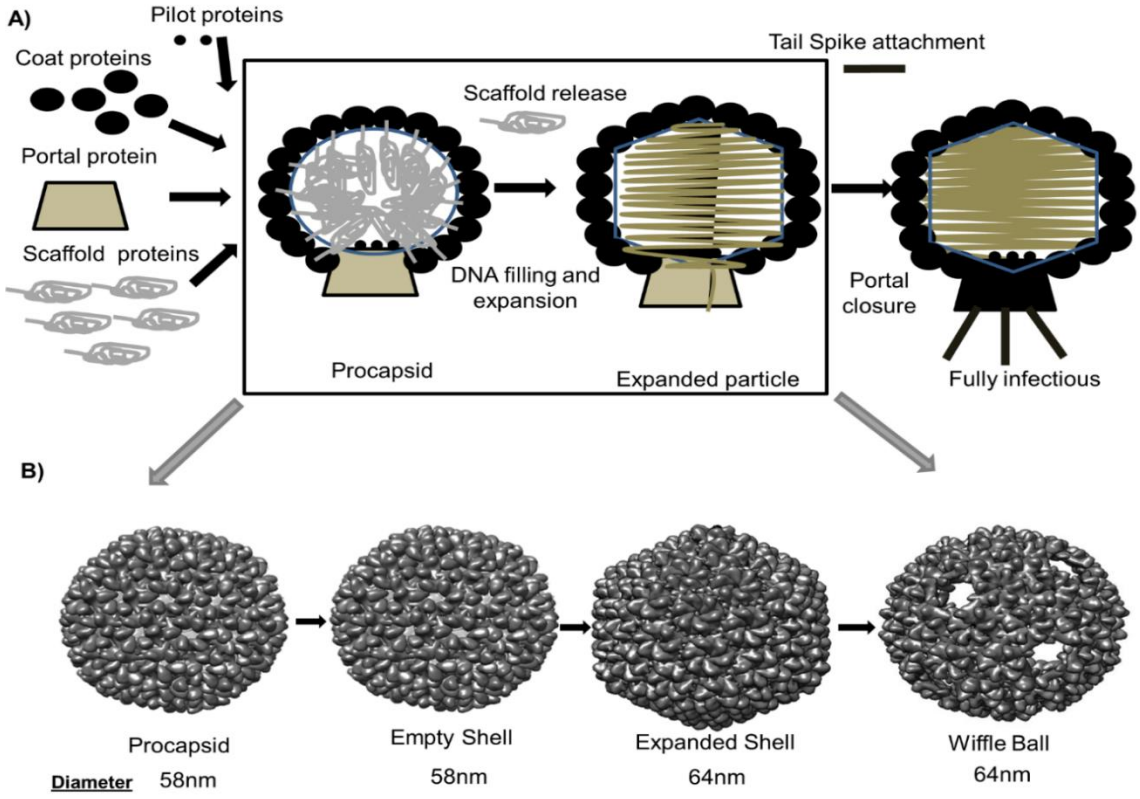


Figure 2.1. Capsid forms and maturation of P22. (A) *In vivo* maturation event of Bacteriophage P22 which leads to infectious form. (B) It shows the different assembled intermediates of P22 VLPs. Procapsid is composed of both coat and scaffold proteins, while Empty shell is devoid of scaffold proteins and only composed of coat proteins. Expanded shell is enlarged icosahedral shell made up of coat protein. Wiffle ball is same as expanded shell except missing pentons from fivefold vertices. (PDB ID 3iyi-Procapsid, 2xyz-Expanded shell, Wiffle ball- 3iyh).

This process of maturation results in a 10% increase in diameter. To assemble P22, approximately 420 molecules of coat proteins interact and co-polymer with 60-300 molecules of scaffold protein along with 12 portal proteins and 3 ejection proteins to form a metastable procapsid (14–16). Scaffold protein plays an important role not only in an initiation of assembly, but also in polymerization, helping to maintain both fidelity and active assembly (17). The packaging of DNA is an ATP-dependent process involving a terminase. During packaging release of electrostatically bound internal scaffold proteins is followed by a readjustment of the protein lattice and expansion of capsid. Expansion results in the formation of non-identical quasi-equivalent contacts between subunits. Quasi-equivalence results in conformational switching which involves the formation of hexamers and pentamers from same coat proteins (18). Thus maturation in P22 results in small differences in subunit interactions and conformations.

Maturation of P22 capsid can be mimicked in vitro by applying stress. Heat or denaturants will trigger expansion (19–21). In vitro studies have shown that heating of P22 procapsid at pH 7.6 mimics shell transformations that are the part of maturation (21). Heterologous expression of the coat and scaffold protein results in self-assembly of the spherical procapsid (PC) with a diameter of 58nm. Incubation of PC in 0.5M guanidine hydrochloride (GdmHCl) releases scaffold protein, producing an empty shell (ES) (16). Heating of ES at 65^{O}C for 20 minutes induces an irreversible expansion resulting in an expanded shell (EX) with a diameter 64nm (22). Heating of ES at 75^{O}C for 20 minutes causes the release of pentons from fivefold axes producing the wiffle ball (WB) form (23, 24). Due to an established in-vitro assembly system, P22 has been established as a nano-

platform for the directed assembly. Above morphologies of P22 are now being used as supramolecular platforms for the vast variety of synthetic manipulations covering the range from bioinspired materials, MRI contrast agents to nano-medicine.

The first three morphologies mimic structural intermediates occurring during expansion (24). While the morphological forms may be similar to that *in-vivo*, thermal activation is not an in-vivo mechanism. Changes in pH have been as an alternative to induce structural transitions in a variety of viruses, including Cowpea chlorotic mottle viruses (CCMV) and Nudaurelia ω capensis (4, 25). Therefore, it is important to understand the effect on pHs on structural intermediates. Capsid maturation has been studied in different icosahedral viruses, the best example of which is HK97. P22 and HK97 has a common structure with high α-helix content and the HK97 fold. This subunit fold is the foundation of a recurring theme of the icosahedral assembly (26–28). The comparative study of structural intermediates of HK97 by atomic force microscopy (AFM) shows an increase in Young's modulus and mechanical strength after maturation (29). The P22 maturation mechanism is different from HK97 in that P22 does not form covalent cross-linking. The P22 maturation mechanism is different from HK97 in that P22 does not form covalent cross-linking. Therefore, comparing them would help us to understand, if small scale rearrangements in P22 after maturation are significant enough to contribute to the mechanical changes after maturation. As detailed above, numerous studies describe the global rearrangements associated with P22 maturation, however, biophysical measurements of mechanical changes are few.

Biophysical and mechanical properties of proteins and protein complexes can be investigated by differential scanning fluorescence (DSF), circular dichroism (CD), atomic force microscopy (AFM) and hydrogen deuterium exchange mass spectrometry (HDX-MS). DSF is an established technique for following the thermal transitions of protein complexes and viruses (30). AFM can be used to image and make measurements of deformation by mechanical force. It has been applied to viruses such as HK97, PBCV and CCMV (29, 31, 32). HDX-MS is sensitive to changes in protein conformation and solvent exposure, demonstrating great utility in the study of capsids (6, 33–36). By applying these four analytical techniques to the structural intermediates of P22 capsids, we report a two-step mechanism in P22 maturation. In the first step, assembly is regulated by the formation of a weaker structure (procapsid) with identical coat protein environment. Second step involving expansion, results in a mature and stable capsid with icosahedral symmetry and quasi-equivalence. Our results show that full transitioning to quasi-equivalence results in increase inter-coat protein interaction, stability to heat and denaturant, higher rigidity and enhanced global hydrophobic core at different quasi-axes. Therefore, study of P22 bacteriophage provides an alternative paradigm where maturation is driven by small scale rearrangements between coat subunits and the mature capsid represents a global minimum.

Materials and Methods

Protein Purification of WT P22

P22 WT procapsid made up of 420 subunits, was produced by a heterologous expression system in *E. coli.* BL21 (DE) *E.coli* was grown in 1L cultures inoculated with

1 mL starter culture (37ºC, 220rpm). After 2 hours (OD_{600} = 0.6), the cultures were induced with 1mM IPTG and grown for 4 more hours. Cells were harvested by centrifugation at 3700g for 20 min. The cells were resuspended in PBS pH 7.6 and were incubated with DNase, RNase, and lysozyme (all Sigma-Aldrich) for 30 minutes at room temperature. Cells were lysed further by sonication on ice (Branson Sonifier 250, Danbury, CT, power 4, duty cycle 50%, 3 × 5 min with 3 min intervals). Bacterial cell debris was removed via centrifugation at 12000g for 45 min. The supernatant was then loaded on a 35% sucrose cushion and centrifuged at 48,000 rpm for 50 min in an ultra-centrifuge (50.2Ti ultra centrifuge rotor). The resulting virus pellet was resuspended in PBS, pH 7.0 and dialyzed to remove sucrose. The P22 ES was prepared by repeated extraction of the scaffolding protein with 0.5M guanidine-HCl. Purified ES were heated at 65ºC for 20 min to obtain P22 expanded and at 75ºC for 20 min to obtain P22 wiffleball. Each individual capsid form was routinely characterized using SDS-PAGE, native agarose gels, transmission electron microscopy (TEM, Leo 912 AB), and dynamic light scattering (DLS, Brookhaven 90Plus, Brookhaven, NY). The protein concentration was determined by absorbance at 280nm using the extinction coefficient (44,920 M^{-1} cm^{-1}).

Differential Scanning Fluorescence (DSF)

A) In Different pH Conditions: Differential Scanning Fluorescence scans of P22 morphologies (PC, ES, EX and WB) were performed in citrate phosphate buffer pH 7 (prepared from stock, 100mM citric acid and 200mM disodium hydrogen phosphate). P22 samples were diluted in citrate phosphate buffer with 50mM NaCl concentration to obtain

the final virus concentration (0.15mg/ml). To each sample, 2.5 µL of 1% Sypro-Orange dye (Invitrogen 140 Inc. S6651) was added to obtain the final reaction volume to 25 µL. The assays were conducted in a qPCR instrument (Corbett Research, RG-3000) with temperature elevating from 25-99 °C, increasing 0.5 degrees every 30 seconds. Lysozyme was run as positive control at final concentration of 0.3mg/ml. DSF assays were also performed in different pH (2.6, 4, 5, 6, 8, and 9) citrate phosphate buffer with the same experimental set up. Melting temperature of samples was determined by calculating the first derivative (dF/dT) from raw fluorescence data. For partial convoluted peaks, tip of the peak is used to calculate the melting temperature.

B) In Guanidine-Hydrochloride: Thermal denaturation of P22 samples were also studied in the presence of fixed concentration of guanidine-hydrochloride concentration (0.5, 1, 2, 3 M) at neutral pH. The reaction conditions and experimental set up in this experiment were same as for different pH DSF assays.

Circular Dichroic Spectroscopy

Circular dichroic (CD) spectra were recorded on JASCO-815 spectrometer. CD measurements were performed on PC, ES, EX and WB samples placed in fused silica cuvette with pathlength 10mm (Starna Cells, Atascadero, CA). Tight fitting stopper was placed on sample filled silica cuvette to prevent sample evaporation. CD spectra were performed between 25°C and 95°C with the ramping rate of 1°C/min controlled by a JASCO programmable Peltier-cooled temperature controller. Final concentration of samples was maintained at 0.03mg/ml. For thermal dependent scan, the parameters were

set in measure range 190-300nm, scan speed of 100 nm/min, with a 1 nm bandwidth and 1 nm data pitch. The UV data was recorded at every 5°C and the dichroic activity was supervised unceasingly and each observed spectrum was an average of 3 scans.

AFM Experiments

Measurements were performed with an AFM microscope (Nanotec Electrónica S.L., Madrid, Spain) operating in Jumping mode plus. Rectangular silicon-nitride cantilevers (Olympus, RC800PSA) with a nominal spring constant of 0.05 N/m were used and calibrated using Sader's method. Maximum imaging force during the measurement was 100 pN. The experiments were carried out under physiological conditions. One 20 μl drop of diluted stock solution was incubated on a silanized glass surface and, after 30 minutes, washed with buffer until a volume of 60 μl was reached. The tip was also pre-wetted with a 30 μl drop of buffer.

All AFM images were processed using WSxM software. Capsids stiffness and breaking force was determined as described in (37). Viral particles were considered as thin-shells that presented a linear elastic response upon deformation with the tip. The elastic constant (stiffness) of the particle was obtained from the slope of the initial linear part of the indentation curve. The breaking force was defined as the maximum force reached in the indentation before the breakage of the shell. In particular, we defined the critical strain as the ratio between the maximum deformation that the particle can withstand before rupturing and the height of the particle (i.e.,$\varepsilon_{critical} = \frac{\delta_{critical}}{height}$, where is the critical indentation).

Hydrogen Deuterium Exchange
Mass Spectrometry (HDX-MS)

Conformational flexibility of P22 samples were studied by intact protein hydrogen deuterium exchange mass spectrometry. Exchange reaction was instigated by 10 fold dilution of P22 stock concentration by D_2O buffer (10mM NH_4HCO_3, 50mM NaCl, pH 7.4). Final concentration of all samples after dilution was 0.1mg/ml. Hydrogen deuterium experiments were performed on 1290 UPLC series coupled to micro-TOF spectrometer (Bruker Daltonics) operated in positive electrospray ionization mode. Auto sampler was set to draw samples from the vial at different time points (0.5, 2.5, 5.5. 12.5, 37.5, 60.5, 90.5, 720 minutes). For Quenching of reaction, HxSil C8 reversed phase Hamilton column (20 x 2.3mm), frit porosity 2µm is pre-equilibrated with acid quenching conditions [20% (v/v) acetonitrile, 80% H_2O and 0.1% formic acid (w/v), pH 2.4]. The gradient conditions were set as follows: 0.5min, 40%B; 0.5-0.7 min, 40-95%B; 1.3min, 95%B, 1.5 min 20% where solvent A: 0.1% formic acid in water and solvent B: 0.1% FA in acetonitrile. The flow rate was 0.5 ml/min, auto sampler and column compartment temperature was set at temperature 25°C and 37°C. Data processing and analysis was performed with the help of Bruker Data Analysis package version 4.0. The maximum entropy deconvolution algorithm was used to calculate the increase in the mass of the P22 sample at different time points in the spectral range of 800 m/ z to 1600 m/z, which covers the majority of subunit charge envelope. Mass of deuterated samples at different points is calculated and the mass of control sample is subtracted from them to determine the total exchanged deuteriums. The relative mass difference between deuterated and undeuterated samples were calculated and plotted against time.

Calculation of Solvent Excluded Surface Area

The cryo-EM structures of P22 were not solved at atomic resolution and could not provide the positions of the side chains. Side-chains were necessary to compute the solvent excluded surface areas of subunits. To address this issue, Cα chains from the cryo-EM structures (2xyy, 2xyz, 3iyi, 3iyh) were extracted and were submitted to the Phyre2 server (38) for a template based side chain structure modeling. In brief, the P22 aminoacid sequence was submitted to the Phyre2 server (38) along with Cα chain extracted from the cryo-EM structure. The Cα chain was used as the template to make sure the output model structurally aligns well with the cryo-EM. During this process, the side-chains were also predicted and included in the output model. The structures 3iyi and 3iyh were solved by Parent et al. whereas the structures 2xyy and 2xyz were solved by Chen et al. In the case of 3iyi and 3iyh, the Cα structures were missing a number of residues (~40 amino acids). This discrepancy was accounted for during sidechain modeling by submitting only the sequence seen in the structure. To account for quasi-symmetry and for conformational polymorphism, Cα chains from multiple subunits were submitted to the Phyre2 server. For each of the structures obtained from Phyre2, clashes were eliminated and refinement was done using ModRefiner (39). The refined models were then structurally aligned into their respective quasi and icosahedral positions in the P22 capsid using the cryo-EM structure as the guide. Solvent excluded surface area (SESA) was computed from these aligned models with a probe radius of ~1.4Å for each subunit using UCSF Chimera software (40). The structure alignment was done using the match maker tool in UCSF Chimera software and SESA calculations were also performed in the same software. A guide cage was created

to correctly position the modeled protein subunits on their respective icosahedral axes. As the procapsid has a more spherical structure, the sphere factor of the guide cage (29nm radius) created was set to maximum. Similarly, sphere factor for the expanded shell and the wiffle ball guide structures (34nm radius) was set to the minimum to show the icosahedral nature of the actual capsid (Figure 2.7 A, B). Each corresponding subunit in all the forms is colored the same. The numeric values for specific interactions are listed in the table in the supplemental material (Table S1).

Results and Discussion

Differential Scanning Fluorescence Reveals Heat Triggered Structural Transitions

P22 maturation involves a significant expansion of the capsid driven by subunit rearrangement. This prompted us to test if changes in particle stability were associated with the transitions. In order to understand the thermal stability of P22 bacteriophage pre and post expansion, DSF was used. DSF is a high throughput, straightforward, and sensitive technique for tracking, thermal unfolding transitions of proteins. It uses a fluorescent dye that is quenched in an aqueous environment. An increase in fluorescence intensity is observed upon interaction with hydrophobic regions of a protein (41). This technique is useful for studying thermal transitions and measuring the thermal stability of viruses and virus-like particles (42). DSF thermal scans of PC, ES, EX and WB were performed from 25 to 99^{O}C at pH 7.0. The scan of the PC, which contains both coat and scaffold proteins, exhibited three transitions labeled I, II, III at 43.5^{O}C 75^{O}C, and 88.5^{O}C, respectively (Figure 2.2). Heating of ES, which no longer contains scaffold protein, had two thermal

transitions that precisely matched II and III from PC. The EX form of capsid also displayed two transitions, again matching II and III. WB, which is missing the pentamers, showed a single transition at the same temperature as III (Figure 2.2, Table 2.1).

Table 2.1. Transition temperature from DSF analysis of P22 morphologies at different pHs.

P22 samples	Temp range (^{0}C)	Transitions	pH 2.5	pH 4	pH 5	pH 6	pH 7	pH 8	pH 9
PC	30-45	I	37.0±0.5*	38.0±0.5	42.0±16	43.5±16	43.5±16	43.5±16	43.5±16
	70-80	II	37.0±0.5*	72.0±0.16	75.0±0.16	75.0±0.16	75.0±0.16	75.0±0.16	75.0±0.16
	80-90	III	62.5±0.1	84.5±0.5	88.5±0.5	88.5±0.5	88.5±0.5	88.5±0.5	88.5±0.5
ES	70-80	II	39.0±0.5	75.0±0.16	75.0±0.16	75.0±0.16	75.0±0.16	75.0±0.16	75.0±0.16
	80-90	III	63.5±0.1	88.5±0.5	88.5±0.5	88.5±0.5	88.5±0.5	88.5±0.5	88.5±0.5
EX	70-80	II	39.5±0.5	75.0±0.16	75.0±0.16	75.0±0.16	75.0±0.16	75.0±0.16	75.0±0.16
	80-90	III	64.5±0.1	88.5±0.5	88.5±0.5	88.5±0.5	88.5±0.5	88.5±0.5	88.5±0.5
WB	80-90	III	64.5±0.1	88.5±0.5	88.5±0.5	88.5±0.5	88.5±0.5	88.5±0.5	88.5±0.5

*Tm of transition I and II is same for procapsid in pH 2.6 as these events are convoluted.

A comparison of DSF scans of PC and ES revealed the absence of transition I in the ES (Figure 2). The major difference between PC and ES is the absence of scaffold, strongly suggesting that transition I is associated with scaffold release. Galisteo and King demonstrated that there is no distinct thermal transition during unfolding of scaffold proteins possibly, due to a general lack of tertiary structure (21). Transition I was broad and occurred at relatively low temperature (30^OC to 50^OC) which is consistent with this interpretation. A comparison of thermal profiles from PC, ES, EX and WB revealed the absence of transition II in WB. WB is structurally similar to the EX, both have icosahedral

symmetry and a diameter of 64nm. The difference is the absence of pentamers in WB. Together, these data strongly advocates that transition II is the release of pentamers.

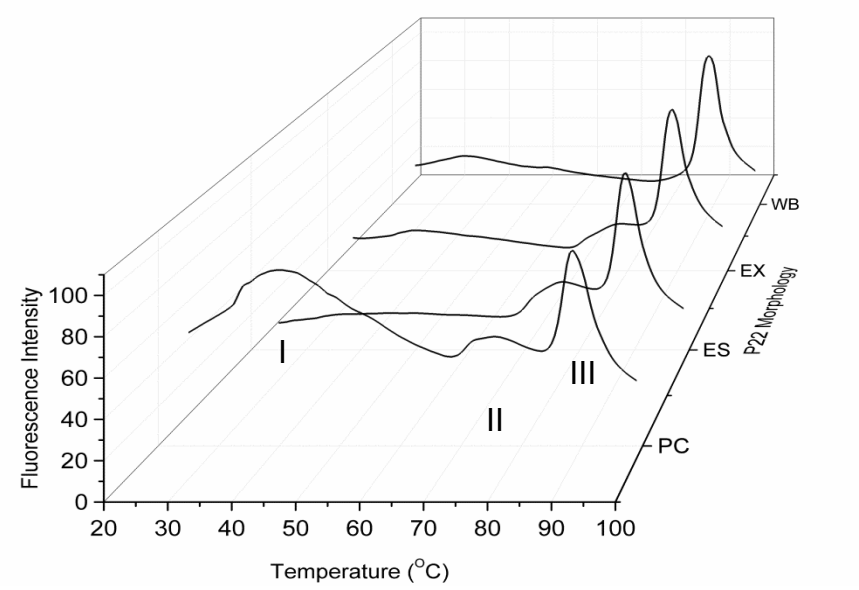


Figure 2.2. Heat triggered maturation of P22 PC, ES, EX and WB. DSF analysis of capsid was conducted by heating from 25 to 99 ^{O}C (pH 7.0) while monitoring fluorescence intensity of Sypro Orange. Thermal scan of PC (front) shows the presence of three transitions (I, II, III) which correspond to different stages of maturation (as shown in Figure 2.2). ES, which has lost scaffold proteins shows only two transitions (II, III). EX also shows the two transitions (II, III), while WB, which is devoid of pentamers at fivefold axis has one transition (III).

Previous experiments using differential scanning calorimetry (DSC) to analyze P22 maturation observed three endothermic transitions. The temperature of these transitions 48.5^{O}C, 71.4^{O}C and 87.3^{O}C correspond with what we have observed by DSF. A single exothermic transition was also observed by DSC at 61^{O}C. Electron microscopy, size exclusion chromatography and agarose gel electrophoresis also confirmed the release of scaffold at 48.5^{O}C and expansion of procapsid at 61^{O}C. Complete denaturation of particles

was reported at 85^{O}C (21). This data is consistent with our DSF experiments. The transitions are independent, as each form of capsid occupies a local energy minimum. Transition I am associated with the release of scaffold protein, transition II is associated with the release of pentamers at the fivefold axis, and transition III is the final denaturation of expanded capsids.

Structural studies indicate that large movements of pentons along the fivefold axes are similar both *in-vivo* and *in-vitro* expansion (43). Difference maps of *in-vivo* and *in-vitro* expanded particles show noteworthy similarity, further validating the use of thermally induced transition to study the maturation of P22 (24). The release of pentamers is not an *in-vivo* event, rather it is only observed during heat induced maturation. This loss of pentons suggests a destabilization of penton and hexon units at higher temperature and a possible mechanism for relieving stress in an icosahedral particle. Continuum elasticity theory, predicts that there is high lateral compression in pentamer units and this stress increases significantly with Triangulation number (44). A previous investigation has demonstrated that the penton moves radially outward by ~37Å upon heating. This movement is followed by the release of pentamers at the icosahedral fivefold axis (43). *In-vivo* the interaction between capsid protein, the DNA genome, and pilot proteins has been proposed to stabilize the pentons, averting release of pentamers during *in-vivo* expansion and DNA packaging (24).

pH Affects Thermal Structural Transitions

While temperature is a convenient tool for nudging capsids over energy barriers associated with maturation, it is of course not a part of the biological process. A more

relevant parameter is pH, which can initiate maturation by altering electrostatic interactions between subunit interfaces. The small icosahedral RNA tetravirus, *Nudaurelia ω capensis* (NωV), can be induced to mature from procapsid to capsid by decreasing the pH from 7.0 to 5.0. The mature capsid form is morphologically distinguishable, and smaller in diameter (4, 45). Another example is cowpea chlorotic mottle virus (CCMV), which at pH 5.0 is found as a closed 28nm particle. At pH 7.0 and low ionic strength, CCMV transitions to a swollen fenestrated form with the diameter increasing by 10% (25). Inspired by these studies, we were interested in the impact of pH on heat induced structural transitions in P22. To test this, DSF of each form was repeated at pH 2.6, 4.0, 5.0, 6.0, 8.0 and 9.0. DSF results at pH 5.0 - 9.0 showed the same transitions and similar temperatures as those observed at pH 7.0. (Figure 2.3). At pH 4.0 PC transition I lower by 5^{O}C, transition II by 3^{O}C and transition III by 4^{O}C (Table 1). No significant changes in Tm were observed for transitions associated with ES, EX and WB at pH 4.0. This suggests that protonation leads to partial disruption of the interaction between coat and scaffold proteins, resulting in early release of scaffold from PC and subsequent transitions (Figure 2.3). P22 particles remain intact at even lower pH, however, DSF scans at pH 2.6 revealed that they were destabilized. The DSF scan of PC at pH 2.6 had only two transitions, the first (I/II) centered at 37^{O}C and second transition (III) centered at 62.5ºC. ES and EX had two transitions (II and III) at slightly higher temperatures than in PC (table 1). As expected, WB showed only the final transition (III) at 65.5^{O}C, associated with particle disruption. These results show that with the exception of the PC, all forms of P22 capsid remained stable between pH 4-9. Below pH 4, P22 particles showed substantial thermal destabilization. But the relative intensity of

transition III increases in the order of PC<ES<EX/WB suggests high thermal stability after expansion (Table1). From this, we can conclude that pH has little effect on P22 from a biological perspective, however, for use as a nanomaterial, exposure to pH below 4 should be considered with caution.

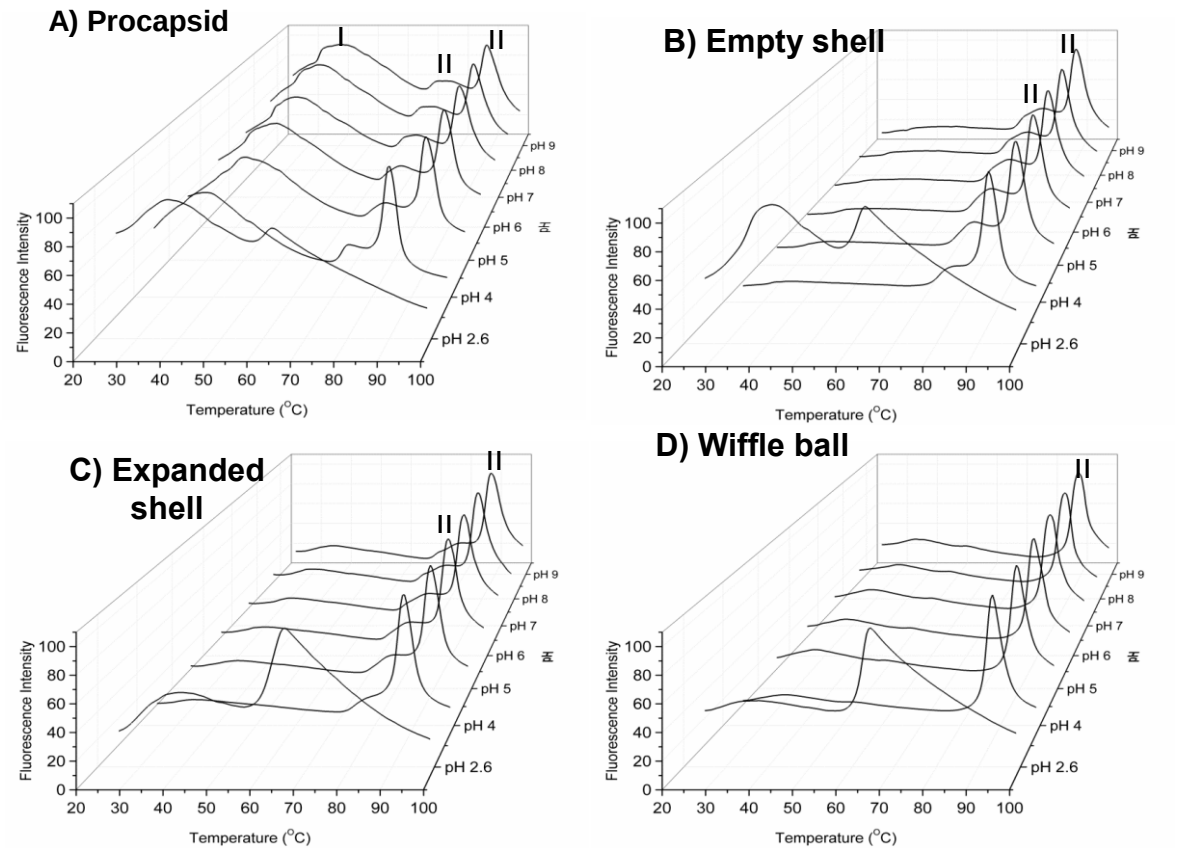


Figure 2.3. DSF thermal scan on PC, ES, EX & WB. (A) Measurement of fluorescence intensity of PC during heating in pH range 4.0 to 9.0 shows the presence of three transitions (I, II, III). (B) DSF scan of ES lacking scaffolds in the pH buffer 4.0 to 9.0 shows the presence of two transitions (II, III). DSF scan of in pH 2.6 showed only two transitions which occurred at relatively lower temperature. (C) DSF scan of EX shows two transitions (II, III) (D) Wiffle ball, which is lacking pentamers at fivefold axis shows only one transition (III). Graphs shown are the normalized average of three independent runs. (x axis represents time, y axis represents fluorescence intensity, z axis represents different pH range).

Maturation Increases Resistance to Denaturant

To gain a deeper understanding of the nature of capsid protein interactions during maturation, the impact of denaturant GdmHCl was investigated. At low concentration, 0.5M, GdmHCl denaturant is used to release scaffold protein without changing the integrity of capsid (16). At higher concentrations, GdmHCl changes the free energy of folding, making the folded form less favorable. Studies of model proteins indicate that the ionic nature of GdmHCl masks electrostatic interactions leading to unfolding (46–48). A recent study involving solvent effects on protein unfolding has also reported the destabilizing effect of GdmHCl on protein by facilitating the aqueous solvation of non-polar side chains and back bone surface area (49). Irrespective of the mechanism, GdmHCl is a much used tool for investigating to protein denaturation.

DSF thermal scans of PC, ES, EX and WB were performed at different concentrations of GdmHCl (0.5, 1, 2 and 3M) at pH 7.0. In 0.5M GdmHCl, PC Showed a decrease in intensity of transition I and partial convolution of transitions II and III (Figure 2.4A and S1). Compared with untreated particles, temperature of transitions II and III were lowered by 2^{O}C and 6^{O}C respectively (Table 2.2). GdmHCl release of scaffold from procapsid could account for the near absence of transition I. (Figure 2.4A). This interpretation is consistent with a previous study where incubation in 0.5M GdmHCl was shown to remove scaffold subunits from purified procapsids. The DSF curve of ES revealed a partial convolution of transition II & III. This partial convolution of transitions II and III suggests they are less distinct energetically. In ES the fluorescence intensity ratio of transitions II: III was nearly 1:1, whereas in PC, transition II intensity was higher than

transition III (Figure 2.4A). The melting temperature of ES transitions II and III were centered at 73^{O}C and 82.5^{O}C as for PC (Table 2.2).

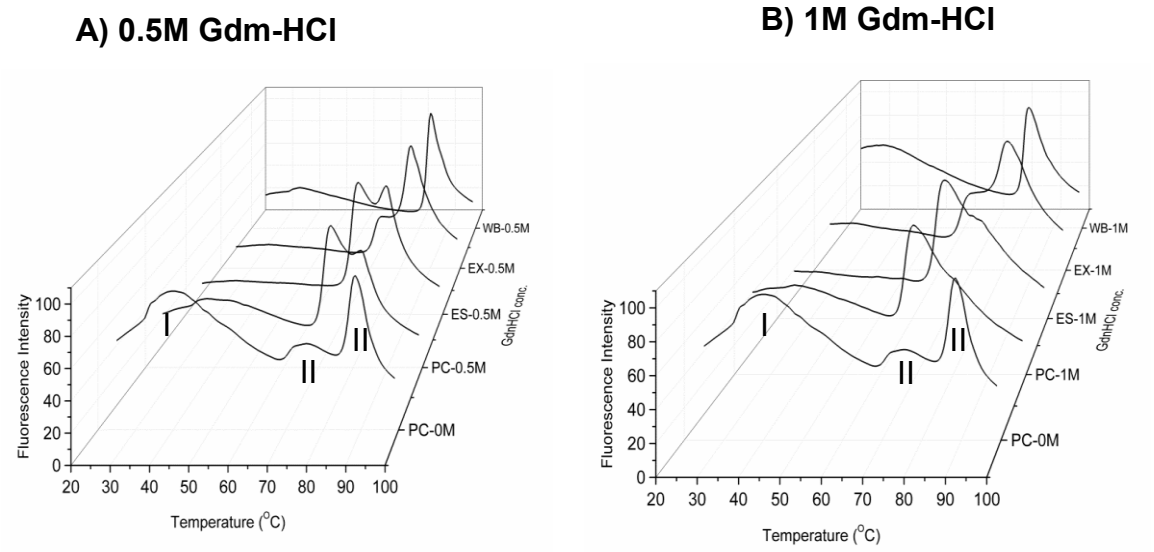


Figure 2.4. DSF monitoring of chemical stability of P22 morphology. DSF scans on PC, ES, EX & WB were performed in different guanidine hydrochloride concentration (A) 0.5M Gdn-HCl (B) 1M Gdm-HCl. Graphs shown are the normalized average of three independent experiments. (x axis represents time, y axis represents fluorescence intensity, z axis represents type of P22 morphology).

At higher concentration (1M GdmHCl) heating of PC resulted in the complete convolution of transitions II and III in a single transition. This suggests the concomitant release of pentamers and particle denaturation. ES behaves much the same, with the exception of a very small shoulder peak in the later half of the transition (Figure 2.4B), indicating that it maintains a structural transition to a greater extent than a PC. The melting temperature of the convoluted transitions for both PC and ES was centered at 68.5^{O}C (Table 2.2). In contrast to the PC and ES, EX retained transitions II and III distinctly. The melting temperature of the prominent transition III was 84^{O}C for both EX and WB. In 1M

GdmHCl thermal transitions differed by nearly 11°C between non-expanded (PC, ES) and expanded particles (EX, WB) for transition III. Heating in 2M GdmHCl resulted in significant loss of structural transitions for PC and ES, contrary to EX and WB which retained distinct transitions (Table 2.2). Furthermore, heating in 3M GdmHCl showed complete loss of all transitions for each morphology (2M, 3M data not shown).

Table 2.2. Transition temperature from DSF analysis of P22 samples.

P22 samples	Transitions	0.5M GdmHCl	1M GdmHCl	2M GdmHCl
PC	I	34.5±0.5	-	-
	II	73±0.5	-	-
	III	82.5±0.5	68.5±0.16	53.5±0.16
ES	II	73±0.5		-
	III	82.5±0.5	69.5±0.16	56±0.16
EX	II	73±0.5	70±0.16	56.5±0.16
	III	84±0.5	81.5±0.16	77.5±0.16
WB	III	84.5±0.16	82±0.16	78±0.16

The addition of GdmHCl had a more pronounced destabilization on spherical (PC and ES) compared to icosahedral capsids (EX and WB). In DSF, melting temperature is defined as the temperature at which maximal binding of the hydrophobic dye SYPRO

Orange is observed. Therefore, DSF reports on the destabilization of hydrophobic protein regions. Our observation is supported by Raman spectroscopy of P22, PC and EX (50). This study revealed that all six tryptophans in PC readily exchange hydrogens, whereas after conversion to EX exchange decreases. The large increase in Tm associated with expansion suggests that the changes in protein stability go beyond the tryptophan residues.

Circular Dichroism is Inconsistent with Refolding during Maturation

To gain further insight to the structural changes associated with P22 maturation, we turned to Circular Dichroism (CD), which provides details more specific to secondary structure. CD is a sensitive technique to monitor the changes in secondary structure, making it useful for the study of local or global protein unfolding as a function of temperature or denaturants (51). Spectra of all four P22 morphologies were recorded from 25 to 95^{O}C. Our CD data showed that P22 capsid secondary structure is rich in β strands. This data is consistent with previous CD data collected on purified coat proteins (52). Analysis of the thermal scans showed no significant change in the secondary structure from 25 to 85^{O}C at pH 7.0 (Figure S1). However, above 85^{O}C there was a sharp transition in the CD curves, followed by a complete loss of signal (Figure S1). The spectra do not transition through a random coil signal, but rather a loss of signal. This suggests that subunit dissociation was followed by rapid aggregation and precipitation. The temperature transitions observed by CD, DSF, and DSC are highly similar (21). Our CD experiments rule out the possibility of secondary structural changes as a driving force for the structural transitions.

AFM Analysis of the Mechanical Properties of P22

The maturation of P22 through expansion and adoption of icosahedral symmetry increased particle stability to heat and denaturant. To study the mechanical changes of the particles we complemented our bulk biochemical experiments with single particles measurements by AFM. AFM is a suitable technique that permits the imaging and manipulation of particles at single particle level. Characterization of virus structure in liquids allowed us to identify and characterize the structure and height of the different particles after adsorption (Figure 2.5A and 2.5B). PC and ES showed spherical structures and presented heights of 50±1 nm and 48±1 nm, respectively (black and red bars in Figure 2.5B). In comparison with the value obtained by cryo-EM (53), these values represented only a 86% and 83% of the virus diameter, indicating that the particles were deformed in contact with the substrate. In contrast to PC and ES, EX presented a more faceted appearance and their orientation could be distinguished (for instance, the EX capsids shown in Figure 2.5A were adsorbed along the 5-fold symmetry axes). We saw that the height of the particle depended on the particle. EX particles presenting a S5 orientation were higher than particles along the S3/S2 orientation (we classified together S3 and S2 orientation because it was difficult to distinguish between them). Most of the WB that we found were presenting a S3 orientation (see Figure 2.5A, bottom) and we observed that the height of these structures was lower when compared to their expanded forms (Figure 2.5B, green bars), suggesting that the substrate induced a major deformation on the WB than on the EX forms.

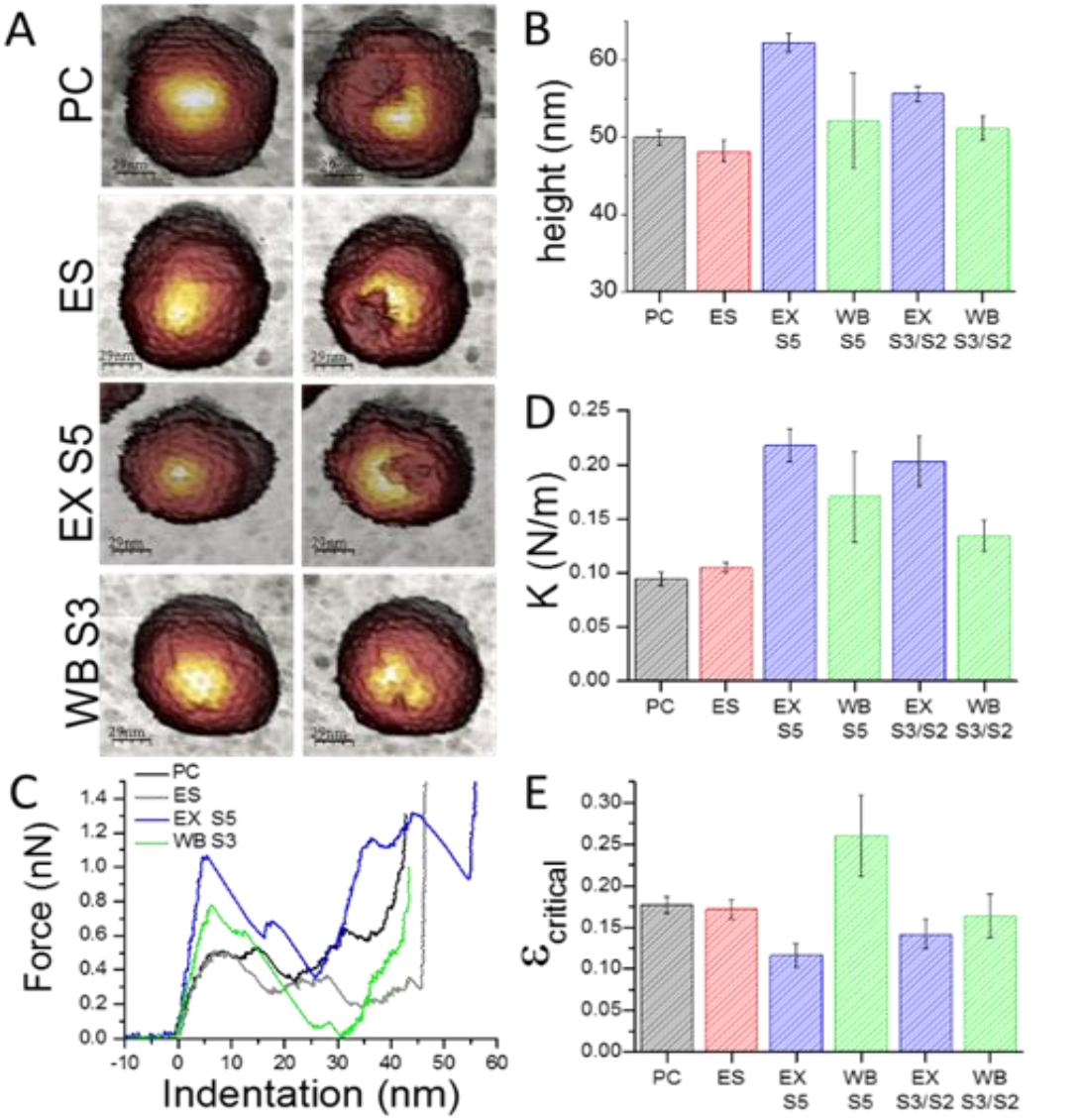


Figure 2.5. AFM analysis of P22 morphology**.** (A) AFM images of individual P22 particles before (left) and after the breakage (right). From top to bottom: procapsid, empty shell (lacking scaffolding protein), expanded capsids (along the 5-fold symmetry axes) and wiffle ball (along the 3-fold symmetry axes). Color bar, from substrate to the highest point: grey-red-yellow-white. (B) Force-indentation curves that rupture the particles shown in panel A. (C) Comparison of the height, elastic constant (k), and critical strain ($\varepsilon_{critical}$) of the different morphologies. For EX and WB the symmetry could be distinguished and particles were classified in two groups (S5 and S3/S2).

To study the rigidity and brittleness of the particle we performed nano-indentation assays. Briefly, nano-indentation experiments consist on deforming individual particles with an AFM tip until inducing the breakage of the specimen (54). The deformation of the particle (indentation) is registered as a function of the force applied to the particle which leads to the force-indentation curve (FICs)(55). Figure 2.5C shows four different indentation curves performed on the particles shown in panel 5A that were done in order to produce the breakage of the shell. After rupturing the shell, an image on the particle was acquired to ensure that the damage was produced (see Figure 2.5A, right). From the FIC, information about the rigidity (elastic constant, k) or brittleness of the particle (critical strain, $\varepsilon_{critical}$) can be obtained (Llauro et al, cargo-shell coupling, under revision). High values of $\varepsilon_{critical}$ indicate that the particle resist large deformations and is not brittle, whereas low values are characteristic of a brittle material. No significant changes in the mechanical properties were observed after scaffold protein removal (compare black and red bars in Figure 2.5D and 2.5E). However, after expansion the particles increase their rigidity and become more brittle (see blue bars in Figure 2.5D and 2.5E). The removal of pentons provoked to things, particles become softer, as it was previously predicted by continuum elasticity theory (56) but also increase the deformability capacity of the WB cages. Another study of P22 have also revealed that expansion from procapsid to virion results in thinning of shell wall (53). These observations make it plausible that rigidity has to increase after expansion, otherwise mechanical strength of the intact virus would have been weakened drastically. Similar observations have already reported in HK97 where increase in Young's

modulus is observed after expansion, although there is an involvement of cross linking between capsomers (29).

Table 2.3. AFM measurements of P22 particles.

	# of particles	K N/m	$\varepsilon_{critical}$	height nm
PC	32	0,094±0,006	0.18±0.010	50±1
ES	12	0,105±0,005	0.17±0.01	48±1
EX S5	8	0.218±0.015	0.12±0.01	62±1
WB S5	3	0.17±0.04	0.26±0.05	52±6
EX S3/S2	11	0.20±0.02	0.14±0.02	56±1
WB S3/S2	9	0.13±0.01	0.16±0.03	51±1

Hydrogen-Deuterium Exchange of P22 Capsids

Up to this point, our data has been consistent in that particle maturation increased capsid stability to thermal, chemical, and mechanical probing. A question remaining was how structural transitions impacted the conformational dynamics of protein subunits and their interactions. To investigate this, intact protein hydrogen deuterium exchange mass spectrometry (HDX-MS) was used. HDX-MS is a straightforward and versatile technique for probing conformational change and dynamics of protein complexes (6). P22 particles were rapidly diluted 10-fold in a buffered solution of D_2O. The incorporation of deuterium in place of exchangeable protons was measured over time using LCMS (57). The rate and extent of deuterium uptake is dependent on protein backbone solvent exposure and

structural changes. Under the denaturing conditions for LCMS, P22 capsid disassembled into coat proteins, allowing accurate mass measurement of the subunits. Measurements of the change in mass of coat protein at different lengths of incubation were completed. The P22 coat protein had a measured mass of 46,620 DA (expected 46,620). After dilution in D_20, a rapid uptake of deuterium was observed for all four morphologies for the first five minutes of exchange (Figure 2.6A). EX showed the least uptake in comparison with others. The 0 -5 minute time window represents fast exchanging regions. Fast exchange is generally attributed to solvent exposed and dynamic domains. These are often coils, loops, and regions undergoing conformational change. After one hour of exchange, PC and WB had a significantly greater level of exchange than ES and EX. During this time period, medium to slow exchanging amide nitrogens contribute to exchange, providing information on conformational change occurring on a relatively long time scale. The reaction was followed for 12 hours to ensure that slow exchanging regions were accounted for. Slow exchanging regions report on well-ordered secondary, tertiary, and quaternary structures offering a way to access protection from solvent. At 12 hours, samples had a progressive decrease in exchange from PC to EX as 18 additional residues were protected (Figure 2.6B). We hypothesize that the majority of the additional protection arises from increased interactions and protected residues could be participating in the formation of new quaternary contacts associated with the adoption of quasi-equivalent icosahedral symmetry. The WB showed an increase in exchange compared to the EX. This observation was initially unexpected due to the fact that WB showed a higher Tm and more resistance

toward GdmHCl denaturation. However, the absence of pentamers increased the average solvent accessible surface area, making direct comparisons with WB difficult to interpret.

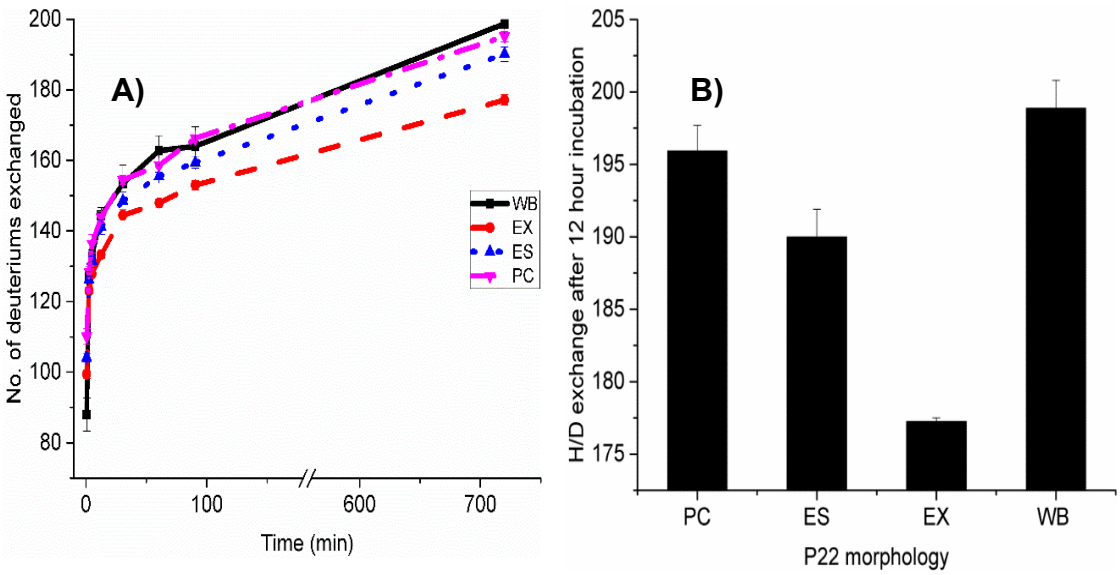


Figure 2.6. Intact protein hydrogen deuterium exchange mass spectrometry of P22 particles. Procapsid, empty shell, expanded shell & wiffle ball were diluted in 10mM ammonium bicarbonate, 50mM NaCl D_20 buffer, pH 7.0. (A) Number of deuterations incorporated (y axis) along with incubation time (x axis) for coat protein. (B) Total number of deuteriums exchanged after 12 hours. Total exchange reactions were carried out for 12 hours and done in three technical replicates. Error bars represent $\pm$ 1 SD.

Maturation Increases Solvent Excluded Area

To complete our biophysical model of P22 maturation, we needed to connect the solution-phase measurements with the known structure. Models of P22 from cryo-EM at 4.0 Å resolution showed that the change in the morphology from PC to EX involved a change from skewed to symmetric hexamers (53). Symmetric hexamers create a consistent interaction surface across hexameric and pentameric capsomers and allow additional

interactions in the E loop/P domain as well (53). These interactions are suggesting an increased global interactions in the mature capsid. However, a direct analysis of subunit interfaces and solvent excluded surfaces had not been completed. To do this, we analyzed changes in quaternary organization, paying specific attention to the total solvent excluded surface area (SESA). Two sets of cryo-EM based structural models from two different labs were perused for this analysis. Due to lack of atomic level resolution of cryo-EM model and the requirement for side chain density to estimate SESA, PDB files 2xyy, 2xyz, 3iyi and 3iyh were submitted to Phyre2 (38) and Modrefiner (39) severs for side chain modeling and secondary structure refinement.

The two data sets represented different morphological pairs corresponding to PC and EX and PC and WB. We compared the new models for EX and WB with their respective PC partner (2xyy with 2xyz and 3iyi with 3iyh). Comparison at the subunit level between the pairs of structures was avoided due to differences in the observed amino acids. In the case of 3iyi and 3iyh, the Cα structures were unassigned ~40 amino acids in the structure. This discrepancy accounted for during side chain modeling by submitting only the sequence seen in the structure. A change in the number of residues involved in structure would have an influence on secondary structure prediction as well as calculation of SESA at different interfaces, hence comparison was avoided. Figure 2.7 A and B shows the subunits interfaces across different cryo-EM models taken into account in the SESA calculations, while panel C shows the relative difference in SESA values at regular (I) and quasi-equivalent (Q) axes for both pair group. See Figure S2 for details.

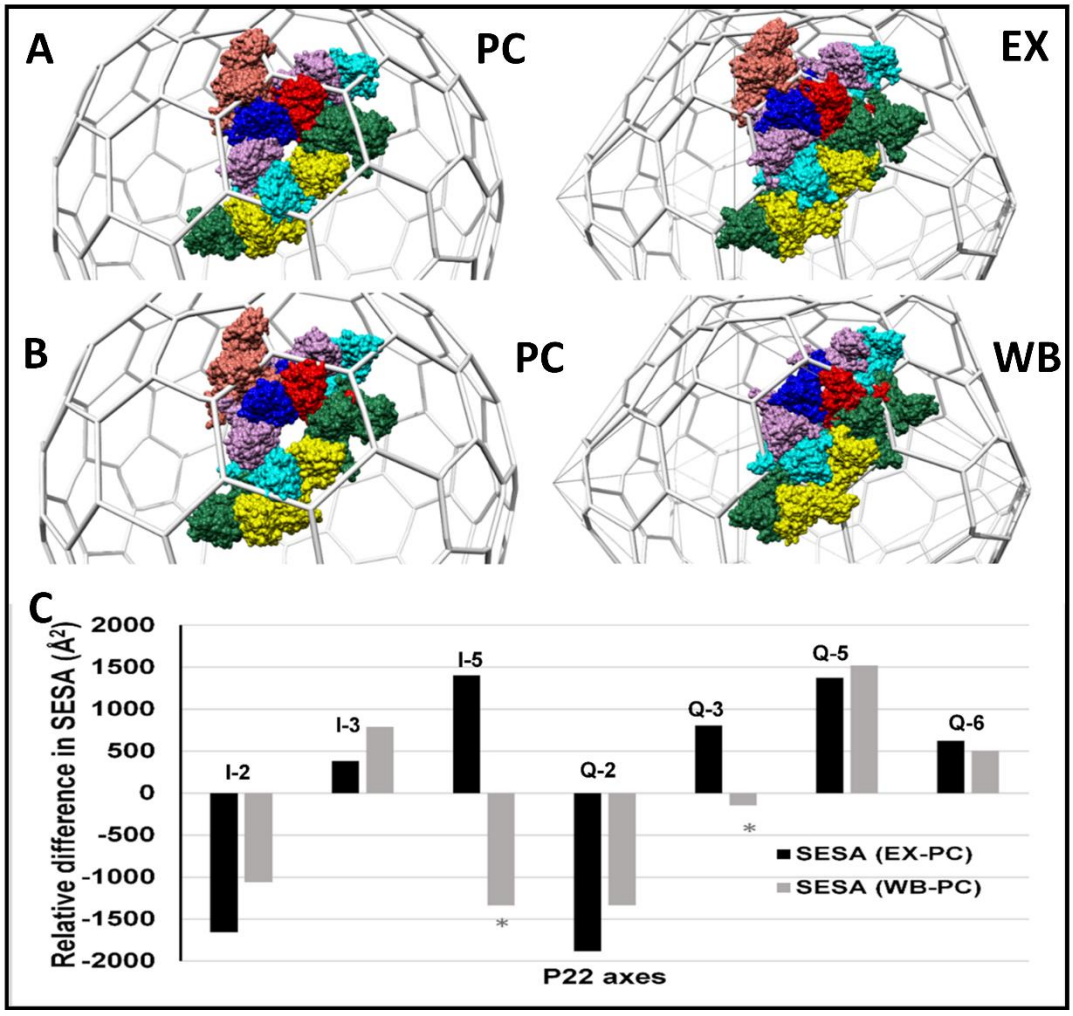


Figure 2.7. Solvent excluded surface area (SESA) of P22 capsids. (A) Spacing filling models of selected subunits show the transformation between PC: 2xyy and EX: 2xyz (2) (B) Spacing filling models of PC: 3iyi and WB: 3iyh (16) display the transition from PC to WB. Absence of pentamers is observed around fivefold in WB. Solvent excluded surface area (SESA) was computed with a probe radius of ~1.4Å for each subunit using UCSF Chimera software (25) after the addition of side chain density. (C) Difference in SESA is calculated and compared across both pairs (2xyy and 2xyz, black color column bar) and (3iyi and 3iyh, grey column bar) along with regular icosahedral axes (I) at 2, 3 and 5 fold and quasi-equivalent (Q) at 2, 3, 5 and 6 fold axes. Numeric SESA values ($Å^2$) is calculated for each axis by averaging all the interacting subunits SESA values at a given axis (Table S2). Differences in averaged SESA for each axis are compared across pairs. Asterisk * at I-5 and Q-3 indicates a reduction in SESA for WB.

Comparative analysis of PC: 2xyy and EX: 2xyz showed a net increase in SESA at both regular icosahedral and quasi-equivalent axis: I3, I5, Q-3, Q-5 and Q-6. The comparison of PC:3iyi and WB 3iyh showed a decrease in SESA at Q-3 and I-5. This was expected, because WB lacks pentamers so residues facing the I-5 axis are more solvent accessible. This is consistent with our HDX on WB, where an increase in deuteriums was observed (Figure 2.6). Structural model SESA analysis corroborated well with HDX data. In spite of this observation, there is a relative increase in SESA at quasi-equivalent axis (Q-5 and Q-6). Hence, quasi-equivalence formation is associated with an increase in SESA suggesting an enhanced hydrophobic core around quasi-axes. This indicates that the expansion is necessary for the attainment of icosahedral geometry which further induces the formation of an enhanced hydrophobic core which is supported by our biochemical experimental data. Therefore, we can say that the expansion of P22 is an important event involving major structural rearrangements mainly at quasi-equivalent axis and responsible for the attainment of important biophysical attributes required for the final stage of maturation.

Maturation Leads to a Decrease in Free Energy by Enhancing Quaternary Interaction

The interrelationship between physical properties (stability, rigidity and solvent accessibility) and maturation can be depicted in the context of an energy landscape (Figure 2.8). The unique shape and architecture of viral capsids is a combination of geometrical principles and free energy minimization. This explains why favorable interactions among capsid proteins results in spontaneous self-assembly into a capsid (58).

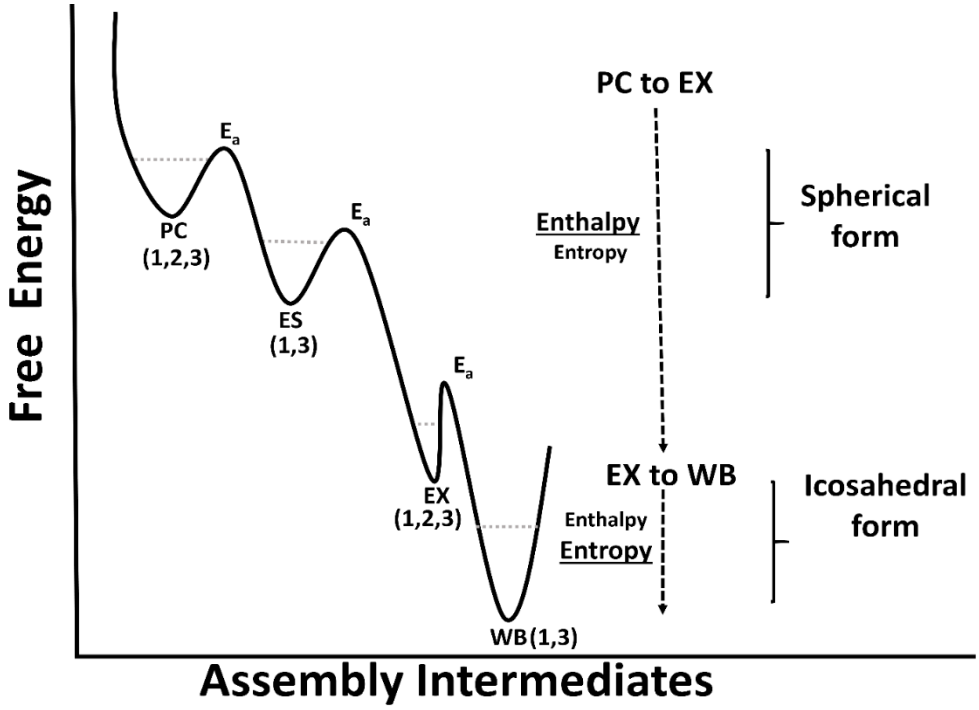


Figure 2.8. Schematic energy landscape of the assembly intermediates of P22. Y axis is free energy and the X axis is the direction of assembly. The broader minima for PC and ES indicate the morphology to less protected and less rigid. The sharp minimum for EX reflects the high rigidity due to an increase in inter-subunit interaction. Biophysical methods supporting the energy landscape are shown by different numbers: DSF (1), AFM (2), HDX (3). E_a represents the activation energy needed to transform into next transition. Underline term represents the driving mechanism stabilizing the corresponding transition.

Formation of a spherical viruses is the natural consequence of free energy minimization. But for icosahedral viruses where hexamers and pentamers coexist, energy state of the viruses is governed by a combination of either enthalpically or entropically driven structural changes during maturation (1–3). Therefore, free energy change as a result of structural transformation from identical to quasi-equivalence should explain the biophysical differences. The relative change in inter-quaternary interactions of a virus during maturation predicts its relative position on an energy land scape. Increased

quaternary interactions result in lowering of the free energy change (18, 33). The broad energy well represents the structure with more flexibility and increased solvent accessibility, while a narrow energy well represents a rigid structure (59).

Based on the results presented above, PC and ES are represented as broad energy wells. This is supported by their greater solvent accessibility and lower rigidity. Our DSF and HDX data showed ES to be slightly more stable and possessing less exchangeable amide hydrogens than PC. Therefore, ES occupied a slightly lower energy position than PC in the landscape (Figure 2.8). Our results have indicated that EX is the most rigid and least solvent accessible morphology which is supported by its lower position in the landscape. The sharp energy minimum for EX reflects the stability, rigidity, brittleness and relative increase in SESA as revealed by DSF, HDX, AFM and structural models. A previous study involving computational analysis of quaternary interactions in icosahedral viruses demonstrated that the association energy is an indicator of stabilities at quasi-equivalent interfaces (60). EX represents a full quasi-equivalence state, therefore, comparison of association energy at different interfaces will address the inter-subunit stability. We extracted the association energy from VIPER (61) and compared across both models (PC:2xyy and EX:2xyz) at common interfaces. We observed a significant increase in association energy which has indicated an increase in stability after quasi-equivalence (Table S2A). Thus, the increase in inter-subunit interactions strongly suggests the free energy stabilization by primarily enthalpically driven mechanism. This interpretation is further supported by a HDX study on P22 where a large protection against deuterium exchange has been observed (10). The protection was distributed throughout the different

parts of coat proteins which resulted in global stabilization, thus supporting the enthalpy driven mechanism.

Our data showed that WB is a less rigid structure and more solvent accessible than EX (Figure 2.5 & 2.6). This is supported by a limited proteolysis study on WB where release of pentamers exposed a cleavage site to Trypsin (23). This proteolytic site was previously shown to be inaccessible in genome filled EX particle (62). But, the DSF results showed the same susceptibility of EX and WB toward heat and denaturant. Similar to EX, comparison of association energy of PC:3iyi and WB:3iyh showed an increase in inter-subunit stability after expansion (Table S2B). AFM data comparisons also showed the highest deformability of WB compared to other P22 morphologies. These results indicate that release of pentamers has added extra elasticity to coat proteins which allow them to adapt and reorganize. This suggests that entropic contributions are responsible for the increased stability of WB. The global minimum energy well for WB is indicated much broader than EX, which represents its higher deformability.

The scheme of maturation is encoded in the amino acid sequence of a coat protein. The coat proteins can arrange into different structures with varying quaternary interactions during maturation. P22 life cycle requires high fidelity during assembly and structural stability at the final stage to withstand high internal pressure imposed by genomic DNA. This balance can be achieved only through regulating inter-subunit interactions at the different stages of assembly. In P22 maturation, this change is regulated by a two-step mechanism. The first step in assembly of P22 is initiated using weaker interactions between coat subunits and scaffold proteins into a spherical procapsid. These weak interactions are

a critical requirement for the precise positioning of coat proteins to avert the formation of aberrant structures and kinetic traps (1–3, 18, 63–66). Hence, the procapsid represents a higher energy local minimum *en-route* to a global minimum (mature capsid). Maturation results in the transformation of structural geometry from spherical to icosahedral with an increase in diameter (17)**.** This transformation resulted in a change in coat protein environment from identical to quasi-equivalent. This conformational switching results in increased subunit interactions, high rigidity, enhanced hydrophobic core and a global minimum.

Conclusions

The thermodynamics and molecular mechanisms behind the assembly and maturation of icosahedral virus capsids are highly complex. By using a suite of orthogonal techniques, we have been able to show that change from identical to quasi-equivalent environment is able to transform the ability of mature P22 capsid to sustain under different stresses. Besides, our studies support a domain interchange model in which after the expansion, domains of neighboring coat proteins interacted with each other to avoid the hydrophobic surface exposure. This model is supported by the lack of structural transitions for expansion during DSF, where the expansion does not involve the transient exposure of hydrophobic residues of coat proteins. Therefore, we are able to put together a mechanism for capsid maturation in which expansion enhances subunit interactions, which expand the hydrophobic core and enhance the high mechanical strength of the global structure. This biophysical transformation must be precisely regulated, with intermediates placed such that

the transformation does not get stalled in a local minimum, en-route to the final quasi-equivalent icosahedral. Comparing with *In-vivo* maturation, where expanded genome filled matured capsid is under high pressure, the expanded capsid need to find a way to accommodate this change. Therefore, here we are suggesting that an increase in mechanical strength is a necessary biophysical transformation necessary for dsDNA viruses expansion. Further comparison P22 and HK97 maturation, we now also propose a recurrent theme and suggesting that such transformation may not only be a conserve mechanism for dsDNA phages infecting bacteria, rather such biomechanical transformations are likely to be found in other dsDNA viruses such as adenovirus and herpes virus. Above discussed biophysical methods are not only having the potential to characterize a P22 capsid, but also for the cargo filled P22 capsids. Therefore, a suite of techniques, we presented here, can be applied to characterize other unexplored natural viruses as well as synthetic-capsids.

References

1. Zlotnick A. 2003. Are weak protein-protein interactions the general rule in capsid assembly? Virology 315:269–274.

2. Ceres P, Zlotnick A. 2002. Weak protein-protein interactions are sufficient to drive assembly of hepatitis B virus capsids. Biochemistry 41:11525–11531.

3. Zlotnick A. 2005. Theoretical aspects of virus capsid assembly. J Mol Recognit 18:479–490.

4. Bothner B, Taylor D, Jun B, Lee KK, Siuzdak G, Schultz CP, Schlutz CP, Johnson JE. 2005. Maturation of a tetravirus capsid alters the dynamic properties and creates a metastable complex. Virology 334:17–27.

5. Prevelige PE, Thomas D, Aubrey KL, Towse S a, Thomas GJ. 1993. Subunit conformational changes accompanying bacteriophage P22 capsid maturation. Biochemistry 32:537–543.

6. Tuma R, Coward LU, Kirk MC, Barnes S, Jr PEP, Al B. 2001. Hydrogen-deuterium Exchange as a Probe of Folding and Assembly in Viral Capsids 389–396.

7. Conway JF, Wikoff WR, Cheng N, Duda RL, Hendrix RW, Johnson JE, Steven a C. 2001. Virus maturation involving large subunit rotations and local refolding. Science 292:744–748.

8. Lewis JK, Bothner B, Smith TJ, Siuzdak G. 1998. Antiviral agent blocks breathing of the common cold virus. Proc Natl Acad Sci U S A 95:6774–6778.

9. Speir J a, Bothner B, Qu C, Willits D a, Young MJ, Johnson JE. 2006. Enhanced local symmetry interactions globally stabilize a mutant virus capsid that maintains infectivity and capsid dynamics. J Virol 80:3582–91.

10. Lin J, Lee LY, Roivainen M, Filman DJ, Hogle JM, Belnap DM. 2012. Structure of the Fab-Labeled “Breathing” State of Native Poliovirus. J Virol 86:5959–5962.

11. Kale A, Bao Y, Zhou Z, Prevelige PE, Gupta A. 2013. Directed self-assembly of CdS quantum dots on bacteriophage P22 coat protein templates. Nanotechnology 24:045603.

12. Kang S, Uchida M, O’Neil A, Li R, Prevelige PE, Douglas T. 2010. Implementation of p22 viral capsids as nanoplatforms. Biomacromolecules 11:2804–9.

13. Patterson DP, Schwarz B, El-Boubbou K, van der Oost J, Prevelige PE, Douglas T. 2012. Virus-like particle nanoreactors: programmed encapsulation of the

thermostable CelB glycosidase inside the P22 capsid. Soft Matter 8:10158.

14. King J, Botstein D, Casjens S, Earnshaw W, Harrison S, Lenk E. 1976. Structure and assembly of the capsid of bacteriophage P22. *Phil. Trans.R.Soc.Lond*. B. 276, 37-49.

15. Casjens S, Adams MB, Hall C, King J. 1985. Autogenous Modulation of Bacteriophage 123:174–179.

16. Tatnall M, King J. 1981. Purification of the Coat and Scaffolding Procapsids of Bacteriophage Proteins from 547:529–547.

17. Prevelige PE, Thomas D, King J. 1988. Scaffolding protein regulates the polymerization of P22 coat subunits into icosahedral shells in vitro. J Mol Biol 202:743–757.

18. Johnson JE. 1996. Functional implications of protein-protein interactions in icosahedral viruses. Proc Natl Acad Sci 93 :27–33.

19. Earnshaw W, Casjens S, Harrison SC. 1976. Assembly of the head of bacteriophage P22: X-ray diffraction from heads, proheads and related structures. J Mol Biol 104:387–410.

20. Capen CM, Teschke CM. 2000. Folding defects caused by single amino acid substitutions in a subunit are not alleviated by assembly. Biochemistry 39:1142–1151.

21. Galisteo ML, King J. 1993. Conformational transformations in the protein lattice of phage P22 procapsids. Biophys J 65:227–35.

22. Lucon J, Qazi S, Uchida M, Bedwell GJ, Lafrance B, Jr PEP, Douglas T. 2012. polymerization with high-density cargo loading. Nature Chem 4:781–788.

23. Parent KN, Khayat R, Tu LH, Suhanovsky MM, Cortines JR, Teschke CM, Johnson JE, Baker TS. 2010. P22 coat protein structures reveal a novel mechanism for capsid maturation: stability without auxiliary proteins or chemical crosslinks. Structure 18:390–401.

24. Teschke CM, McGough A, Thuman-Commike P a. 2003. Penton release from P22 heat-expanded capsids suggests importance of stabilizing penton-hexon interactions during capsid maturation. Biophys J 84:2585–92.

25. Speir J a, Munshi S, Wang G, Baker TS, Johnson JE. 1995. Structures of the native and swollen forms of cowpea chlorotic mottle virus determined by X-ray crystallography and cryo-electron microscopy. Structure 3:63–78.

26. Hendrix RW, Johnson JE. 2012. Viral Molecular Machines 726:351–363.

27. Wikoff WR, Liljas L, Duda RL, Tsuruta H, Hendrix RW, Johnson JE. 2000. Topologically linked protein rings in the bacteriophage HK97 capsid. Science 289:2129–2133.

28. Duda RL. 1998. Protein chainmail: Catenated protein in viral capsids. Cell 94:55–60.

29. Roos WH, Gertsman I, May ER, Brooks CL, Johnson JE, Wuite GJL. 2012. Mechanics of bacteriophage maturation. Proc Natl Acad Sci 109:2342–2347.

30. Rayaprolu V, Kruse S, Kant R, Venkatakrishnan B, Movahed N, Brooke D, Lins B, Bennett A, Potter T, McKenna R, Agbandje-McKenna M, Bothner B. 2013. Comparative Analysis of Adeno Associated Virus Capsid Stability and Dynamics. J Virol.

31. Kuznetsov YG, McPherson A. 2011. Atomic force microscopy in imaging of viruses and virus-infected cells. Microbiol Mol Biol Rev 75:268–285.

32. Roos WH, Ivanovska IL, Evilevitch a., Wuite GJL. 2007. Viral capsids: Mechanical characteristics, genome packaging and delivery mechanisms. Cell Mol Life Sci 64:1484–1497.

33. Tuma R, Prevelige PE, Thomas GJ. 1998. Mechanism of capsid maturation in a double-stranded DNA virus. Proc Natl Acad Sci U S A 95:9885–90.

34. Wang L, Lane LC, Smith DL. 2001. Detecting structural changes in viral capsids by hydrogen exchange and mass spectrometry. Protein Sci 10:1234–1243.

35. Kang S, Poliakov A, Sexton J, Renfrow MB, Jr PEP. 2008. Probing Conserved Helical Modules of Portal Complexes by Mass Spectrometry-based Hydrogen / Deuterium Exchange 772–784.

36. Kang S, Prevelige PE. 2005. Domain study of bacteriophage p22 coat protein and characterization of the capsid lattice transformation by hydrogen/deuterium exchange. J Mol Biol 347:935–48.

37. Hernando-Pérez M, Lambert S, Nakatani-Webster E, Catalano CE, de Pablo PJ. 2014. Cementing proteins provide extra mechanical stabilization to viral cages. Nat Commun 5:4520.

38. Kelley LA, Mezulis S, Yates CM, Wass MN, Sternberg MJE. 2015. The Phyre2 web portal for protein modeling, prediction and analysis. Nat Protoc 10:845–858.

39. Xu D, Zhang Y. 2011. Improving the physical realism and structural accuracy of

protein models by a two-step atomic-level energy minimization. Biophys J 101:2525–2534.

40. Pettersen EF, Goddard TD, Huang CC, Couch GS, Greenblatt DM, Meng EC, Ferrin TE. 2004. UCSF Chimera - A visualization system for exploratory research and analysis. J Comput Chem 25:1605–1612.

41. Niesen FH, Berglund H, Vedadi M. 2007. The use of differential scanning fluorimetry to detect ligand interactions that promote protein stability. Nat Protoc 2:2212–21.

42. Rayaprolu V, Kruse S, Kant R, Venkatakrishnan B, Movahed N, Brooke D, Lins B, Bennett A, Potter T, McKenna R, Agbandje-McKenna M, Bothner B. 2013. Comparative Analysis of Adeno Associated Virus Capsid Stability and Dynamics. J Virol.

43. Zhang Z, Greene B, Thuman-Commike P a, Jakana J, Prevelige PE, King J, Chiu W. 2000. Visualization of the maturation transition in bacteriophage P22 by electron cryomicroscopy. J Mol Biol 297:615–26.

44. Zandi R, Reguera D. 2005. Mechanical properties of viral capsids. Phys Rev E - Stat Nonlinear, Soft Matter Phys 72.

45. Canady M a, Tihova M, Hanzlik TN, Johnson JE, Yeager M. 2000. Large conformational changes in the maturation of a simple RNA virus, nudaurelia capensis omega virus (NomegaV). J Mol Biol 299:573–584.

46. RF G, CN P. 1974. Urea and guanidine hydrochloride denaturation curves. J Biol Chem 249:5388–5393.

47. Pace CN, Vanderburg KE. 1979. Determining globular protein stability: guanidine hydrochloride denaturation of myoglobin. Biochemistry 18:288–292.

48. Monera OD, Kay CM, Hodges RS. 1994. Protein denaturation with guanidine hydrochloride or urea provides a different estimate of stability depending on the contributions of electrostatic interactions. Protein Sci 3:1984–1991.

49. England JL, Haran G. 2011. Role of solvation effects in protein denaturation: from thermodynamics to single molecules and back. Annu Rev Phys Chem 62:257–277.

50. Tuma R, Prevelige PE, Thomas GJ. 1998. Mechanism of capsid maturation in a double-stranded DNA virus. Proc Natl Acad Sci U S A 95:9885–9890.

51. Asghar A, Buzari B, Pavelkic V, Gopcevic K, Petkovic M, Bordbar A. 2013. Thermochimica Acta Thermal denaturation of pepsin at acidic media : Using DSC , MALDI-TOF MS and PAGE techniques. Thermochim Acta 568:165–170.

52. Lanman J, Tuma R, Prevelige PE. 1999. Identification and characterization of the domain structure of bacteriophage P22 coat protein. Biochemistry 38:14614–23.

53. Chen D-H, Baker ML, Hryc CF, DiMaio F, Jakana J, Wu W, Dougherty M, Haase-Pettingell C, Schmid MF, Jiang W, Baker D, King J a, Chiu W. 2011. Structural basis for scaffolding-mediated assembly and maturation of a dsDNA virus. Proc Natl Acad Sci U S A 108:1355–1360.

54. Mateu MG. 2012. Mechanical properties of viruses analyzed by atomic force microscopy: A virological perspective. Virus Res 168:1–22.

55. Llauro A, Guerra P, Irigoyen N, Rodriguez JF, Verdaguer N, De Pablo PJ. 2014. Mechanical stability and reversible fracture of vault particles. Biophys J 106:687–695.

56. Lazarus A, Florijn HCB, Reis PM. 2012. Geometry-induced rigidity in nonspherical pressurized elastic shells. Phys Rev Lett 109:1–5.

57. Bai Y, Milne JS, Mayne L, Englander SW. 1993. Primary structure effects on peptide group hydrogen exchange. Proteins 17:75–86.

58. Nguyen TT, Bruinsma RF, Gelbart WM. 2005. Elasticity theory and shape transitions of viral shells. Phys Rev E - Stat Nonlinear, Soft Matter Phys 72:1–19.

59. Tuma R, Tsuruta H, Benevides JM, Prevelige PE, Thomas GJ. 2001. Characterization of subunit structural changes accompanying assembly of the bacteriophage P22 procapsid. Biochemistry 40:665–74.

60. Reddy VS, Giesing H a, Morton RT, Kumar a, Post CB, Brooks CL, Johnson JE. 1998. Energetics of quasiequivalence: computational analysis of protein-protein interactions in icosahedral viruses. Biophys J 74:546–558.

61. Carrillo-Tripp M, Shepherd CM, Borelli IA, Venkataraman S, Lander G, Natarajan P, Johnson JE, Brooks CL, Reddy VS. 2009. VIPERdb2: an enhanced and web API enabled relational database for structural virology. Nucleic Acids Res 37:D436–42.

62. Lanman J, Tuma R, Prevelige PE. 1999. Identification and characterization of the domain structure of bacteriophage P22 coat protein. Biochemistry 38:14614–23.

63. Schwartz R, Shor PW, Prevelige PE, Berger B. 1998. Local Rules Simulation of the Kinetics of Virus Capsid Self-Assembly. Biophys J 75:2626–2636.

64. Moerman PG, van der Schoot P, Kegel WK. 2016. Kinetics versus Thermodynamics in Virus Capsid Polymorphism. J Phys Chem B acs.jpcb.6b01953.

65. Parent KN, Doyle SM, Anderson E, Teschke CM. 2005. Electrostatic interactions

govern both nucleation and elongation during phage P22 procapsid assembly. Virology 340:33–45.

66. Parker MH, Stafford WF, Prevelige PE. 1997. Bacteriophage P22 scaffolding protein forms oligomers in solution. J Mol Biol 268:655–65.

CHAPTER 3

UNDERSTANDING OF P22 BACTERIOPHAGE MATURATION BY QCM-D

Contribution of Authors and Co-Authors

Manuscript in Chapter 3

Author: Ravi Kant

Contributions: Data collection and Analysis, Manuscript preparation

Co-Author: Vamseedhar Rayaprolu

Contributions: Aided in data collection

Co-Author: Brian Bothner

Contributions: Obtained funding, provided critical intellectual input and mentoring, discussed data and the manuscript

Manuscript Information Page

UNDERSTANDING OF P22 BACTERIOPHAGE MATURATION BY QCM-D

Authors: Ravi Kant, Vamseedhar Rayaprolu, Brian Bothner

Journal:

Status of Manuscript:
__x_ Prepared for submission to a peer-reviewed journal
____ Officially submitted to a peer-review journal
____ Accepted by a peer-reviewed journal
____ Published in a peer-reviewed journal

Publisher:

Issue in which Manuscript Appears: In Preparation

CHAPTER 3

UNDERSTANDING OF P22 BACTERIOPHAGE MATURATION BY QCM-D

Abstract

QCM-D is an established method to understand adsorption of proteins such as biomaterials and therapeutic diagnostics. We have extended the application of this technique to understand biophysical changes in a tailed bacteriophage P22. We show an increase in rigidity after expansion from the frequency and dissipation ratio. We also extend the study to viscoelastic modeling using Voigt model. We show an increase in elastic modulus, viscosity and thickness after expansion. Our modeling suggests that QCM-D technique has a potential to explore the biophysical properties for other complicated macromolecular complexes.

Introduction

There are approximately 10^{31} viruses to be present in the biosphere (1). They come in a variety of shapes and sizes including filaments, bullet-shaped, irregular and spherical. Among viruses, the most abundant are the tailed double stranded DNA bacteriophages (1, 2). Nearly 50% of the them are spherical, usually icosahedral and they display a unique maturation mechanism (3). Assembly of an icosahedral capsid is regulated by sequential and highly coordinated inter-coat proteins interaction. Investigating the assembly mechanism requires an understanding about the mode of assembly for different virus system which includes the formation of oligomers or direct assembly into structural

intermediates (2–5) (6). *In-vitro* assembly systems mimicking *in-vivo* processes have provided the opportunity to understand important biological processes. Icosahedral viruses have been under investigation for many decades. Two of the most well studies systems are HK 97 phage (7–9) and P22 phage (10–12).

Despite the long history of investigation, methods for studying the biophysical properties of nano-sized megadalton viruses remains a daunting task. Investigation of structural transformations are very crucial to understand the proper functioning and biology of a virus life cycle. Any defect during assembly may lead to the loss of biological function or infectivity in viral capsids (3, 13). Viruses maintain the dynamic relationship between stability and structural integrity to ensure partial instability at the time of release of nucleic acids. Virus achieve this event by altering the mechanical stability at different stages of maturation. The biomechanical study (change in rigidity) has been conducted across a few virus system in the icosahedral class (14). Biomechanical studies are primarily studied in viruses by single particle techniques such as atomic force microscopy (AFM). The most studied system are *Paramecium bursaria* chlorella virus type 1 (a large algal virus), Cowpea chlorotic mottle virus (a plant virus) and HK 97 (bacteriophage) (15–20). Other bulk techniques like QCM-D (quartz crystal microbalance with dissipation) has not been explored much to understand and compare the rigidity among viruses.

P22 bacteriophage is a model virus system for understanding the mechanism and driving forces behind icosahedral virus capsid assembly. However, even after years of investigation, changes in particle rigidity during structural transitions are not thoroughly understood. P22 is a T=7 bacteriophage which infect *Salmonella typhimurium* and the

assembly of this phage is initiated as procapsid. Procapsid assembly is regulated by the interaction and co-polymerization of 400 coat proteins and 60-300 scaffold proteins. Others accessory proteins (12 portal proteins and 3 ejection proteins) are also reported to assist in the formation of metastable procapsid (21, 22). Subsequently, Incorporation of genomic DNA in procapsid is regulated by an ATP dependent terminase. During packaging, the characteristic changes involve in procapsid are the release of internal scaffold proteins and 10% capsid expansion. Expansion results in large scale structural rearrangements and transformation in morphology from spherical to icosahedral form (6, 23, 24).

Study of the mechanism behind P22 maturation is possible due to an *in-vitro* system mimicking *in-vivo* transitions. Procapsid is assembled by the heterologous expression of coat and scaffold proteins in *E.coli* (25). When ES is heated for 20 minutes at 65 ^{O}C, capsid is expanded to form expanded shell (EX) (22, 26, 27). Another expanded morphology termed as WB can be achieved by heating the ES 20 minutes at 75 ^{O}C (11, 22, 26, 27). PC and ES are spherical in shape with the diameter 58nm. Morphology EX and WB are icosahedral in symmetry with diameter 64nm (Figure 3.1A). These morphological transformation are irreversible. This complex cycle of P22 maturation asks for obvious questions: “how the structural rigidity do changes along the course of expansion in P22 phage?” To really understand it, we need to know that “What is the difference between spherical and icosahedral capsid?” how the global rearrangements at different stage of maturation influence the global rigidity? Many research studies have inferred that in-vivo and *in-vitro* expanded particle are remarkably similar, thus all the studies on these *in-vitro* morphology are authentic to understand the biophysical transformation (11, 26). PC, ES

are structural intermediates while EX and WB are the matured form of P22 (Figure 3.1B). To characterize the biophysical change in the structural transitions, we have implemented a bulk measurement technique QCM-D on PC, ES, EX and WB.

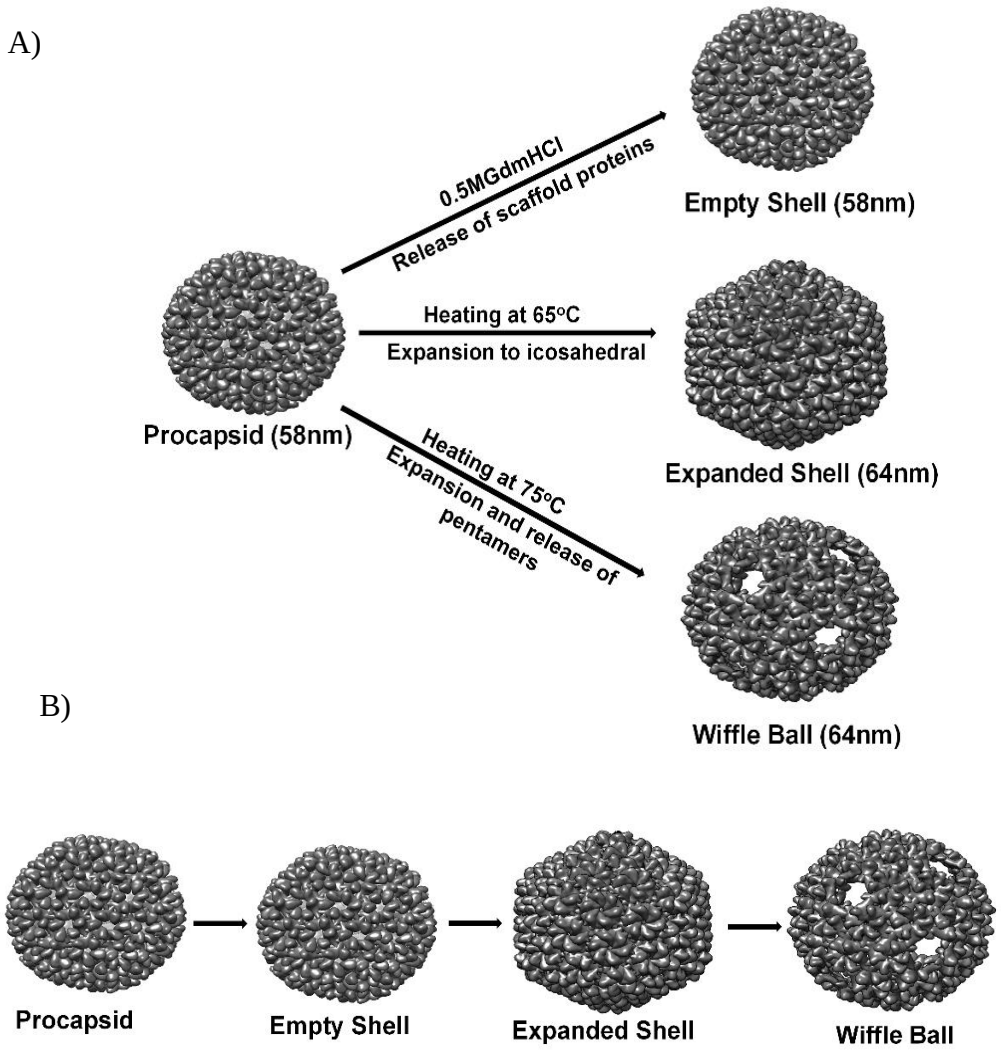


Figure 3.1. A) *in-vitro* maturation of P22 morphology. Procapsid is assembled from coat and scaffold proteins. Empty shell is generated by incubating procapsid in 0.5M guanidium hydrochloride (GdmHCl). Expanded shell and Wiffle ball are generated by heating procapsid at 65 ^{0}C and 75 ^{0}C for 20 minutes respectively. B) P22 capsid maturation pathway.

Making Viscoelastic Measurements Using QCM-D

QCM is a technique utilizing acoustic waves generated by a piezoelectric quartz crystal. Resonance in QCM occurs when the standing wave generated by alternating expansion and contraction is an odd integer of the thickness of gold coated quartz crystal. QCM has been established as an important balance technique based on Sauerbrey equation (Sauerbrey, 1959). It describes a linear relationship between change in frequency (Δf) and mass deposited (Δm).

$$\Delta m = \frac{C}{n}\,\Delta f \qquad C = \frac{t_q \rho_q}{f_0}$$

n =harmonic number and

Where t_q , ρ_q and f_0 represent the thickness, density and resonant frequency of the quartz crystal respectively. The Sauerbrey equation is based on three assumptions. 1. Relative mass of adsorbed material should be smaller than the mass of the quartz crystal. 2. Adsorbed mass be rigid. 3. Mass is evenly distributed over the crystal (28). A drawback of QCM measurements in liquid phase is that it often incorporates viscous and elastic contributions and thus violates a primary assumption of Sauerbrey model. The limitations of Sauerbrey equation prompted new models to addresses changes associated with viscoelastic materials. To address the adsorption related changes due to viscoelastic materials, dissipation (D) was introduced. A viscoelastic material related dissipation (D) were monitored by measuring decay of oscillation frequency after a rapid excitation at resonating frequency (29). This decay is proportional to energy dissipation of the oscillating quartz crystal (30). QCM-D (advanced version of QCM) measures both change in frequency and dissipation. QCM-D measurement follows the principle in which when

the driving power is switched off, the voltage decays as an exponential damped sinusoidal (31).

$$A(t) = A_0 e^{-t/\tau} \sin(2\pi f t + \varphi),$$

Where A_0= amplitude at t=0, τ= decay time constant and φ is the phase. D is related to decay time constant as follows

$$D = \frac{1}{\pi f \tau} \qquad D = \frac{1}{Q} = \frac{E_{Dissipated}}{2\pi E_{Stored}}$$

D is dimensionless and Q being the quality factor.

It measures both change in frequency and dissipation from an oscillating gold. Change in frequency at different overtones measures changes in the mass attached to surface, while (ΔD) relates to viscoelastic properties of the adsorbed layer (32–34). Rigid materials, when bound to oscillating crystals, exhibits low dissipation due to strong coupling, while soft materials due to weak coupling undergoes more deformation results in high dissipation (35).

Here we have initiated a comparative study of the different forms of P22 capsids using QCM-D. The forms analyzed are conducted on PC, ES, EX and WB showed that release of scaffold don't alter the capsid characteristics. But expansion results in major global rearrangements which leads to increase an increase in rigidity, viscosity and particle diameter.

Materials and Methods

Protein Purification of WT P22

P22 purification is explained in chapter 2 (material and method section).

QCM-D Experiment

The adsorption properties of different P22 morphologies (PC, ES, EX & WB) were explored by using QCM-D (Q-Sense D300 system, Q-Sense AB, Goteborg, Sweden). For these measurements, gold coated quartz crystal (AT cut) with a fundamental resonant frequency of 5MHz was used. Baseline was established with PBS buffer and recorded for 10 minutes. P22 samples (0.01mg/mL, 0.6mL, PBS buffer at pH 7) were then gradually deposited on the crystal and allowed it to stabilize for 45min. To remove the loosely bound viral particles, gold surface was then washed with 0.6mL of same buffer for 10min.

After every run the gold surface was cleaned and regenerated by soaking the crystal in a 1:1:5 mixture of H_2O_2 (30%), NH_3 (25%), and distilled water at 60^{o}C for 15min followed by exposure to UV light in UV chamber for 10 min. All four samples were run in random order in triplicate and every time fresh cleaned crystal was used. Frequency and dissipation values were obtained at fundamental frequency 5MHz and three overtones (15MHz, 25MHz and 35MHz).

Viscoelastic Modeling

After frequency and dissipation extraction for three overtones, data modeling and analysis were carried out with the Q sense Qtool 3.0. Both Sauerbrey and Viscoelastic model could be selected for data modeling. Sauerbrey equation assumes that adsorbed mass to be uniform, rigid and thin film and it follows a linear function of frequency change. Use of Sauerbrey equation is limited and it underestimate the adsorbed mas, when an increase in dissipation is observed. Since adsorption of P22 samples resulted in increased dissipation and hence Sauerbrey used is limited for P22 data modeling. To overcome this limitation,

Voigt model was implemented which is a simple representation of viscoelastic solid. By fitting the QCM-D data for all three overtones (n = 3, 5 and 7) with Voigt model, thickness, shear viscosity and shear modulus can be obtained. In data modeling fixed parameters were set as follows: fluid density (kg/m^3) = 1000, fluid viscosity (kg/ms) = 0.001, P22 density (kg/m^3) = 1100. Data fitting were also performed using three overtones (n=3, 5 and 7). Variable parameters were L1 visc [kg/ms]:0.0005 to 0.01, L1 shear [Pa]: 100 to 1E8 and thickness [m]: 1E-15 to 1E-6. Fitting were performed by applying different iteration steps to ensure a stable fit is obtained.

Results and Discussion

Capsid Rigidity Increases After Expansion

To determine if there was a change in rigidity associated with capsid maturation, PC, ES and EX and WB were deposited onto oscillating gold coated quartz crystal in q-sense D300 instrument. Figure 3.2 shows the typical QCM-D curve showing the decrease in frequency (Y1 axis in black), increase in dissipation (Y2 axis in gray) and time (min) at x axis. Change in frequency Δf and dissipation ΔD were measured simultaneously at three different overtones (n = 3, 5, and 7). After a stable base line with buffer was obtained, P22 particles were allowed to adsorb to the crystal for 45min. This was followed by a wash step to remove loosely bound virus particles. Again a stable line after wash step indicated a strong adsorption of P22 virus particles onto gold surface. To compare and measure the capsid rigidity, change in frequency and dissipation was extracted for each morphology.

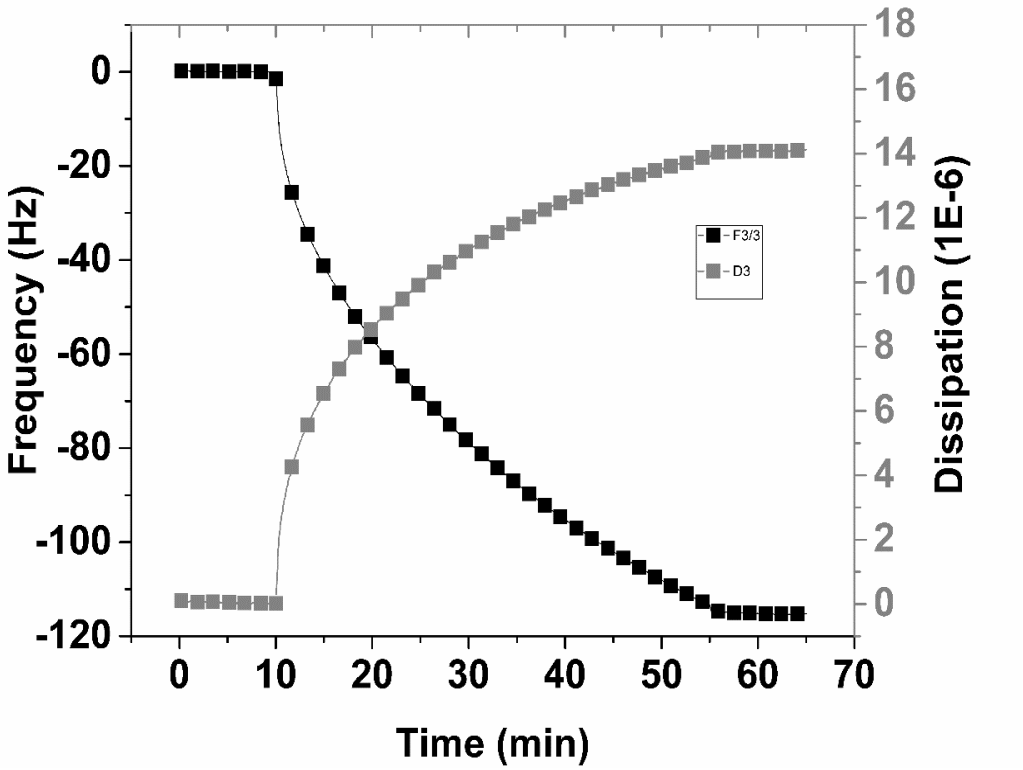


Figure 3.2. Typical QCMD spectra representing the change in frequency and dissipation along with time. Overtone (3^{rd}) of WB is represented. X axis shows the time (minutes), Y1 axis shows the decrease in the frequency corresponding to mass deposited onto gold quartz crystal. Y2 axis shows the increase in dissipation.

Rigidity is calculated from frequency/dissipation ratio of Third overtone data. Procapsid showed a $\Delta f/ \Delta D$ ratio of 6.03 ± 0.08, whereas empty shell showed a ratio of 6.16 ± 0.1. There is no observed significant difference in the rigidity from PC to ES transition. However, EX showed a ratio of 7.62 ± 0.08 which indicates that transition from PC/ES to EX leads to increase in rigidity by approximately 19%. The $\Delta f/ \Delta D$ ratio of WB showed a ratio of 8.13 ± 0.08, which indicates that WB is the relatively more rigid than other morphological forms (Table 3.1). This shows that rigidity of expanded particles (WB,

EX) are much higher than unexpanded particles (PC, ES). Globally, increase in rigidity follows the following order PC/ES<EX<WB.

Table 3.1. QCM-D data of different P22 morphology

P22 samples	$\|\Delta f/\Delta D\|$ at 15 MHz	Diameter (nm)
P22_PC	6.03 ± 0.08	58
P22_ES	6.16 ± 0.14	58
P22_EX	7.62 ± 0.08	64
P22_WB	8.13 ± 0.08	64

Relative increase in $\Delta f / \Delta D$ ratio is also an indicator of increased protein interaction in an icosahedral capsid. The viscoelastic properties changes are related to in the dynamics of the proteins which is evident from CCMV structural transitions. A previous report on QCM-D confirmed that closed form of CCMV is more rigid ($\Delta f / \Delta D$ = 15.4 MHz) than swollen form ($\Delta f / \Delta D$ = 12.9 MHz). It is explained that in swollen form, virus undergoes fenestration and resulting in increased of surface area by 5%. This expansion suggests that reduced subunit-subunit interaction decreased the rigidity of the entire particle (36, 37). Therefore, we suggest that transition from PC/ES to EX/WB results in structural rearrangements plausibly involving increased in coat protein interactions.

Voigt Viscoelastic Modeling

Ratio of $\Delta f / \Delta D$ only provides qualitative information about P22 capsids. QCM-D data has a potential to provide quantitative information than $\Delta f/\Delta D$ ratio of these capsid. Therefore, QCM-D data was further analyzed using Voigt-based viscoelastic model (38). This model describes the propagation and damping of shear bulk acoustic waves in an uniformly adsorbed viscoelastic material which is in contact with bulk Newtonian fluid under no slip condition (38–40). This model allows the conversion of change in frequency Δf and dissipation ΔD numbers into three important global biophysical parameters: thickness of the layer, shear viscosity (ηVoigt), and shear modulus (μVoigt) (41, 42). All three overtones n= 3, 5 and 7 were subjected to data modeling with the parameters defined in the method section. Data was allowed to fit at different iteration steps with the defined set of parameters (see method section) to ensure the global minima is reached for each data set. Figure 3.3 shows the comparison of raw data and Voigt model fit of procapsid, empty shell, expanded shell and expanded shell. The graph showed that raw and modeled data corresponded well that suggests the model worked well and a good fit was observed. Shear modulus, viscosity and layer thickness were obtained from Voigt model and compared.

Expansion Leads to Shear Modulus

Comparison of shear modulus across P22 morphology showed no significant change in shear modulus from PC to ES transition suggesting that release of scaffold proteins has no effect on global rigidity of PC (Figure 3.4). Results were more exciting for EX where a significant increase in shear modulus (rigidity) was observed. These results suggest a major structural rearrangement after expansion.

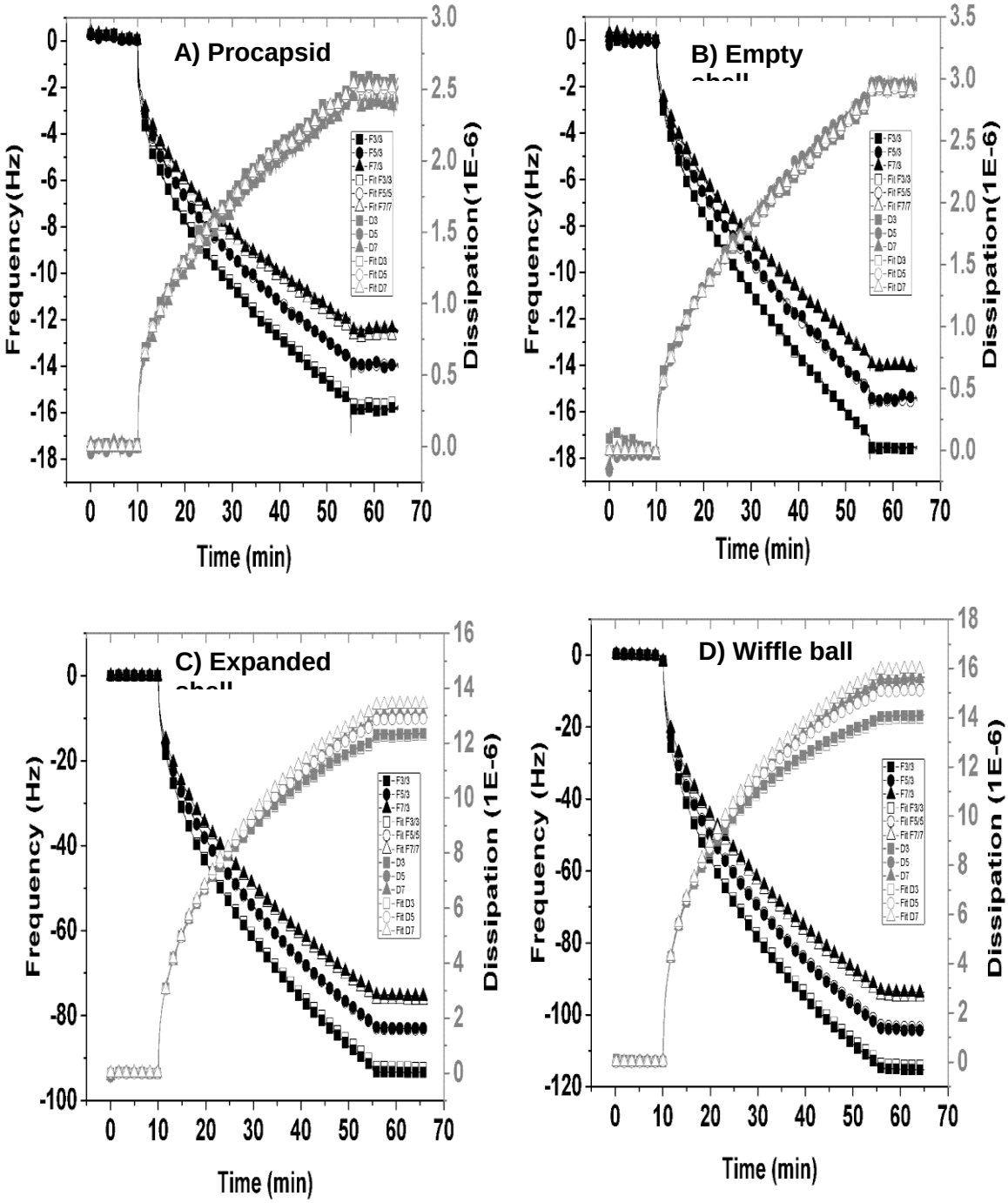


Figure 3.3. Representation fit of QCMD raw data and modeled Voigt across different P22 morphology A) Procapsid B) Empty shell C) Expanded shell and D) Wiffle ball

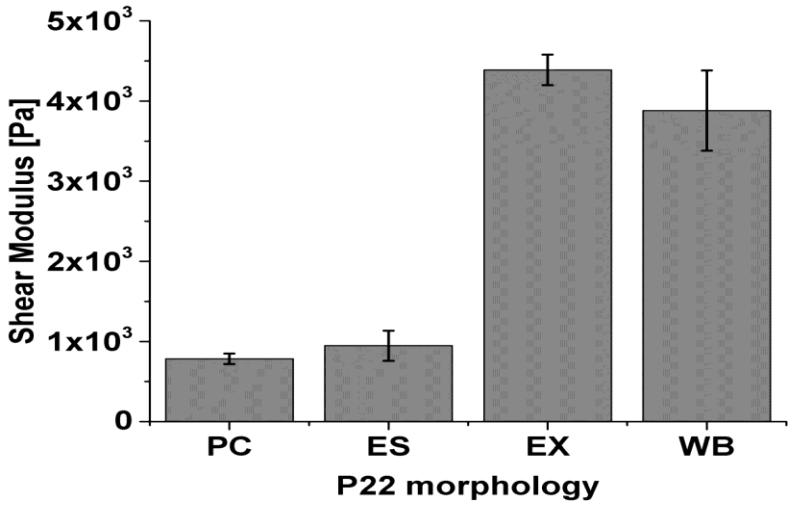


Figure 3.4. Shear modulus obtained from Voigt model is represented and compared across all morphology of P22.

Up to this point, shear modulus trend followed with the $\Delta f / \Delta D$ ratio (PC/ES<EX). However modeling results for WB was slightly conflicting, where a relative decrease in shear modulus is observed for WB. This results wasn't expected earlier as $\Delta f / \Delta D$ showed an increase in rigidity for WB. Though the result was unexpected but not too surprising. A previous study have shown the presence of pentamers as architectural defect. According to continuum elasticity theory, pentamers in icosahedral lattice at fivefold axis exert high lateral compression in the lattice. This stress increases with the complexity (Triangulation number) of viruses (43). Therefore, release of pentamers at fivefold axis relaxes the strain from the icosahedral virus and EX particles become softer (less rigid), hence a relative reduction in rigidity from EX to WB was observed (Figure 3.4).

QCM-D studies including Voigt modeling have not been implemented to understand regular proteins and protein complexes. Numeric values of shear modulus have

been reported only in a few studies (42, 44, 45). For example: comparison of elastic shear modulus of P22 across limited studies showed different trends. A study on laminin (a cell adhesive protein) by QCM-D have shown the elastic modulus of 8 kPa on the homogenous surface (45). In contrast to above example, shear modulus of P22-EX is approximately an order of magnitude smaller than Mytilys edilus foot protein (Mefp). In this study, authors compared non-cross and cross linked protein, and as a result a substantial increase in the elastic shear modulus and shear viscosity is observed. The difference is not very surprising Mefp can form a thin film of 20nm that results in increased rigidity (42). These studies have also suggested that smaller range shear modulus output is consistent with higher level of hydration level. P22 capsid is an ensemble of 420 interacting proteins and therefore expected to be heavily hydrated. Therefore, the shear modulus output obtained for P22 capsids is in lower range of kPa value.

Expansion Leads to Increase in Viscosity

Viscosity comparison of P22 morphology showed an increase in viscosity in the following order PC/ES<EX<WB (Figure 3.5). Increase in viscosity can be explained by decreased flexibility in a protein. A previous study on poly-L-lysine have showed that the alpha helix form is more viscous than β sheet. This increase may arise owing to intrastrand hydrogen in alpha helix bonding in poly-L-lysine. Intrastrand hydrogen bonding also resulted in the decreased back bone flexibility in a peptide (46). Therefore increase in viscosity can reflect information about reduced flexibility of a protein. This interpretation is well supported for our observation by cryoEM study on expanded P22 capsid. This model has suggested a relative increase in intracapsomere after capsid expansion (47).

Therefore, increase in viscosity after expansion can be interpret as the decreased back bone flexibility of EX and WB after expansion.

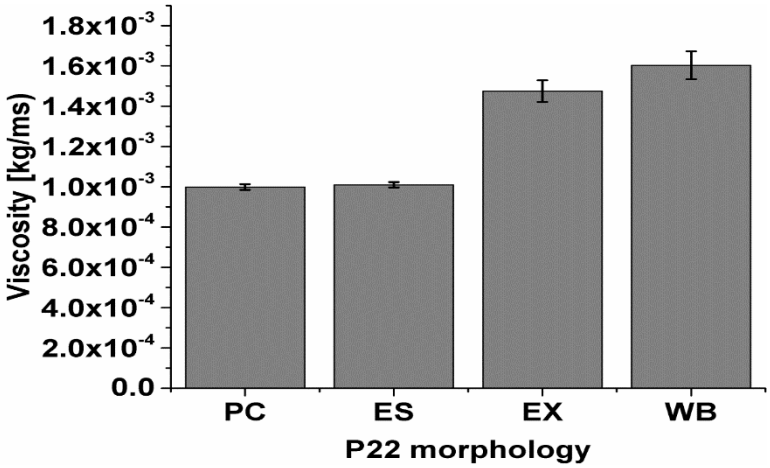


Figure 3.5. Modeled viscosity value obtained from Voigt model is represented for all four morphology of P22.

Expansion Leads to Increase in Thickness

Voigt model predicted an increase in layer thickness after expansion. The increasing order of layer thickness follows as PC/ES<EX<WB (Figure 3.6). Both PC and ES thickness were ~50nm while for EX was 56nm and WB was 60nm. Modeled thickness number was slightly less (4 to 8nm range) than reported for P22 capsid diameters (27, 48–50). This decrease is expected as particles were adsorb onto surface, a little distortion as a result of capsid and gold surface interaction is expected which may in turn affect the modeled output thickness. Closeness of modeled thickness and diameter strongly suggests that capsids were forming monolayer onto gold quartz surface (Table 3.1). In summary, conversion of PC to ES has no effect on the biophysical properties described above. The change is more

substantial from PC/ES to EX/WB conversion, where an increase in rigidity, decrease in flexibility and increase in size are observed. Our results also show that WB is slightly less rigid than EX.

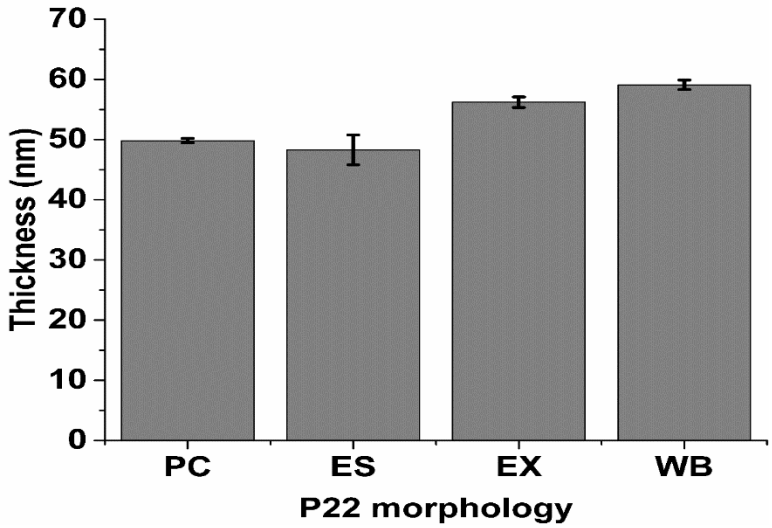


Figure 3.6. Layer thickness value obtained from Voigt model is represented and compared across all morphology of P22.

These observations follow the biology that P22 maturation undergoes major structural reorganization at icosahedral and quasi three fold axis. In addition, hexamers undergo change from skewed to symmetric after expansion (11, 47). These arrangements result in biophysical changes after maturation. Increase in rigidity after expansion has been observed for the HK 97 virus (17) that undergoes structural transformations similar to P22 except cross linking in HK97 capsid after expansion. We can't directly compare these two techniques but we can certainly compare the trend in the capsid stiffness. AFM measurements depend on large scale deformations, while QCM-D measures the small scale

protein perturbations and proteins are expected to conserve shape and structure (51). Moreover, AFM is directional in nature, whereas QCM-D is independent upon particle orientation and therefore measures global property. By comparing the maturation trend of HK 97 and P22, we can hypothesize that increase in rigidity is an inevitable transformation necessary for the expansion leads to maturation.

Conclusion

Till date, AFM is the major technique that has been implemented to understand rigidity in viruses. This is to our knowledge the first attempt to model QCM-D data to extract biophysical parameters of any virus. Despite the limitation of the model, we achieve the good fit and all the model outputs connect to the maturation of P22. Our study will encourage scientists to implement this technique to other unexplored macromolecular systems. P22 is also currently been used a nano-container for different applications ranging from bioinspired materials to nanomedicine (49, 52–55). Therefore investigation about layer properties, rigidity and viscosity could be a key for the development of a nanomaterial assembly and transformations.

References

1. Hendrix RW. 1999. Evolution: The long evolutionary reach of viruses. Curr Biol 9:914–917.

2. Veesler D, Johnson JE. 2012. Virus maturation. Annu Rev Biophys 41:473–96.

3. Zlotnick A. 2005. Theoretical aspects of virus capsid assembly. J Mol Recognit 18:479–490.

4. Tuma R, Tsuruta H, French KH, Prevelige PE. 2008. Detection of intermediates and kinetic control during assembly of bacteriophage P22 procapsid. J Mol Biol 381:1395–406.

5. Bothner B, Taylor D, Jun B, Lee KK, Siuzdak G, Schultz CP, Schlutz CP, Johnson JE. 2005. Maturation of a tetravirus capsid alters the dynamic properties and creates a metastable complex. Virology 334:17–27.

6. Galisteo ML, King J. 1993. Conformational transformations in the protein lattice of phage P22 procapsids. Biophys J 65:227–35.

7. Wikoff WR, Liljas L, Duda RL, Tsuruta H, Hendrix RW, Johnson JE. 2000. Topologically linked protein rings in the bacteriophage HK97 capsid. Science 289:2129–2133.

8. Duda RL. 1998. Protein chainmail: Catenated protein in viral capsids. Cell 94:55–60.

9. Gertsman I, Gan L, Guttman M, Lee K, Speir JA, Duda RL, Hendrix RW, Komives EA, Johnson JE. 2009. An unexpected twist in viral capsid maturation. Nature 458:646–650.

10. Galisteo ML, King J. 1993. Conformational transformations in the protein lattice of phage P22 procapsids. Biophys J 65:227–35.

11. Parent KN, Khayat R, Tu LH, Suhanovsky MM, Cortines JR, Teschke CM, Johnson JE, Baker TS. 2010. P22 coat protein structures reveal a novel mechanism for capsid maturation: stability without auxiliary proteins or chemical crosslinks. Structure 18:390–401.

12. Tuma R, Prevelige PE, Thomas GJ. 1998. Mechanism of capsid maturation in a double-stranded DNA virus. Proc Natl Acad Sci U S A 95:9885–9890.

13. Zlotnick A. 2003. Are weak protein-protein interactions the general rule in capsid assembly? Virology 315:269–274.

14. Uchida M, Douglas T. 2013. Unravelling capsid transformations. Nat Chem 5:444–445.

15. Roos WH, Ivanovska IL, Evilevitch a., Wuite GJL. 2007. Viral capsids: Mechanical characteristics, genome packaging and delivery mechanisms. Cell Mol Life Sci 64:1484–1497.

16. Kuznetsov YG, McPherson A. 2011. Atomic force microscopy in imaging of viruses and virus-infected cells. Microbiol Mol Biol Rev 75:268–285.

17. Roos WH, Gertsman I, May ER, Brooks CL, Johnson JE, Wuite GJL. 2012. Mechanics of bacteriophage maturation. Proc Natl Acad Sci 109:2342–2347.

18. Kuznetsov YG, Gurnon JR, Van Etten JL, McPherson A. 2005. Atomic force microscopy investigation of a chlorella virus, PBCV-1. J Struct Biol 149:256–263.

19. Kuznetsov YG, McPherson A. 2011. Atomic Force Microscopy in Imaging of Viruses and Virus-Infected Cells. Microbiol Mol Biol Rev 75:268–285.

20. Michel JP, Ivanovska IL, Gibbons MM, Klug WS, Knobler CM, Wuite GJL, Schmidt CF. 2006. Nanoindentation studies of full and empty viral capsids and the effects of capsid protein mutations on elasticity and strength. Proc Natl Acad Sci U S A 103:6184–6189.

21. Earnshaw W, Casjens S, Harrison SC. 1976. Assembly of the head of bacteriophage P22: X-ray diffraction from heads, proheads and related structures. J Mol Biol 104:387–410.

22. Casjens S, Adams MB, Hall C, King J. 1985. Autogenous Modulation of Bacteriophage 123:174–179.

23. Parker MH, Casjens S, Prevelige PE. 1998. Functional domains of bacteriophage P22 scaffolding protein. J Mol Biol 281:69–79.

24. Parker MH, Prevelige PE. 1998. Electrostatic interactions drive scaffolding/coat protein binding and procapsid maturation in bacteriophage P22. Virology 250:337–49.

25. Prevelige PE, Thomas D, King J. 1988. Scaffolding protein regulates the polymerization of P22 coat subunits into icosahedral shells in vitro. J Mol Biol 202:743–57.

26. Teschke CM, McGough A, Thuman-Commike P a. 2003. Penton release from P22 heat-expanded capsids suggests importance of stabilizing penton-hexon interactions during capsid maturation. Biophys J 84:2585–92.

27. Lucon J, Qazi S, Uchida M, Bedwell GJ, Lafrance B, Jr PEP, Douglas T. 2012. polymerization with high-density cargo loading. Nat. Chem 4:781–788.

28. Dixon MC. 2008. Quartz crystal microbalance with dissipation monitoring: enabling real-time characterization of biological materials and their interactions. J Biomol Tech 19:151–8.

29. Rodahl M, Höök F, Krozer A, Brzezinski P, Kasemo B. 1995. Quartz crystal microbalance setup for frequency and Q-factor measurements in gaseous and liquid environments. Rev Sci Instrum 66:3924–3930.

30. Arnau A. 2008. A Review of Interface Electronic Systems for AT-cut Quartz Crystal Microbalance Applications in Liquids. Sensors 8:370–411.

31. Rodahl M, Kasemo B. 1996. A simple setup to simultaneously measure the resonant frequency and the absolute dissipation factor of a quartz crystal microbalance. Rev Sci Instrum 67:3238–3241.

32. Bradshaw BL. 2000. Understanding piezoelectric quartz crystals, www.rfdesign.com, August.

33. Dutta AK, Belfort G. 2007. Adsorbed gels versus brushes: viscoelastic differences. Langmuir 23:3088–94.

34. Voinova M V, Rodahl M, Jonson M, Kasemo B. Viscoelastic Acoustic Response of Layered Polymer Films at Fluid-Solid Interfaces : Viscoelastic Acoustic Response of Layered Polymer Films at Fluid-Solid Interfaces : Continuum Mechanics Approach. Applied Physics report, 97-34.

35. Wang S-H, Shen C-Y, Weng T-C, Lin P-H, Yang J-J, Chen I-F, Kuo S-M, Chang S-J, Tu Y-K, Kao Y-H, Hung C-H. 2010. Detection of cartilage oligomeric matrix protein using a quartz crystal microbalance. Sensors (Basel) 10:11633–43.

36. Rayaprolu V, Manning BM, Douglas T, Bothner B. 2010. Virus particles as active nanomaterials that can rapidly change their viscoelastic properties in response to dilute solutions. Soft Matter 6:5286.

37. Liu H, Qu C, Johnson JE, Case D a. 2003. Pseudo-atomic models of swollen CCMV from cryo-electron microscopy data. J Struct Biol 142:356–363.

38. Voinova M V, Rodahl M, Jonson M, Kasemo B. 1999. Viscoelastic acoustic response of layered polymer films at fluid-solid interfaces: continuum mechanics approach. Phys Scr 59:391–396.

39. Bandey HL, Robert Hillman a., Brown MJ, Martin SJ. 1997. Viscoelastic characterization of electroactive polymer films at the electrode/solution interface.

Faraday Discuss 107:105–121.

40. Johannsmann D. 1999. Viscoelastic analysis of organic thin films on quartz resonators. Macromol Chem Phys 516:501–516.

41. Larsson C, Rodahl M, Höök F. 2003. Characterization of DNA immobilization and subsequent hybridization on a 2D arrangement of streptavidin on a biotin-modified lipid bilayer supported on SiO2. Anal Chem 75:5080–5087.

42. Höök F, Kasemo B, Nylander T, Fant C, Sott K, Elwing H. 2001. Variations in coupled water, viscoelastic properties, and film thickness of a Mefp-1 protein film during adsorption and cross-linking: a quartz crystal microbalance with dissipation monitoring, ellipsometry, and surface plasmon resonance study. Anal Chem 73:5796–804.

43. Zandi R, Reguera D. 2005. Mechanical properties of viral capsids. Phys Rev E - Stat Nonlinear, Soft Matter Phys 72.

44. Liu SX, Kim J-T. 2009. Application of Kevin–Voigt Model in Quantifying Whey Protein Adsorption on Polyethersulfone Using QCM-D. J Assoc Lab Autom 14:213–220.

45. Malmström J, Agheli H, Kingshott P, Sutherland DS. 2007. Viscoelastic modeling of highly hydrated laminin layers at homogeneous and nanostructured surfaces: Quantification of protein layer properties using QCM-D and SPR. Langmuir 23:9760–9768.

46. Binazadeh M, Zeng H, Unsworth LD. 2013. Effect of peptide secondary structure on adsorption and adsorbed film properties. Acta Biomater 9:6403–13.

47. Chen D-H, Baker ML, Hryc CF, DiMaio F, Jakana J, Wu W, Dougherty M, Haase-Pettingell C, Schmid MF, Jiang W, Baker D, King J a, Chiu W. 2011. Structural basis for scaffolding-mediated assembly and maturation of a dsDNA virus. Proc Natl Acad Sci U S A 108:1355–1360.

48. O'Neil A, Reichhardt C, Johnson B, Prevelige PE, Douglas T. 2011. Genetically programmed in vivo packaging of protein cargo and its controlled release from bacteriophage P22. Angew Chemie - Int Ed 50:7425–7428.

49. Patterson D, Edwards E, Douglas T. 2015. Hybrid Nanoreactors: Coupling Enzymes and Small-Molecule Catalysts within Virus-Like Particles. Isr J Chem 55:96–101.

50. Kang S, Uchida M, O'Neil A, Li R, Prevelige PE, Douglas T. 2010. Implementation of p22 viral capsids as nanoplatforms. Biomacromolecules 11:2804–9.

51. Lubarsky G V., Davidson MR, Bradley RH. 2007. Hydration-dehydration of

adsorbed protein films studied by AFM and QCM-D. Biosens Bioelectron 22:1275–1281.

52. Usselman RJ, Qazi S, Aggarwal P, Eaton SS, Eaton GR, Russek S, Douglas T. 2015. Gadolinium-Loaded Viral Capsids as Magnetic Resonance Imaging Contrast Agents. Appl Magn Reson 46:349–355.

53. Bedwell GJ, Zhou Z, Uchida M, Douglas T, Gupta A, Prevelige PE. 2015. Selective Biotemplated Synthesis of TiO2 inside a Protein Cage. Biomacromolecules 16:214–218.

54. Patterson DP, Schwarz B, Waters RS, Gedeon T, Douglas T. 2014. Encapsulation of an enzyme cascade within the bacteriophage P22 virus-like particle. ACS Chem Biol 9:359–365.

55. Kale A, Bao Y, Zhou Z, Prevelige PE, Gupta A. 2013. Directed self-assembly of CdS quantum dots on bacteriophage P22 coat protein templates. Nanotechnology 24:045603.

CHAPTER 4

PROLONGED INCUBATION WITH LIPOSOME LEADS TO PLA2 ACTIVATION IN ADENO-ASSOCIATED VIRUSES

Contribution of Authors and Co-Authors

Manuscript in Chapter 4

Author: Ravi Kant

Contributions: Optimized and established purification and data collection, collected and analyzed data, prepared the manuscript

Co-Author: Navid Movahed

Contributions: Assisted in establishing protocols

Co-Author: Dewey Brooke

Contributions: Assisted in establishing protocols

Co-Author: Antonette Bennett

Contributions: AAVs sample preparation

Co-Author: Mavis Agbandje-McKenna

Contributions: Helped in manuscript editing and critical discussion

Co-Author: Brian Bothner

Contributions: Obtained funding, provided critical intellectual input and mentoring, discussed data and the manuscript

Manuscript Information Page

PROLONGED INCUBATION WITH LIPOSOMES LEADS TO PLA2 ACTIVATION IN ADENO-ASSOCIATED VIRUSES

Authors: Ravi Kant, Navid Movahed, Dewey Brooke, Antonette Bennett, Mavis Agbandje-McKenna, Brian Bothner

Status of Manuscript:
__x_ Prepared for submission to a peer-reviewed journal
____ Officially submitted to a peer-review journal
____ Accepted by a peer-reviewed journal
____ Published in a peer-reviewed journal

Publisher:

Issue in which Manuscript Appears: In Preparation

CHAPTER 4

PROLONGED INCUBATION WITH LIPOSOMES LEADS TO PLA2 ACTIVATION IN ADENO-ASSOCIATED VIRUSES

Abstract

Non-enveloped animal viruses face a major challenge in how to circumvent the plasma membrane. A common theme involves conformational change of the capsid in response to host factors. Adeno-associated viruses (AAVs) are small, non-pathogenic viruses showing great promise in human gene therapy. Escape of AAVs from endosomes involves activation of a capsid bound lipase domain. Currently the mechanism responsible for lipase activation is unclear. To investigate lipase activation we developed a highly sensitive mass spectrometry based assay. Using this approach, we show that prolonged incubation of AAV particles with liposomes stimulates the capsid tethered enzyme. *In vitro*, activation does not require involvement of cellular receptors or a drop in pH.

Introduction

AAVs are small, non-enveloped, icosahedral viruses with a single stranded DNA genome. They are members of the parvoviridae (genus-Dependovirus), have a T1 architecture, and are assembled from three capsid proteins VP1, VP2 and VP3 at a ratio of 1:1:8/10 (1, 2). The proteins VP1 and VP2 share the same C-terminal amino acids with VP3, but have an additional domains at the N-terminus. VP1 is 137 residues larger than VP2, and VP2 is 65 residues larger than VP3 (3) (4). Despite being non-pathogenic, AAVs

have received considerable attention due to their promise as vectors in gene therapy (5–10).

AAVs enter a cell via receptor mediated endocytosis (11–13). According to the current model of AAV infection cycle, AAV enters into host cells within the first 60 minutes of exposure (14). Almost 2/3 of the particles that initially bind to the plasma membrane are taken up by 10 minutes (15). After internalization, subsequent trafficking and escape of AAV from endosomes is not well understood and is believed to vary from cell type to cell type (16, 17). Among the common AAV serotypes, AAV2 is the best characterized with regard to cell entry and trafficking. Once AAV2 attaches to its primary receptor (heparin sulphate), entry is facilitated through dynamin dependent clathrin mediated endocytosis (18). Acidification of endosomes is important and has been proposed to trigger externalization of the N-terminus of VP1 without disrupting the integrity of capsid (3). The VP1 N-terminal domain contains a phospholipase (PLA2) and a nuclear localization signal (NLS). Deletion of either causes a multi-log reduction in titer (19). Current models of entry suggest that phospholipid cleavage results in the breakdown of endosomes, escape of virus particles into the cytoplasm and subsequent trafficking to the nucleus (19–21).

Characterization of the lipase domain has largely been conducted *in-vitro*. Lipase activity is minimal in freshly purified particles. Standard protocols for AAVs use heat to activate the lipase (22). The evidence for externalization as the trigger behind activity is based on seroconversion after heating when using antibodies specific to the PLA2 (3, 23–25). A cryo-EM study of AAV2 capsids revealed that protein density inside the capsids at

2-fold axes was lost upon heating at 65 ^{o}C for 3 minutes. This density was interpreted to be the N-terminal part of VP1 (26). *In-vivo* externalization is believed to be triggered by receptor binding and a drop in pH (19). However, *in-vitro* studies on AAVs have largely failed to identify the specific triggers and pH alone is insufficient for lipase activation or externalization as judged by antibody binding (19, 25)

Each AAV particles contains on average five copies of VP1, five copies of VP2 and fifty copies of VP3 proteins and therefore 5 enzymes (1, 27–30). Characterization of heterologously expressed AAV2 PLA2 indicates that it has low activity compared to other soluble forms of the enzyme (3, 22). The most commonly used methods for measuring lipase activity include radioactive, colorimetric, and fluorescence based assays. When applied to AAVs, these techniques can be problematic due to low sensitivity, use of modified substrate, and accumulation of radioactive waste (31–37). A method based on Liquid Chromatography Mass Spectrometry (LC-MS) for quantification of released fatty acids has been described (38). Due to the low level of activity associated with AAV PLA2s and a desire to screen a large number of samples, we sought to develop an improved method that was sensitive, fast enough to collect data on enzyme kinetics and did not require modified lipid substrates. The LC-MS method that we arrived at uses HILIC-style (normal phase) chromatography in a conventional solvents system (0.1% formic acid in water and acetonitrile). This allowed us to measure and quantitate the cleavage products consistently and accurately.

Materials and Methods

AAV Purification

Virus-like Particle Production and Purification: Recombinant baculovirus encoding VP1, VP2, and VP3 of AAV2 was generated using the Bac-to-Bac expression system (Invitrogen, cat#10359-016). The virus-like particles (VLPs) of each virus was expressed in sf9 cells and purified according to previously established protocols (39–42). AAV2 was purified using a step iodixanol gradient followed by anion exchange chromatography (43, 44). The pellets were resuspended in lysis buffer (50mM Tris-HCl, pH8.0, 100mM NaCl, 1mM EDTA, and 0.2% Triton X-100) and freeze/thawed three times in a dry ice-ethanol slurry and 37°C water bath with the addition of 1 µL of Benzonase (Sigma, cat#E1014;50 U/ml final concentration) and incubated at 37°C for 30min after the second freeze/thaw cycle. The crude cell lysate was clarified by centrifugation at 12,100 x g at 4°C for 15 min. For AAV2, the clarified supernatant was loaded onto a discontinuous 15-60% iodixanol (Optiprep) step gradient (Nycomed, cat#1114542), and centrifuged at 350,000 x g at 18°C for 1h and the gradient fractionated. The 25% iodixanol gradient fraction, enriched with AAV2 VLPs, was further purified on a 5ml HiTrap Q anion exchange column (GE Healthcare, cat#17-5159-01) The sample was diluted with Buffer A (20Mm Tris-HCl, 15mM NaCl, pH8.5), loaded onto the column, washed with 50ml of Buffer A, eluted with a gradient of 30ml of Buffer A and Buffer B (20Mm Tris, 15mM NaCl, pH8.5), and the peak fractions collected. The purity and integrity of the VLPs were monitored using Coomassie stained SDS-PAGE and negative-stain electron microscopy (EM) on a JEOL JEM-100CX III microscope.

Liposome Preparation

Liposomes were prepared by transferring 0.05ml of 25mg/µl dissolved 1-palmitoyl-2-oleoyl-*sn*-glycero-3-phosphocholine (POPC) in chloroform (1.64umole) in a glass tube. Chloroform was then dried by gentle passing nitrogen gas in the test tube. To the dried POPC, 1.640ml of HBS (100mM NaCl, 20mM Hepes/NaOH, pH7.5) was added and incubated for 2h at room temperature. After incubation, lipid was re-suspended by vigorous mixing which resulted in a milky appearance of the resuspension indicated the presence of multilamellar vesicles. To form unilamellar vesicles, the multilamellar vesicles were broken down by sonication which was continued until the solution became transparent. Overheating of the vesicles was avoided by interrupting sonication, total time was 45 minutes. Unilamellar vesicles were stored at 4^{o}C. This protocol was optimized from that previously published by the Morrissey lab (45).

Liquid Chromatography-Mass Spectrometry

Lipase activity was measured with an Agilent 1290 ultrahigh pressure (UPLC) series chromatography instrument coupled to a Bruker MicroTOF mass spectrometer. The activity was measured in positive mode. Control lipase reactions were initiated by mixing 0.002ml of Bee venom lipase A_2 (0.1mg/ml) (Sigma: Product number P9279) and 0.005ml of unilamellar liposomes in the presence of 5mM $CaCl_2$. Total reaction volume was set as 0.04ml using 20mM universal buffer (20mM HEPES 4-(2-hydroxyethyl)-1-piperazineethanesulfonic acid, 20mM MES 2-(N-Morpholino) ethanesulfonic acid, 20mM NaOAc (sodium acetate) and 50mM NaCl (sodium chloride) (46), pH 7.5 and reaction was incubated at 37°C. Substrate and reaction products were separated on a Kinetex™ HILIC-

LC Column (2.6 µm, 100 Å, 30 x 2.1 mm) (Phenomenex) using a multi-linear gradient (solvent A: 0.1% formic acid in water, solvent B: 0.1% formic acid in acetonitrile) at 0.5ml/min flow rate. The gradient conditions were set as follows: 0 min, 2%B; 0.7-3.0min, 17-70%B; 3-3.2, 70-98%B, 3.2-4min, 2% at column temperature 40°C. Electrospray conditions were: drying gas flow 8.0L/min, dry temperature 180°C, and capillary exit 150V. Scan range was 200-3000 m/z. Data processing and analysis were performed using a Bruker Data Analysis package 4.0. Mass/charge ratio of substrate POPC was verified as 760.56m/z. Lipase activity was verified by confirming two different cleavage products 496.32 (PLA2 specificity) and 522.34 (PLA1 specificity). For AAV2 and AAV9 reactions, 0.003ml of purified particles at 0.2m g/ml was used for each lipase assay.

Results and Discussion

Development of LC-MS Method

Liposomes were formed using POPC, a major component of human plasma membranes (47, 48). Bee venom phospholipase A2 (bvPLA2) served as a positive control. The reaction was initiated by mixing the bvPLA2, liposomes, and $CaCl_2$. The reaction was then placed in the HPLC autosampler at 37^0C. Aliquots of the reaction were analyzed at selected time points automatically using rapid HILIC chromatography and positive mode ESI. This method is unconventional in that the phospholipids lipids and their products were separated on a HILIC (normal phase) column using an increasing gradient of acidified organic solvent. We were able to detect the substrate (POPC) as well as enzymatic products

(lysoPC) generated by bvPLA2 (Figure 4.1). Chromatography gradient lasted 4 minutes and provided excellent separation of molecular species.

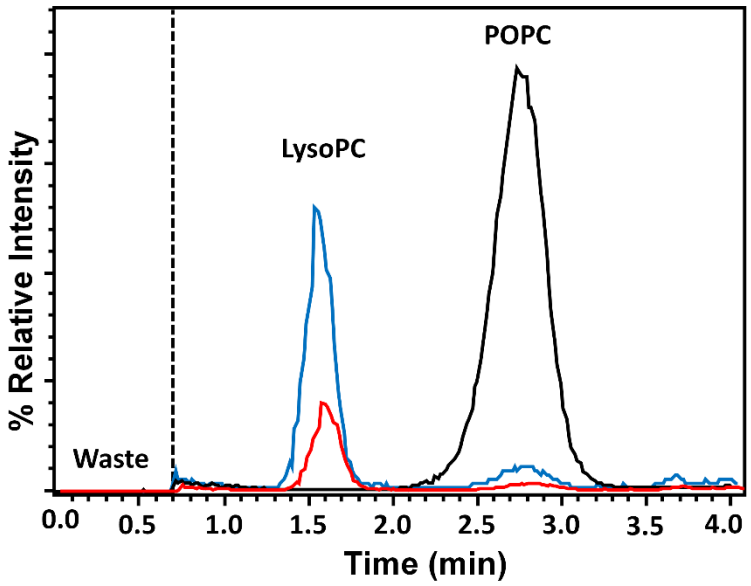


Figure 4.1. LC-MS analysis of POPC and the lysoPC product generated by bvPLA2. Dotted line indicates the time until which solvent was directed to waste. Extracted ion chromatograms (EIC) show POPC (black) and after 5min of reaction (blue). The two different lysoPC products are shown in different colors: PLA2 (blue) and PLA1 (red).

POPC substrate was observed as 760.56 m/z (expected 760.57) (Figure 4.2). We observed two different lysoPC products from the reaction mixtures: PLA2 product (palmitoyl-2-hydroxy-*sn*-glycero-3-phosphocholine) resulting from hydrolysis at the C-2 position (major product) was observed as 496.32 m/z (MH^+ expected 496.33 m/z). A minor product from a PLA1 type hydrolysis (1-hydroxy-2-oleoyl-*sn*-glycero-3-phosphocholine) was observed at 522.34 m/z (MH^+ expected 522.34 m/z). In addition, to the protonated species, the singly charged sodium adduct ion species was observed.

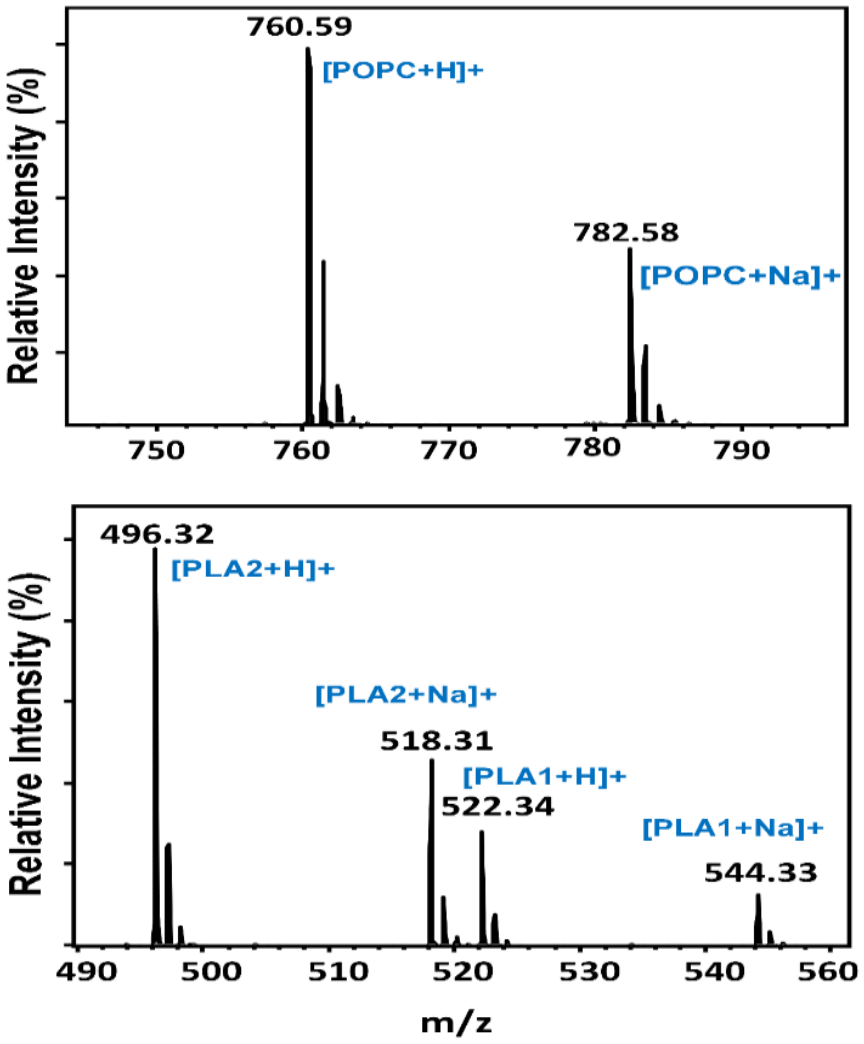


Figure 4.2. Mass spectra of the substrate and product generated by bvPLA2. LC-MS spectrum of intact POPC (upper panel). LC-MS spectrum of lysoPC products from PLA2 and PLA1 specific reactions (lower panel).

Measuring AAV Lipase Activity by LC-MS Method

Having tested the LC-MS method, we were ready to measure AAV lipase activity. Heating of AAV2 at 65^0C for 3 minutes has been reported to externalize and activate the lipase domain (3, 22, 49). The AAV2 capsid maintains structural integrity during and after

thermal treatment (50). After heating, capsids were cooled to room temperature. As a control, capsids were incubated at 37^0C for 3 minutes. Both heated and non-heated AAV2, were separately mixed with liposomes and $CaCl_2$ as described in the method section. Reaction mixtures were separated and analyzed by LC-MS. Activity was quantified by integrating the area under the EIC of lysoPC products. Product accumulations were plotted against incubation time. A steady accumulation of product was measured for 3 hours (Figure 4.3). This confirmed heat treated AAV2 contained an active lipase. Our LC-MS results corroborates the previous reports that heat act as a surrogate to expose the buried PLA2 domain in AAV2 (3, 22, 49).

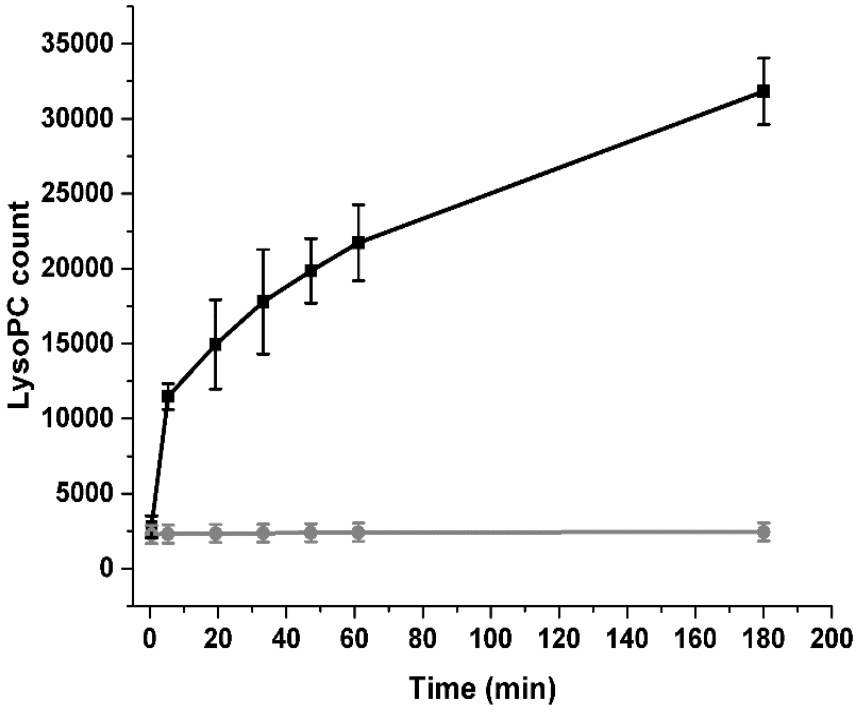


Figure 4.3. Production of lysoPC by AAV2 over time. Lipase reaction product formation by heat activated (black) and control (grey) AAV2.

Activation of AAV2
Lipase Domain without Heat

Up to this point, we have shown that we can monitor the activation of the PLA2 domain by heat. This is clearly not relevant to *in vivo* activation, so we tested factors that could be important during endocytosis. Our initial experiments involved lowering the pH without heat, as occurs during endocytosis. Incubation of AAV2 at pH 5 for 60 minutes failed activate the lipase. Temporal analysis of intracellular trafficking and un-coating of recombinant AAVs have reported that expression of reporter genes can require 8 to 24 hours (51–53). In addition, studies using green fluorescent protein tagged (GFP) AAV particles, have shown that 11 hours after contacting cells, the particles displayed perinuclear accumulation, with 90% of the GFP signal remained outside the nucleus (54). These studies prompted us to consider if prolonged exposure to membranes in the endosome could be an important factor for understanding the infection cycle. To test this, we extended the incubation of AAV2 with liposomes at 37^0C (5mM $CaCl_2$) to 12 and 24 hours. Figure 4.4 shows the product abundance as determined by LC-MS of AAV2 control, heated (65ºC), and with prolonged incubation with liposomes. The observed the lysoPC product after 12 and 24 hour incubations exceeded what was expected based on the 30 minute and 1 hour control time points by 3.6 and 5.9 fold respectively. To confirm that the products were not generated by auto hydrolysis of liposomes under our experimental conditions, we ran an additional experiment. Liposomes were incubated in the presence of calcium for 12 and 24hr without AAV2 (negative control). We did not observe lysoPC products in this reaction. We have reported the lipase activity of AAV2 at pH 7.5. This pH

was selected because it has been reported to be the optimal pH for AAV2 lipase catalytic activity (22).

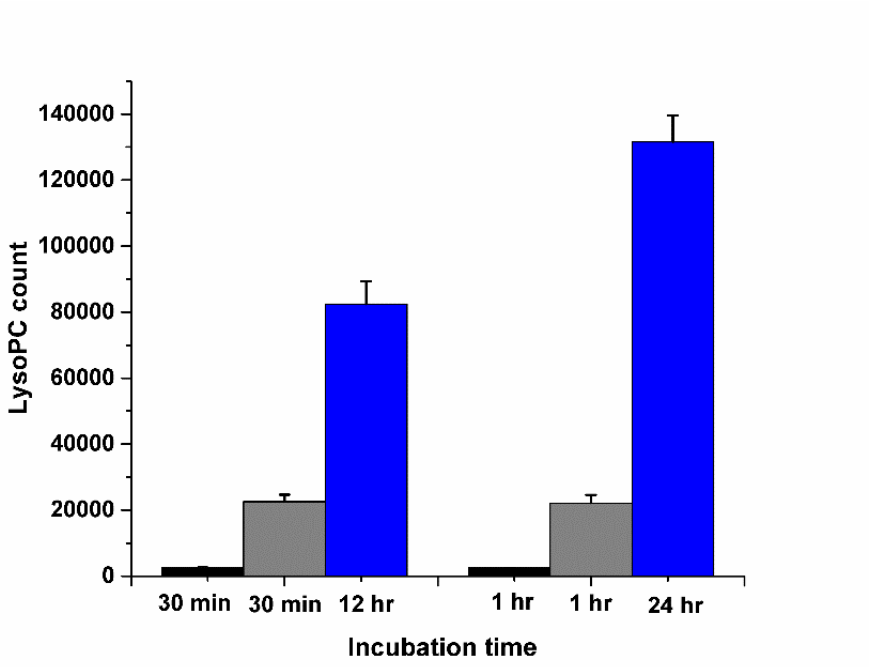


Figure 4.4. Lipase activity of AAV2 after prolonged incubation with liposomes. Integrated area under EIC of lyso-PC is shown for each sample. All reactions were conducted at 37ºC. Control (black), heated (grey), prolonged incubation (blue). Significant lipase activation occurred with time.

Product Specificity Is Independent of the Mode of Lipase Activation

After confirming the lipase activity of AAV2 without heat, we were interested in the impact of heating may have on the enzyme. To investigate this, we compared the % product specificity of heat activated and prolonged incubation activated AAV2. AAV2 enzyme has been categorized as a PLA2 class lipase. This is based on phylogenetic analyses (55) and

the observed ability to hydrolyze fatty acids at the C-2 position (22). However, by using a phospholipid with different fatty acids chains at positions C1 and C2, we have clearly demonstrated that hydrolysis occurs at both positions. Relative product formation was determined from the LC-MS data. We measured the ion intensity based on EIC area for PLA2 and PLA1 products (Figure S2). This was used to calculate the enzyme specificity (Figure 4.5). No significant change is specificity was observed. This indicates that catalytic specificity is independent of the mode of activation. This result is important as most of the work on AAV lipases has used heated treated samples.

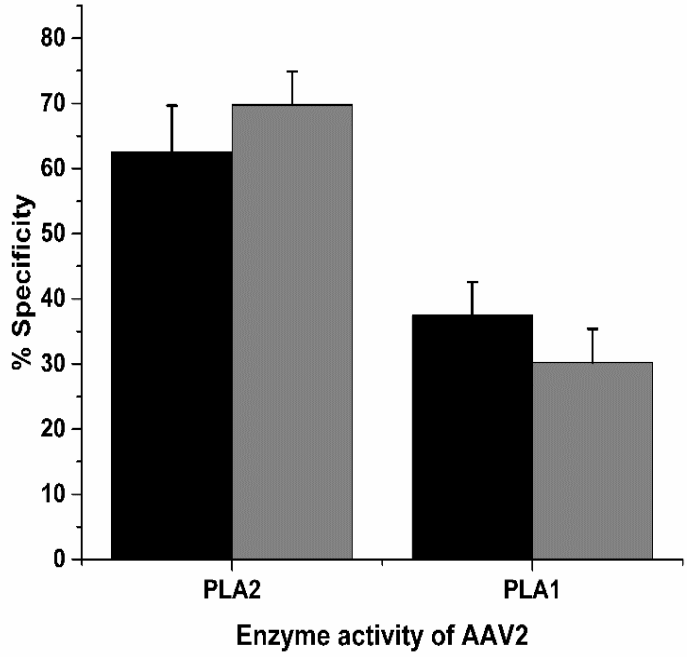


Figure 4.5. Comparison of enzyme specificity of heat activated and non-heated activated (prolonged incubation) AAV2 lipase. Both the specific (PLA2) and non-specific (PLA1) products are observed.

AAV9 Exhibits Lipase Activity after Prolonged Incubation

Different serotypes of AAVs display distinct patterns of tissue tropism (56–58). This has led to speculation that there may be different triggers for lipase activation. Therefore, we extended this study to AAV9. This is a very unique human AAV serotype which can cross the blood-brain barrier and target the central nervous system (64). This has also reported to target cardiac and skeletal muscle, as well as the liver and pancreas (59–63). We measured the lipase activity of non-heated, heated (73^0C for 3min) and prolonged incubated AAV 9 samples as was done with AAV2 above. Mixed lipase products were observed following heat activation and prolonged incubated (Figure S2, S4). Furthermore, as with AAV2, lipase product specificity was independent of the mode of activation (Figure S3). This experiment confirmed that both AAV2 and AAV9 lipases can hydrolyze lipids as a PLA1 and PLA2 enzyme. In addition, this extends our observation that incubation with membranes is a sufficient trigger to activate lipase activity.

Conclusion

The standard method for studying the role of capsid tethered AAV activity has been to uses heat to induce activation by causing VP1 domain externalization (3, 22). In this study we have shown AAV lipase activity in the absence of heat activation. The mechanism of lipase activation in AAVs has been much debated. Current models involve a series of events involving interactions between receptors, co-receptors and the acidic environment in the endosome (3, 3, 54). Our data show that prolonged interaction with a phospholipid membrane is itself sufficient to activate AAV2 and AAV9 PLA2 domain. Our results may

provide some insight into previously observations such as the delayed initiation of AAV enter and gene expression that has been observed with certain serotypes in particular cells (51–53). An obvious factor that may play a role in activation is pH. The effect of pH on the incubation time needed for activation must now be investigated. The fact that interfacial contact of particles with membranes leads to lipase activation, is consistent with observations that the N-terminal domain of VP1 maybe transiently exposed on the surface of the particle (50). This raises the question of why antibodies to AAV2 VP1 domain fail to recognize freshly purified particles. A plausible explanation is that the transient externalization of the VP1 N-terminus containing the PLA2 domain keeps the domain close to the capsid surface, inaccessible to an antibody yet within reach of a membrane surface. Once in contact with phospholipids, favorable interactions between the PLA2 domain could induce a more complete externalization. Our optimized method has a potential to be very useful tool for the characterization of different AAVs for the vector development and improvement in the gene therapy. This established assay has a potential to compatible with various substrates and pHs, therefore it can be applicable to wide range of biological systems involving lipase enzymes.

References

1. Buller RM, Rose JA. 1978. Characterization of adenovirus-associated virus-induced polypeptides in KB cells. J Virol 25:331–8.

2. Rose J a, Maizel J V, Inman JK, Shatkin a J. 1971. Structural proteins of adenovirus-associated viruses. J Virol 8:766–770.

3. Sonntag F, Bleker S, Leuchs B, Fischer R, Kleinschmidt JA. 2006. Adeno-associated virus type 2 capsids with externalized VP1/VP2 trafficking domains are generated prior to passage through the cytoplasm and are maintained until uncoating occurs in the nucleus. J Virol 80:11040–54.

4. Hoque M, Ishizu K, Matsumoto A, Han SI, Arisaka F, Takayama M, Suzuki K, Kato K, Kanda T, Watanabe H, Handa H. 1999. Nuclear transport of the major capsid protein is essential for adeno-associated virus capsid formation. J Virol 73:7912–5.

5. Coura R dos S, Nardi NB. 2008. A role for adeno-associated viral vectors in gene therapy. Genet Mol Biol 31:1–11.

6. Pugh EN, Ph D, Mingozzi F, Bennicelli J, Banfi S, Marshall KA, Testa F, Arruda VR, Konkle B, Stone E, Sun J, Jacobs J, Osso LD, Hertle R, Ma J, Redmond TM, Zhu X, Hauck B, Zelenaia O, Volpe NJ, Mcdonnell JW, Auricchio A, High KA, Bennett J. 2008. Safety and Efficacy of Gene Transfer for Leber's Congenital Amaurosis.

7. Daya S, Berns KI. 2008. Gene therapy using adeno-associated virus vectors. Clin Microbiol Rev 21:583–93.

8. Samulski RJ, Muzyczka N. 2014. AAV-Mediated Gene Therapy for Research and Therapeutic Purposes. Annu Rev Virol 1:427–451.

9. Daya S, Berns KI. 2008. Gene therapy using adeno-associated virus vectors. Clin Microbiol Rev 21:583–593.

10. Li C, Bowles DE, van Dyke T, Samulski RJ. 2005. Adeno-associated virus vectors: potential applications for cancer gene therapy. Cancer Gene Ther 12:913–25.

11. Summerford C, Samulski RJ. 1998. Membrane-associated heparan sulfate proteoglycan is a receptor for adeno-associated virus type 2 virions. J Virol 72:1438–1445.

12. Kaludov N, Brown KE, Walters RW, Chiorini JA, Kaludov N, Brown KE, Walters RW, Zabner J. 2001. and AAV5 Both Require Sialic Acid Binding for Hemagglutination and Efficient Transduction but Differ in Sialic Acid Linkage

Specificity Adeno-Associated Virus Serotype 4 (AAV4) and AAV5 Both Require Sialic Acid Binding for Hemagglutination and Efficient 4:6884–6893.

13. Walters RW, Yi SM, Keshavjee S, Brown KE, Welsh MJ, Chiorini J a, Zabner J. 2001. Binding of adeno-associated virus type 5 to 2,3-linked sialic acid is required for gene transfer. J Biol Chem 276:20610–6.

14. Seisenberger G, Ried MU, Endreß T, Büning H, Hallek M, Bräuchle Ch. 2001. Real-Time Single-Molecule Imaging of the Infection Pathway of an Adeno-Associated Virus. Science (80-) 294:1929–1933.

15. Bartlett JS, Wilcher R, Samulski RJ. 2000. Infectious entry pathway of adeno-associated virus and adeno-associated virus vectors. J Virol 74:2777–2785.

16. Hansen J, Qing K, Srivastava A. 2001. Adeno-associated virus type 2-mediated gene transfer: altered endocytic processing enhances transduction efficiency in murine fibroblasts. J Virol 75:4080–90.

17. Duan D, Yue Y, Yan Z, Yang J, Engelhardt JF. 2000. Endosomal processing limits gene transfer to polarized airway epithelia by adeno-associated virus. J Clin Invest 105:1573–1587.

18. Seisenberger G, Ried MU, Endress T, Büning H, Hallek M, Bräuchle C. 2001. Real-time single-molecule imaging of the infection pathway of an adeno-associated virus. Science 294:1929–1932.

19. Sonntag F, Bleker S, Leuchs B, Fischer R, Kleinschmidt J a. 2006. Adeno-associated virus type 2 capsids with externalized VP1/VP2 trafficking domains are generated prior to passage through the cytoplasm and are maintained until uncoating occurs in the nucleus. J Virol 80:11040–54.

20. Suikkanen S, Antila M, Jaatinen A, Vihinen-Ranta M, Vuento M. 2003. Release of canine parvovirus from endocytic vesicles. Virology 316:267–280.

21. Farr G a, Zhang L, Tattersall P. 2005. Parvoviral virions deploy a capsid-tethered lipolytic enzyme to breach the endosomal membrane during cell entry. Proc Natl Acad Sci U S A 102:17148–17153.

22. Canaan S, Z??dori Z, Ghomashchi F, Bollinger J, Sadilek M, Moreau ME, Tijssen P, Gelb MH. 2004. Interfacial Enzymology of Parvovirus Phospholipases A2. J Biol Chem 279:14502–14508.

23. Van Vliet K, Blouin V, Agbandje-McKenna M, Snyder RO. 2006. Proteolytic Mapping of the Adeno-associated Virus Capsid. Mol Ther 14:809–821.

24. Popa-Wagner R, Porwal M, Kann M, Reuss M, Weimer M, Florin L, Kleinschmidt

J a. 2012. Impact of VP1-Specific Protein Sequence Motifs on Adeno-Associated Virus Type 2 Intracellular Trafficking and Nuclear Entry. J Virol 86:9163–9174.

25. Bleker S, Pawlita M, Kleinschmidt JA. 2006. Impact of Capsid Conformation and Rep-Capsid Interactions on Adeno-Associated Virus Type 2 Genome Packaging Impact of Capsid Conformation and Rep-Capsid Interactions on Adeno-Associated Virus Type 2 Genome Packaging. J Virol 80:810–820.

26. Kronenberg S, Böttcher B, Der CW Von, Bleker S, Kleinschmidt J a, Bo B, Lieth CW Von Der. 2005. A Conformational Change in the Adeno-Associated Virus Type 2 Capsid Leads to the Exposure of Hidden VP1 N Termini A Conformational Change in the Adeno-Associated Virus Type 2 Capsid Leads to the Exposure of Hidden VP1 N Termini 79:5296–5303.

27. Carter BJ, Rose JA. 1972. Adenovirus-Associated Virus Multiplication 10:9–16.

28. Johnson FB, Ozer HL, Hoggan MD. 1971. Structural proteins of adenovirus-associated virus type 3. J Virol 8:860–63.

29. Becerra SP, Koczot F, Fabisch P, Rose J a. 1988. Synthesis of adeno-associated virus structural proteins requires both alternative mRNA splicing and alternative initiations from a single transcript. J Virol 62:2745–2754.

30. Cassinotti P, Weitzand M, Tratschin JD. 1988. Organization of the adeno-associated virus (AAV) capsid gene: Mapping of a minor spliced mRNA coding for virus capsid protein. Virology 167:176–184.

31. Panteghini M, Pagani F, Bonora R. 1993 Clinical and Analytical Evaluation of a Continuous Enzymatic Method for Measuring Pancreatic Lipase Activity. Clin Chem 39/2, 304-308

32. Jette JF, Ziomek E. 1994. Determination of lipase activity y a Rhodamine-Triglycerid-Agarose Assay. Anal Biochem 219, 256-260

33. Hendrickson HS. 1994. Fluorescence-based assays of lipases, phospholipases, and other lipolytic enzymes. Anal Biochem.

34. Negre-Salvayre A, Abouakil N, Lombardo D, Salvayre R. 1990. Hydrolysis of fluorescent pyrene-acyl esters by human pancreatic carboxylic ester hydrolase and bile salt-stimulated lipase. Lipids 25:428–434.

35. Negre-Salvayre A, Dagan A, Gatt S, Salvayre R. 1993. Use of pyrenemethyl laurate for fluorescence-based determination of lipase activity in intact living lymphoblastoid cells and for the diagnosis of acid lipase deficiency. Biochem J 294 (Pt 3:885–891.

36. Wilton DC. 1991. A continuous fluorescence-displacement assay for triacylglycerol lipase and phospholipase C that also allows the measurement of acylglycerols. Biochem J 276 (Pt 1:129–133.

37. Briquet-Laugier V, Ben-Zeev O, Doolittle MH. 1999. Determining lipoprotein lipase and hepatic lipase activity using radiolabeled substrates. Methods Mol Biol 109:81–94.

38. Hao G, Yang L, Mazsaroff I, Lin M. 2007. Quantitative Determination of Lipase Activity by Liquid Chromatography-Mass Spectrometry. J Am Soc Mass Spectrom 18:1579–1581.

39. Kim J, Jung J, Reyes JL, Kim Y, Kim S, Chung K, Kim JA, Lee M, Lee Y, Kim VN, Park C. 2006. NIH Public Access 42:84–94.

40. DiMattia M, Govindasamy L, Levy HC, Gurda-Whitaker B, Kalina A, Kohlbrenner E, Chiorini JA, McKenna R, Muzyczka N, Zolotukhin S, Agbandje-McKenna M. 2005. Production, purification, crystallization and preliminary X-ray structural studies of adeno-associated virus serotype 5. Acta Crystallogr Sect F Struct Biol Cryst Commun 61:917–921.

41. Lane MD, Nam HJ, Padron E, Gurda-Whitaker B, Kohlbrenner E, Aslanidi G, Byrne B, McKenna R, Muzyczka N, Zolotukhin S, Agbandje-McKenna M. 2005. Production, purification, crystallization and preliminary X-ray analysis of adeno-associated virus serotype 8. Acta Crystallogr Sect F Struct Biol Cryst Commun 61:558–561.

42. Kaludov N, Padron E, Govindasamy L, McKenna R, Chiorini J a, Agbandje-McKenna M. 2003. Production, purification and preliminary X-ray crystallographic studies of adeno-associated virus serotype 4. Virology 306:1–6.

43. Mah C, Fraites JTJ, Zolotukhin I, Song S, Flotte TR, Dobson J, Batich C, Byrne BJ. 2002. Improved Method of Recombinant AAV2 Delivery for Systemic Targeted Gene Therapy. Mol Ther 6:106–12.

44. Zolotukhin S, Potter M, Zolotukhin I, Sakai Y, Loiler S, Fraites TJ, Chiodo VA, Phillipsberg T, Muzyczka N, Hauswirth WW, Flotte TR, Byrne BJ, Snyder RO. 2002. Production and purification of serotype 1, 2, and 5 recombinant adeno-associated viral vectors. Methods 28:158–67.

45. Neuenschwander PF, Fiore MM, Morrisseys JH. 1993. Factor VII Autoactivation proceeds via Interaction of Distinct Protease-Cofactor and Zymogen-Cofactor Complexes. J Biol Chem 268:21489–21492.

46. Brooke D, Movahed N, Bothner B. 2015. Universal buffers for use in biochemistry and biophysical experiments. AIMS Biophys 2:336–342.

47. V??cha R, Berkowitz ML, Jungwirth P. 2009. Molecular model of a cell plasma membrane with an asymmetric multicomponent composition: Water permeation and ion effects. Biophys J 96:4493–4501.

48. Andoh Y, Okazaki S, Ueoka R. 2013. Molecular dynamics study of lipid bilayers modeling the plasma membranes of normal murine thymocytes and leukemic GRSL cells. Biochim Biophys Acta - Biomembr 1828:1259–1270.

49. Wu P, Xiao W, Conlon T, Hughes J, Agbandje-McKenna M, Ferkol T, Flotte T, Muzyczka N. 2000. Mutational analysis of the adeno-associated virus type 2 (AAV2) capsid gene and construction of AAV2 vectors with altered tropism. J Virol 74:8635–8647.

50. Rayaprolu V, Kruse S, Kant R, Venkatakrishnan B, Movahed N, Brooke D, Lins B, Bennett A, Potter T, McKenna R, Agbandje-McKenna M, Bothner B. 2013. Comparative Analysis of Adeno Associated Virus Capsid Stability and Dynamics. J Virol.

51. Douar A, Poulard K, Stockholm D, Danos O. 2001. Intracellular Trafficking of Adeno-Associated Virus Vectors : Routing to the Late Endosomal Compartment and Proteasome Degradation Intracellular Trafficking of Adeno-Associated Virus Vectors : Routing to the Late Endosomal Compartment and Proteasome Degra. Society 75:1824–1833.

52. Xiao P-J, Samulski RJ. 2012. Cytoplasmic trafficking, endosomal escape, and perinuclear accumulation of adeno-associated virus type 2 particles are facilitated by microtubule network. J Virol 86:10462–73.

53. Li C, He Y, Nicolson S, Hirsch M, Weinberg MS, Zhang P, Kafri T, Samulski RJ. 2013. Adeno-associated virus capsid antigen presentation is dependent on endosomal escape. J Clin Invest 123:1390–1401.

54. Lux K, Goerlitz N, Schlemminger S, Goldnau D, Endell J, Leike K, Kofler M, Finke S, Hallek M, Perabo L, Kofler DM. 2005. Green Fluorescent Protein-Tagged Adeno-Associated Virus Particles Allow the Study of Cytosolic and Nuclear Trafficking Green Fluorescent Protein-Tagged Adeno-Associated Virus Particles Allow the Study of Cytosolic and Nuclear Trafficking †. Society 79:11776–11787.

55. Gao G, Vandenberghe LH, Alvira MR, Lu Y, Calcedo R, Zhou X, Wilson JM. 2004. Clades of Adeno-associated viruses are widely disseminated in human tissues. J Virol 78:6381–8.

56. Zincarelli C, Soltys S, Rengo G, Rabinowitz JE. 2008. Analysis of AAV serotypes 1-9 mediated gene expression and tropism in mice after systemic injection. Mol Ther 16:1073–1080.

57. Wu Z, Asokan A, Samulski RJ. 2006. Adeno-associated Virus Serotypes: Vector Toolkit for Human Gene Therapy. Mol Ther 14:316–327.

58. Asokan A, Schaffer D V, Jude Samulski R. 2012. The AAV Vector Toolkit: Poised at the Clinical Crossroads. Mol Ther 20:699–708.

59. Wu P, Phillips MI, Bui J, Terwilliger EF. 1998. Adeno-associated virus vector-mediated transgene integration into neurons and other nondividing cell targets. J Virol 72:5919–5926.

60. Fisher KJ, Jooss K, Alston J, Yang Y, Haecker SE, High K, Pathak R, Raper SE, Wilson JM. 1997. Recombinant adeno-associated virus for muscle directed gene therapy. Nat Med 3:306–312.

61. Xiao X, Li J, Samulski RJ. 1996. Efficient long-term gene transfer into muscle tissue of immunocompetent mice by adeno-associated virus vector. J Virol 70:8098–108.

62. Castle MJ, Gershenson ZT, Giles AR, Holzbaur ELF, Wolfe JH. 2014. Adeno-associated virus serotypes 1, 8, and 9 share conserved mechanisms for anterograde and retrograde axonal transport. Hum Gene Ther 25:705–20.

63. DiMattia MA, Nam HJ, Van Vliet K, Mitchell M, Bennett A, Gurda BL, McKenna R, Olson NH, Sinkovits RS, Potter M, Byrne BJ, Aslanidi G, Zolotukhin S, Muzyczka N, Baker TS, Agbandje-McKenna M. 2012. Structural insight into the unique properties of adeno-associated virus serotype 9. J Virol 86:6947–6958.

64. Foust KD, Nurre E, Montgomery CL, Hernandez A, Chan CM, Kaspar BK, Curtis M, Kaspar BK. 2009. Intravascular AAV9 preferentially targets neonatal-neurons and adult-astrocytes in CNS. Nat Biotechnol 27:59–65.

CHAPTER 5

COMPARISON OF THE VISCO-ELASTIC PROPERTIES OF VIRUSES, VIRUS BASED NANOMATERIALS AND ACTIVE PROTEIN CAGES

Contribution of Authors and Co-Authors

Manuscript in Chapter 5

Author: Ravi Kant

Contributions: Data collected and analyzed, prepared the manuscript

Co-Author: Vamseedhar Rayaprolu

Contributions: Data collected and analyzed, prepared the manuscript

Co-Author: Brian Bothner

Contributions: Obtained funding, discussed the results and implications and edited the manuscript.

Manuscript Information Page

COMPARISON OF THE VISCO-ELASTIC PROPERTIES OF VIRUSES, VIRUS BASED NANOMATERIALS AND ACTIVE PROTEIN CAGES

Authors: Ravi Kant, Vamseedhar Rayaprolu, Brian Bothner

Journal:

Status of Manuscript:
_ x _ Prepared for submission to a peer-reviewed journal
____ Officially submitted to a peer-review journal
____ Accepted by a peer-reviewed journal
____ Published in a peer-reviewed journal

Publisher:

CHAPTER 5

COMPARISON OF THE VISCO-ELASTIC PROPERTIES OF VIRUSES, VIRUS BASED NANOMATERIALS AND ACTIVE PROTEIN CAGES

Abstract

QCM-D study is conducted to compare and understand the biomechanical properties of different protein cages. Protein cages under study vary from non-icosahedral to icosahedral (viruses). A simple theoretical model is used to establish the relationship between diameter and particle rigidity. In addition, correlation between rigidity and triangulation number is compared. Our analysis suggest that change in rigidity simply do not correlate with diameter, triangulation number rather shares a more complex relationship. Therefore, we propose that altered subunit interactions contribute decisively to predict the change in protein shell rigidity.

Introduction

Viruses are the most abundant biological entities on earth. An important feature of icosahedral viruses is the symmetric supramolecular shell composed of protein subunits that serve to protect and deliver the encapsulated genome. The geometric arrangement of subunits imparts a multitude of physical properties that facilitate receptor binding, entry, genome release, virus assembly and maturation. Such an icosahedral architecture is stabilized by protein-protein and protein-nucleic acid interactions. Interestingly, this type of periodic arrangement of proteins is not limited to viruses and can be seen in other cages

like ferritins and heat shock proteins (1, 2) with the only difference being the lack of nucleic acid interactions. Viruses have evolved to accommodate genetic material of varying lengths by manipulating the arrangement of these proteins and varying the number of subunits that compose a capsid.

Structure and function functional analyses of icosahedral particles have been studied for the years (3, 4), however, direct measurements of mechanical properties has only recently been possible (5–7). Nano-indentation experiments using atomic force microscopy (AFM) on viruses provide the relationship between the force exerted on the capsid and the resultant deformation. This is represented using the Force-Displacement Curves (FDCs), which allow the rigidity of the virus particle to be estimated. FDCs estimate the mechanical strength of the capsids which facilitates a direct comparison between viruses. QCM-D has been emerged as a very potent complementary technique to investigate the biomechanical changes in big protein complexes. QCM-D has the ability to detect a small scale and large scale changes that are associated with the biological functions (8–10).

QCM-D is a surface technique that takes advantage of the piezoelectric property of quartz. The gold-coated quartz crystal used in the measurements is driven by applying pulses of alternating current inducing it to oscillate at a precise frequency. A change in frequency, proportional to the mass change, is observed when a sample is deposited on to the surface of the crystal sensor. When the AC voltage is interrupted, the crystal oscillation decays exponentially, also known as “ringing down”. The rate of decay is recorded, and the frequency and damping (or dissipation) are extracted. While the frequency is relative

to the mass deposited on the crystal, dissipation is dependent on the viscoelastic properties of the sample. Dissipation is defined as the sum of all energy losses in the system per oscillation (Equation 1),

$$D = \frac{E_{dissipated}}{2\pi E_{stored}} = \frac{1}{\pi f \tau} \qquad (1)$$

Where D is dissipation, $E_{dissipated}$ is the energy lost from the crystal, E_{stored} is the energy retained in the crystal, f is frequency, and τ is the time constant. Samples that strongly couple to the crystal oscillation contribute less to the dissipation and are classified as relatively rigid materials. Similarly, soft materials show higher deformation and dissipate more energy. QCM-D is a well-established technique that has been implemented to understand various biomedical applications. These applications include DNA based sensors, DNA hybridization, DNA-protein interactions, lipid surface interactions and bioactive surfaces consisting of protein layers (biofilms) (11–17). Instead of wide spread applications, QCM-D has not been explored much to understand changes in big protein complexes. Viruses are multidalton protein complexes which are very primitive life forms, therefore a foundation to understand the structure functional relationship. QCM-D has a potential to display the biomechanical changes in viruses but hasn't been explored enough.

In the current study, we attempt to showcase the power of QCM-D and demonstrate its potential for a widespread application. The viral and protein platforms studied in the current work have been isolated from a range of different species, such as algae, bacteria, moths, plants and primates, and portray the diversity of these supramolecular complexes. Along with diversity in their host range, these complex platforms also represent a variety of size classes. To understand and compare the viscoelastic differences among different

protein cages, we provide the first instance of a carefully curated library of different viruses and protein cages using QCM-D (Figure 5.1).

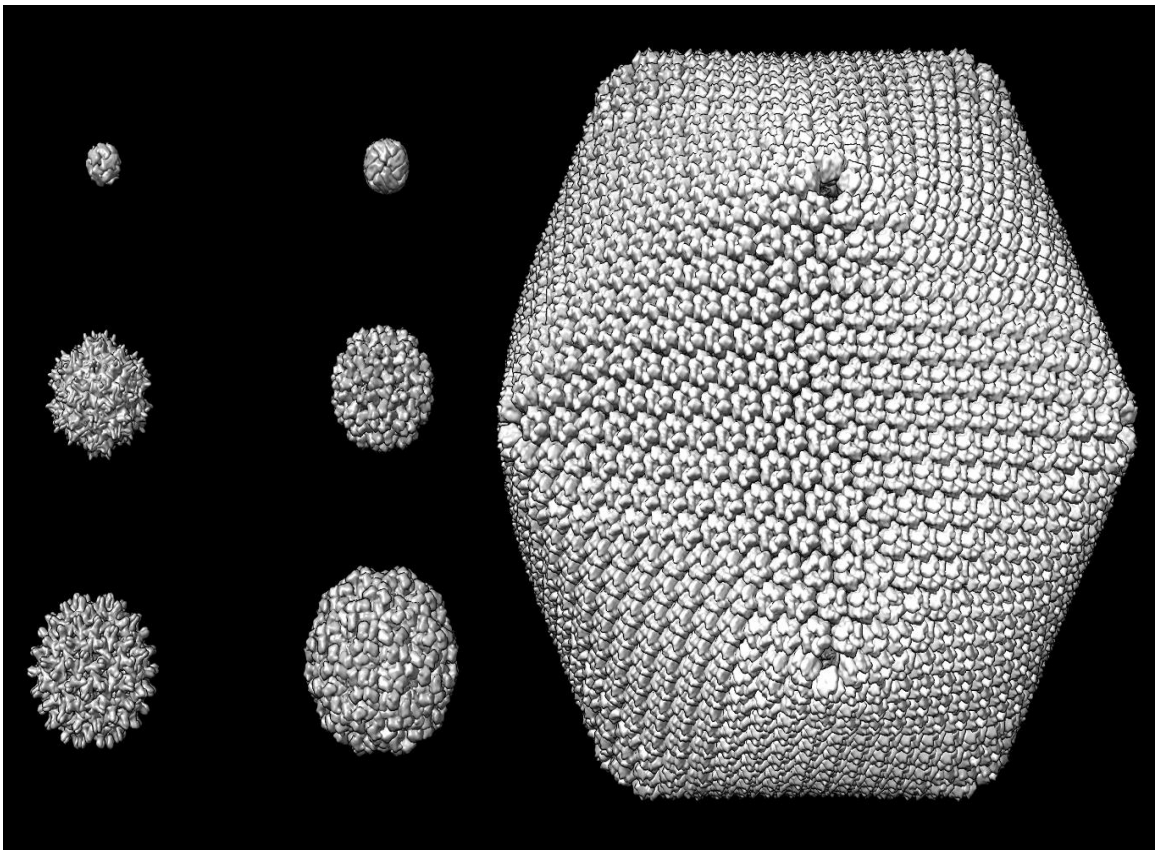


Figure 5.1. Virus and protein cage library. Protein cages and viruses of diameters ranging from 10nm to 190nm were used in this study. A. Dps-L, ~10nm (Gauss et al, 2006) B. H-ferritin, ~12nm (Hempstead et al, 1997) C. AAV2, ~28nm (Xie et al, 2002) D. CCMV, ~29nm (Speir et al, 1995) E. HBV, ~35nm (Wynne et al, 1999) F. NωV, ~41nm (Canady et al, 2001) G. PBCV-1, ~190nm (Yan et al, 2000).

We chose a wide range of cages from non-icosahedral to icosahedral symmetry to understand the architectural differences. To also expand our understanding about nano assemblages, protein cages that were much smaller than the viruses were also included in the analysis. The samples utilized in the current study can further be broadly classified into

three categories. 1) Nanomaterials that are under active development for drug and gene delivery for therapeutic purposes: AAVs (Adenoassociated viruses) CCMV, Dps-L, H-ferritin 2) Those that pose a major threat to human health (HBV: Hepatitis B virus) 3) Model and proof of concept systems NωV (Nudaurelia capensis omega virus) and PBCV-1 (Paramecium bursaria chlorella virus).

Our comparison points to a complex relationship between the diameter, T-numbers, and protein-protein interactions of the virus/protein cages to its rigidity. Our work shows that QCM-D acts as a common platform to not only compare biological entities amongst themselves but also with their nanomaterial counterparts while providing insights into both biology and material design.

Materials and Methods

QCM-D Experiment

The viscoelastic properties of different protein cages were explored by using QCM-D (Q-Sense D300 system, Q-Sense AB, Goteborg, Sweden). For these measurements, gold coated quartz crystal (AT cut) with a fundamental resonant frequency of 5MHz was used. Baseline was established with their respective storage buffers and recorded for 10 minutes. Each sample (0.01mg/mL, 0.6mL) were then gradually deposited on the crystal and allowed it to stabilize for 45min. To remove the loosely bound viral particles, gold surface was then washed with 0.6mL of same buffer for 10min. For Nudaurelia capensis omega virus, after wash step, another buffer exchange step with pH 5.0 buffer was introduced and

sample were allowed to incubate for 2 hours. Buffer exchange control was run to take into account the buffer exchange effect.

After every run, gold surface was cleaned and regenerated by soaking the crystal in a 1:1:5 mixture of H_2O_2 (30%), NH_3 (25%), and distilled water at 60^{o}C for 15min followed by exposure to UV light in UV chamber for 10 min. All samples were run in random order in triplicate and every time fresh cleaned crystal was used. Frequency and dissipation values were obtained at fundamental frequency 5MHz and three overtones (15MHz, 25MHz and 35MHz). Rigidities were calculated by taking the ratio of change in frequency to change in dissipation, $|\Delta F/\Delta D|$.

Rigidity Modeling

We developed a theoretical model to understand the relationship between the diameter of the shell and its rigidity. We considered an icosahedral virus particle in buffer with hydrodynamic diameter of π. When the virus is overlaid onto a QCM-D quartz crystal and the crystal is excited, the virus is subjected to shearing forces from the surrounding buffer. These shearing forces cause stress and strain on the virus particle where stress is defined as the shearing force acting per unit virus surface area and strain is defined as the distortion occurring in the virus due to the force applied. A ratio of the stress to the strain is defined as the shear modulus and is a well-known parameter to describe the rigidity of a substance, in this case, the virus. The classical representation of shear (26) is given by,

$$\frac{F}{A} = S\,\frac{\Delta x}{y}$$

Where F is the shearing force exerted by the liquid, A is the area on which the force is being exerted, S is the shear modulus, Δx is the distortion occurring and y is the

length/diameter. Shear stress is expressed in SI Δf/ΔD units as Pascals (N/m^2) and shear strain is unitless. Therefore, shear modulus is also expressed as Pascals.

To attain a reasonable representation of the model we assumed that a) the virus particle with its hydrodynamic shell is a sphere, b) the force applied on the virus is constant during the course of all experimental runs and c) the virus particle on the crystal does not disintegrate due to the force applied. Virus particles are generally very rigid entities and resist high internal pressures to package their genomes (27, 28) and have been known to resist large external forces by AFM (29, 30). With these assumptions in place, we estimated that the area that the shearing forces act on would be equal to $2\pi r^2$ where r is the radius of the hydrodynamic shell. The length of the virus in this case is the diameter, π. There are three possible scenarios with the deformation of the virus. a) Δ*x* is constant for all viruses. In other words, the amount of change observed in all tested samples is relatively equal. For the ease of calculation and understanding we assigned an arbitrary value of 10 Δf/ΔD units to Δ*x*. Inputting these values into the equation, we get $S = \frac{F}{5\pi^2}$. In scenario b) Δ*x* increases with increase in virus particle size. For simplicity, we increased *x* by 1 unit with each increase in size of the virus. For example, if the virus size increased from π to 2π, we increased Δ*x* from 10 to 11. And finally scenario c) was the opposite of scenario b, where Δ*x* decreased with each increase in virus particle size. For example, we decreased x by 1 unit with each increase in size of the virus. We then calculated S for viruses with diameters 2π, 3π and so on in all three scenarios. The three graphs obtained for the different virus diameters are plotted in Figure 5.3.

Results and Discussion

Small Protein Cages Exhibits Higher Rigidity

To explore the trend in rigidity across small and larger protein cages (viruses) QCM-D data was collected for the whole library (Table 5.1).

Table 5.1. QCM-D library of different protein cages

Protein cages	|Δf/ΔD| at 15 MHz	Diameter (nm)	Triangulation number (subunits)
DPS-L	52.4 ± 1.0	10	12
H-Ferritin	36.6 ± 0.9	12	24
CCMV (closed)	15.4 ± 0.1	26	3 (180)
XL-CCMV (closed)	49.6 ± 2.5	26	3 (180)
XL-CCMV (mineralized)	59.0 ± 0.3	26	3 (180)
CCMV (swollen)	12.9 ± 0.2	28.6	3 (180)
AAV 2	20.1 ± 0.5	28-29	1 (60)
AAV 1	22.2 ± 0.2	28-29	1 (60)
AAV 8	25.6 ± 0.6	28-29	1 (60)
AAV 5	25.8 ± 0.8	28-29	1 (60)
HBV 1-183 (WT)	15.0 ± 0.3	36	4 (240)
HBV 1-183 (EEE)	16.1 ± 0.4	36	5 (240)
HBV 1-149 (WT)	7.7 ± 0.2	36	4 (240)
NWV CAPSID	18.2 ± 0.5	41	4 (240)
NWV PROCAPSID	17.5 ± 0.3	45	4 (240)
PBCV - 1	4.1 ± 0.3	190	169 (5040)

The smallest protein cages in the library are Dps-L and human H-ferritin. Dps-L is a 10nm, dodecameric cage-like particle isolated from the hyperthermophilic archaeal species *Sulfolobus solfataricus.* This is primarily involved in cellular response to oxidative stress. 24 subunits of recombinant human H-ferritin self-assemble with an octahedral symmetry into a 12nm empty shell and function to direct bio-mineralization of iron and maintain iron homeostasis. Our previous work with Cowpea chlorotic mottle virus (wtCCMV), was the first time QCM-D had been used to compare rigidities of viruses and

virus based nanomaterials (18). Comparing the values for Dps-L and H-ferritin to wtCCMV, an increase in rigidity was observed with decrease in particle size. Dps-L showed an increase of 37 Δf/ΔD units (~71%) while H-ferritin showed an increase of 21.2 Δf/ΔD units (~42%) in rigidity. While the data fit into scenario #2 of our theoretical rigidity model well, it was intriguing that with a size reduction of only 3nm, Dps-L showed an increase in rigidity of 15.8 Δf/ΔD units (~70%) over H-ferritin.

Cross Linking Leads to High Capsid Rigidity

Adding the modified versions of CCMV (X-linked and M-X-linked) to this comparison provided a more significant perspective. X-linked CCMV showed an increase in rigidity of 34.2 Δf/ΔD units compared to its wildtype counterpart and almost all of this increase could be attributed directly to the cross-linking. With Dps-L, the rigidity was about 2.8 Δf/ΔD units (~5%) higher than the X-linked. Taking these two comparisons together, we could say that the strength of protein-protein, protein-nucleic acid and cross-linking interactions in X-linked are equivalent to about 95% of the strength of protein-protein interactions seen in Dps-L. Out of the 95%, 30% are contributed by native protein-protein and protein-nucleic acid interactions while the remaining 65% are due to the cross-links. H-ferritin, on the other hand, shows 13 Δf/ΔD units with lower rigidity than the X-linked. A comparison as above shows that the strength of protein-protein interactions in H-ferritin could be equivalent to ~74% of that in X-linked. Further, the rigidity imparted due to mineralization alone could be seen in the 9.4 unit increase (~16%) in M-X-linked compared to X-linked.

C- Terminal Domain in HBV Leads To

Increase in Protein-Protein Interactions

This was a very striking observation and showed that the protein-protein interaction in small cages contribute to the higher rigidity. To further validate our observation to bigger cages, we tested the empty nucleocapsid core of Hepatitis B virus (HBV), a dsDNA virus with a nucleocapsid core diameter of ~35nm. HBV is an enveloped virus with T=4 icosahedral symmetry and is the cause for Hepatitis B induced liver cirrhosis and cancer. This choice of sample was prompted due to three reasons. i. HBV is a DNA virus that infects animals, similar to AAV. ii. HBV is a T = 4 virus like NωV though smaller in size iii. HBV has had very big health and economic implications on the society. We compared the nucleocapsid core assembled *in vitro* using truncated (residues 1-149) and non-truncated capsid core (1-183). Truncated and non-truncated wt-HBV gave a value of 7.7 and 15.0 $\Delta f/\Delta D$ units respectively (Figure 5.2). This shows that presence of CTD (C terminal domain) (150-183) provided rigidity (48% higher) to the capsid without increasing the capsid diameter. This strongly suggests that presence of extra amino acids leads to an effective interaction among coat subunits. Results were even more interesting while comparing the mutant EEE (three CTD serines were replaced with glutamate) and wild type non-truncated HBV samples. Mutant HBV showed a slightly increase in the rigidity (1.0$\Delta f/\Delta D$ unit) in comparison to wt HBV (Figure 5.2). A previous study comparing non-truncated mutant and wt HBV has suggested that in mutant HBV is more thermally stable due to enhanced electrostatic interactions and also much slower rate of proteolytic cleavage than wild type (19). Therefore, higher rigidity was expected and we showed that QCM-D has the potential to detect even small changes in the structure. This is another relevant

example where proteins interactions contribute to increase in rigidity rather than increase in size.

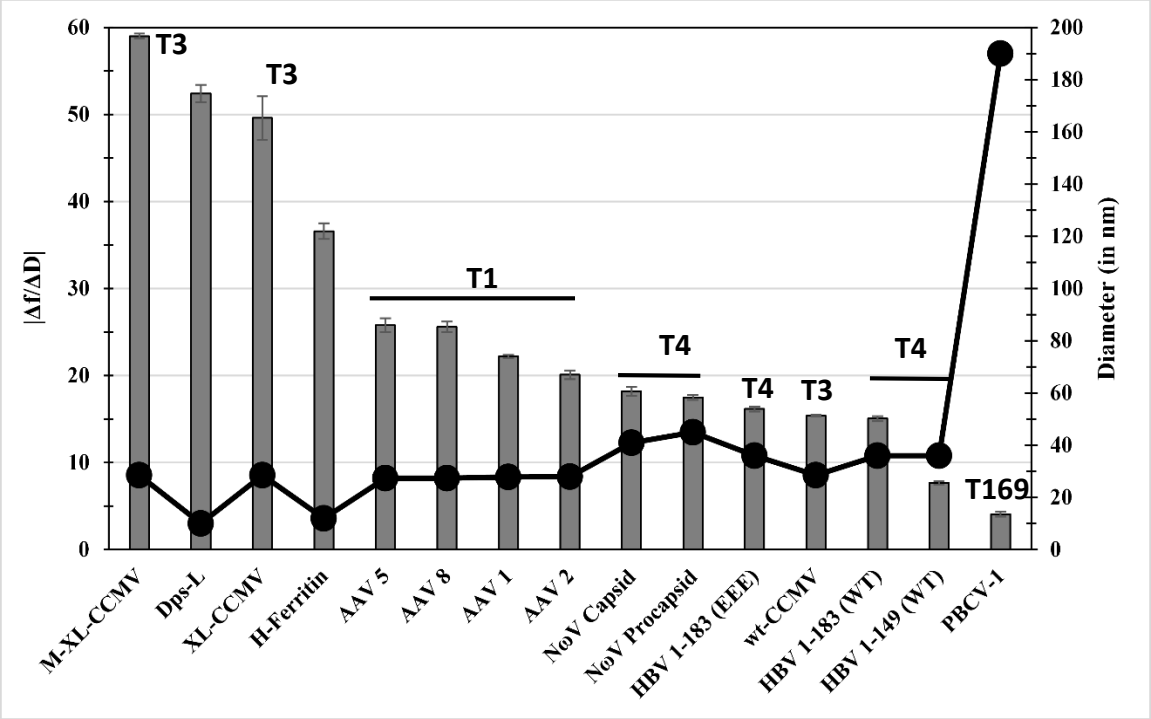


Figure 5.2: Rigidity, size and T-number of the various samples used in the study. The column graph (y1 axis) represents the rigidity (|Δf/ΔD|) values while the respective sizes of each of the samples are represented using the line plot (y2 axis). The T numbers of the samples are listed on the top of their respective columns. Note that Dps-L and H-ferritin do not have a T-number listed on them. These are not viruses and hence are not classified according to the Caspar and Klug principles of virus structure (31).

AAV5 Exhibits Highest Rigidity
among Tested Adeno-Associated Viruses

Inspired by the results from more complicated T=4 (240 subunits) HBV capsid, we sought to investigate a lesser complicated T=1 (60 subunits) human virus AAV capsids. Different serotypes of Adeno-associated virus (AAV1, AAV2, AAV5 and AAV8) were tested. There were 3 main reasons to test AAVs: i. AAV is an animal virus containing ssDNA, unlike CCMV, ii. AAV is a T=1 virus unlike HBV and with similar diameter to

CCMV (~29nm). iii. The 4 different serotypes belong to different clades (20) and have different solution phase properties (21). From the rigidity model, we predicted that the AAVs would have values similar to CCMV though this was not the case. AAV5 showed the highest rigidity at 25.8 Δf/ΔD units closely followed by AAV8 at 25.6 Δf/ΔD units, a ~40% increase in both cases compared to wtCCMV. AAV2 and AAV1 were at 22.2 and 20.1 Δf/ΔD units, a ~30% and ~23% increase respectively. From the previous work on AAVs, we know that AAV5 also showed the highest thermal and proteolytic stability. So, it was not surprising to see it at the top of the rigidity list too. AAVs followed the same trend as HBV where increase in rigidity in rigidity is observed without a change in diameter. What intrigued us was the relatively high rigidity of all the AAVs compared to similar sized CCMV. The AAVs did not fit into our current rigidity model but this also led us to factors other than size that could have an influence on rigidity.

Nωv Shows a High Rigidity Despite a Bigger Size

In recent years, the structure and the biophysical properties of (NωV), another T=4 virus, have been characterized to a point where it is now considered a model system for maturation in ssRNA viruses. Maturation involves the reduction in virus size from a 45nm procapsid at pH 7 to a 41nm capsid at pH 5. The procapsid is spherical with the subunits arranged as dimers while the capsid has the subunits arranged as trimers and in an icosahedron. More importantly, at the lower pH an autoproteolytic cleavage event is triggered which makes the transition from procapsid to capsid irreversible. It is easy to see why NωV acts as a great model platform for this work. It provides the option to test both the effect of size and the change in surface area of protein in a single system. In our studies,

we tested both forms with their genome packaged. It was surprising to see that even with a size change of ~4nm, the rigidities of the two forms were essentially the same and were 17.5 and 18.2 for the procapsid and capsid respectively. With respect to the rigidity model, these values were much higher than expected for a virus of this size. An interesting thing to note here is that the NωV tested here is not an empty capsid, therefore, coat proteins and genome interaction plausibly contribute to high rigidity.

PBCV Exhibits Least Rigidity in the Library

Viruses come in a diverse set of sizes and we are willing to test other macromolecular system that did not fall into or was even close to the size ranges (10-45nm). To test the validity of our hypothesis, we extended our QCM-D study to a larger and much more complicated system. So, we collected data on PBCV-1 a 190nm, algal, dsDNA virus. PBCV-1 has a T=169 icosahedral symmetry and contains ~150 gene products in the mature virion. Although it is an algal virus, a related virus (ATCV-1) has been recently found in the oropharyngeal samples of healthy adults and has been associated with decrease in cognitive functions in human and mice (22). PBCV-1 not only represents the largest virus we've tested, but also has a highly complex virus structure as seen from the number of gene products incorporated into the mature virion. It also gave us the smallest rigidity value, 4.1 $\Delta f/\Delta D$ units, among all the viruses tested.

$\Delta f/\Delta D$ Ratio Corroborates With The
Proposed Theoretical Model with Some Outliers

With the data from several different viruses and protein cages in hand, we compared our theoretical model with the collected data. The QCM-D data is plotted in Figure 4 along

with the data fitted to a single exponential fit. When this is compared to the previously simulated theoretical model, we noticed that the QCM-D data fits reasonably well to the proposed model. While the first two scenarios indicate predictable behavior for any hydrodynamic shells, this final scenario indicates that with an increase in size of the shell, resistance to distortion is observed. This could happen only if shells become more rigid as they become larger. In the context of protein shells, this is counterintuitive as we would expect proteins to behave mostly according to scenario 2.

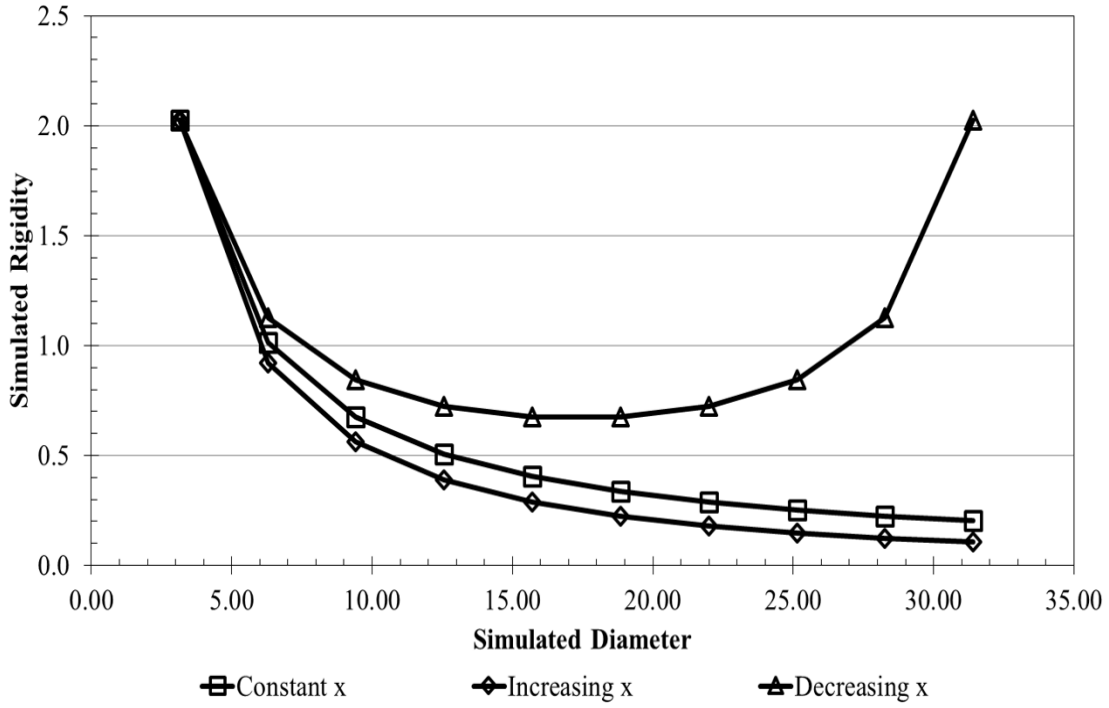


Figure 5.3: A scatter plot of simulated rigidity versus simulated diameter. Three different scenarios involving the change in strain are shown here. The term "Constant x" is used to describe a constant absolute amount of strain irrespective of the diameter of the sample being tested. "Increasing x" is used to describe a proportionate increase in strain with increase in diameter of sample. Similarly, "Decreasing x" is used to describe a proportionate decrease in strain with increase in diameter of sample.

Though it is difficult to precisely point out whether it fits scenario 2 or scenario 3 (Figure 5.3). We could speculate and say that with an increase in the size of the virus, there would be an increase in the distortion. This puts our data in the regime of scenario 3. We noticed a decreased in rigidity along with an increase in diameter. This observation is valid till the comparison is among different protein cages. But this is not consistent when we compare the rigidity trend with in group example AAVs and HBVs. In both groups, different rigidity in different serotypes were observed without a change in diameter. The outliers to our data are also plotted in Figure 5.4.

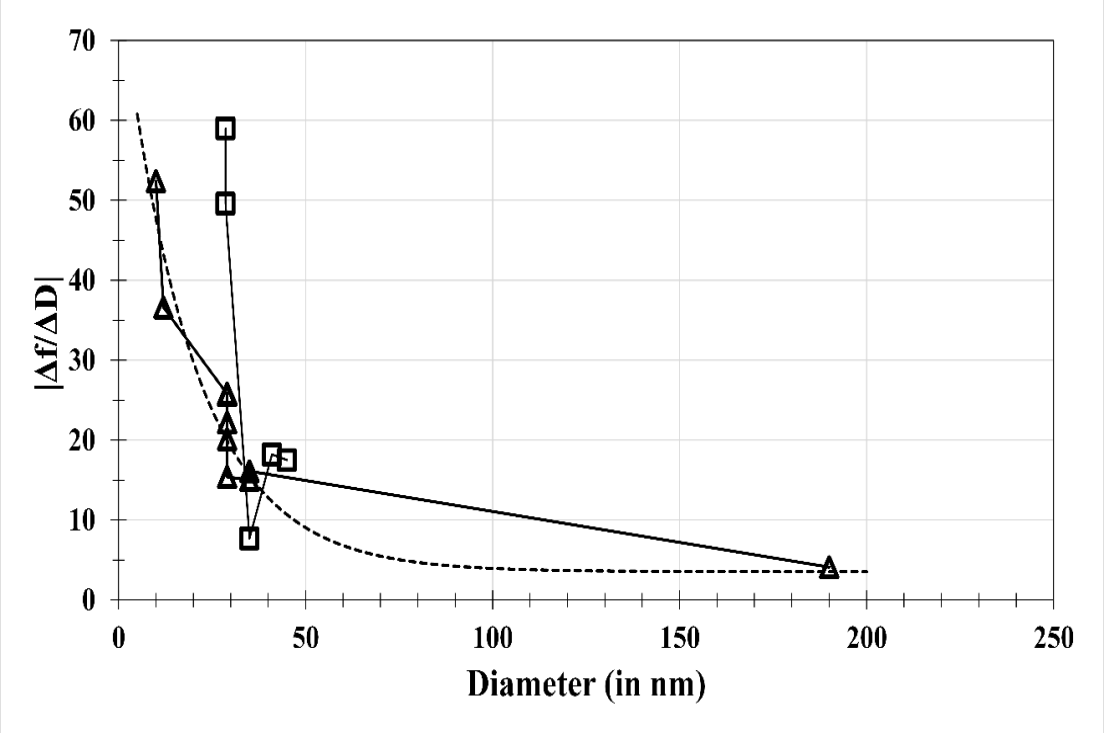


Figure 5.4: A scatter plot of rigidity (|Δf/ΔD|) vs the Diameter of the samples seen in Figure 5.2. The triangular markers represent a subset of the samples which were used to generate an exponential fit, shown as the dashed line. The square markers represent data from M-X-linked, X-linked, truncated HBV (1-149), NωV capsid and procapsid samples. These were considered outliers.

Outliers include modified CCMVs, truncated HBV(1-149) and NωV. We expected modified CCMV as one due to induced interactions by means of cross linking. NωV came up as a really surprise where a high rigidity is observed that could be a combined effect of increased inter-coat proteins and genome-coat proteins interaction. HBV (1-149) is a nucleocapsid core made up of truncated dimers, hence not surprised to see as outliers.

Rigidity and Triangulation Numbers Shows No Direct Relationship

Although virus structures are considered best represented by their T-numbers, it is clear here that there are some subtle and not so subtle differences that also need to be accounted for. For example, while AAV and CCMV have similar diameters, their T-numbers and rigidities are different. The AAV subunit protein is 3-4 times higher in molecular weight, occupies a much larger surface area, has many more protein-protein interactions and therefore has higher association energy in the capsid. All of these attributes contribute to the higher rigidity of AAV. On the other hand, NωV and HBV share the same T-number and still show very different rigidities with NωV being at least 10 $\Delta f/\Delta D$ units (42-44%) higher than HBV. NωV capsid protein has 4 times higher molecular weight than that HBV capsid protein and consequently has a much larger surface area available for protein-protein interactions. This could enhance the overall rigidity of the NωV capsid as well as the procapsid. It is also important to note that the HBV sample was the empty nucleocapsid core assembled from non-truncated proteins is relatively less rigid despite belong to high triangulation number and relatively smaller size than NωV. Nevertheless, the observed difference is significant and may indicate that the nucleocapsid cores of

enveloped animal viruses are more flexible than previously thought. In fact, a recent study observed disordered nucleocapsid cores in Rossriver virus (24) an enveloped T=4 alphavirus. This disorder could presumably facilitate genome release upon infection. The assembly competent HBV capsid protein has no known human homolog and therefore is a prime therapeutic target. Knowledge about the physical properties of HBV would promote rational and more efficient drug design.

While on one end of this size spectrum stand the small protein shells, Dps-L and H-ferritin, the other end is described by PBCV-1, one of the largest viruses discovered. While Dps-L and H-ferritin are not icosahedral and cannot be assigned a T-number, PBCV-1 has a T-number of 169 with 5040 total proteins forming its shell. A straightforward comparison of hydrodynamic diameter tells us that Dps-L and H-ferritin would have a much higher rigidity compared to PBCV-1. But a more detailed comparison helps us understand the effect of protein-protein interactions in these systems. The number of proteins and hence the number of protein-protein interactions in PBCV-1 are at least 2 orders of magnitude higher than the Dps-L and H-ferritin. But, interestingly, this increase does not translate to an increase in rigidity of the whole structure.

Drawing a direct correlation between size/symmetry to the rigidity of a virus particle could lead to incorrect interpretations. We suggests that the increased subunit interactions play a decisive role in deciding the global rigidity of the protein cages. This interaction can be independent diameter, size and triangulation number. A previous study involving simulations on AFM nanoindentations done on 35 different viruses (25) showed that mechanical properties of protein shells depend on T-number, the number of amino

acids, the mean capsid radius, the capsid width and most importantly the backbone and side chain interactions in the subunits. The simulations compared CCMV, HBV and NωV among other viruses. Cieplak et al found that the mechanical properties of the viruses tested are a not a direct function of size or the symmetry but are strongly correlated to the number of interactions each amino acid makes (25). In fact, the full range of small scale deformations and large irreversible transitions noticed by them could be observed using just the viruses in a radius range of 13.0-13.4nm. Cieplak et al also observed that the mechanical properties of viruses with large shell thickness showed a larger variation (25). In our study, we noticed a weak correlation between increasing shell thickness and decreasing rigidity with PBCV-1 showing the largest shell thickness and the lowest rigidity. That said, it is difficult to correlate shell thickness directly to rigidity with our current data as most of the shell thicknesses of our samples fall in the range of 5-10 nm with the exception of PBCV-1 (~19nm).

Conclusions

The QCM-D results presented here follow similar trends demonstrated with AFM and AFM simulations. However, there are several key points where the power of QCM-D shines. QCM-D values are generated in near physiological conditions where the samples are being subjected only to shear forces by the liquid medium, as would be the case in biological systems. We also demonstrate that with minimal changes to the measurement protocols, we are able to measure extremely altered virus particles (Ex: X-CCMV and M-X-CCMV) and with the same speed and reproducibility. This positions QCM-D as a semi-

high throughput method for viral particle characterization. While rigidity obtained from simple QCM-D analysis is central to the technique, it can also be used to measure the thickness of the deposited layer and carefully design thin films with desired properties. These are essential details needed for material synthesis using biological components.

References

1. Gauss GH, Benas P, Wiedenheft B, Young M, Douglas T, Lawrence CM. 2006. Structure of the DPS-like protein from Sulfolobus solfataricus reveals a bacterioferritin-like dimetal binding site within a DPS-like dodecameric assembly. Biochemistry 45:10815–27.

2. Lawson DM, Artymiuk PJ, Yewdall SJ, Smith JM, Livingstone JC, Treffry A, Luzzago A, Levi S, Arosio P, Cesareni G. 1991. Solving the structure of human H ferritin by genetically engineering intermolecular crystal contacts. Nature 349:541–4.

3. Caspar DLD, Klug A. 1962. Physical principles in the construction of regular viruses. Cold Spring Harb Symp Quant Biol 27th:1–24.

4. Johnson JE, Speir J a. 1997. Quasi-equivalent viruses: a paradigm for protein assemblies. J Mol Biol 269:665–75.

5. Ivanovska IL, de Pablo PJ, Ibarra B, Sgalari G, MacKintosh FC, Carrascosa JL, Schmidt CF, Wuite GJL. 2004. Bacteriophage capsids: tough nanoshells with complex elastic properties. Proc Natl Acad Sci U S A 101:7600–7605.

6. Gibbons M, Klug W. 2007. Nonlinear finite-element analysis of nanoindentation of viral capsids. Phys Rev E 75:1–11.

7. Roos WH, Wuite GJL. 2009. Nanoindentation Studies Reveal Material Properties of Viruses. Adv Mater 21:1187–1192.

8. Rydell GE, Dahlin AB, Höök F, Larson G. 2009. QCM-D studies of human norovirus VLPs binding to glycosphingolipids in supported lipid bilayers reveal strain-specific characteristics. Glycobiology.

9. Rayaprolu V, Manning BM, Douglas T, Bothner B. 2010. Virus particles as active nanomaterials that can rapidly change their viscoelastic properties in response to dilute solutions. Soft Matter 6:5286.

10. da Silva AK, Kavanagh O V, Estes MK, Elimelech M. 2011. Adsorption and aggregation properties of norovirus GI and GII virus-like particles demonstrate differing responses to solution chemistry. Environ Sci Technol 45:520–6.

11. Nguyen TH, Elimelech M. 2007. Adsorption of plasmid DNA to a natural organic matter-coated silica surface: Kinetics, conformation, and reversibility. Langmuir 23:3273–3279.

12. Nguyen TH, Chen KL. 2007. Role of divalent cations in plasmid DNA adsorption

to natural organic matter-coated silica surface. Environ Sci Technol 41:5370–5375.

13. Nguyen TH, Elimelech M. 2007. Plasmid DNA adsorption on silica: Kinetics and conformational changes in monovalent and divalent salts. Biomacromolecules 8:24–32.

14. Keller CA, Kasemo B. 1998. Surface specific kinetics of lipid vesicle adsorption measured with a quartz crystal microbalance. Biophys J 75:1397–1402.

15. Cho NJ, Cho SJ, Kwang HC, Glenn JS, Frank CW. 2007. Employing an amphipathic viral peptide to create a lipid bilayer on Au and TiO2. J Am Chem Soc 129:10050–10051.

16. Schofield AL, Rudd TR, Martin DS, Fernig DG, Edwards C. 2007. Real-time monitoring of the development and stability of biofilms of Streptococcus mutans using the quartz crystal microbalance with dissipation monitoring. Biosens Bioelectron 23:407–413.

17. Wittmer CR, Phelps JA, Saltzman WM, Van Tassel PR. 2007. Fibronectin terminated multilayer films: Protein adsorption and cell attachment studies. Biomaterials 28:851–860.

18. Rayaprolu V, Manning BM, Douglas T, Bothner B. 2010. Virus particles as active nanomaterials that can rapidly change their viscoelastic properties in response to dilute solutions. Soft Matter 6:5286.

19. Selzer L, Kant R, Wang JCY, Bothner B, Zlotnick A. 2015. Hepatitis B virus core protein phosphorylation sites affect capsid stability and transient exposure of the C-terminal domain. J Biol Chem 290:28584–28593.

20. Gao G, Vandenberghe LH, Alvira MR, Lu Y, Calcedo R, Zhou X, Wilson JM. 2004. Clades of Adeno-associated viruses are widely disseminated in human tissues. J Virol 78:6381–8.

21. Rayaprolu V, Kruse S, Kant R, Venkatakrishnan B, Movahed N, Brooke D, Lins B, Bennett A, Potter T, McKenna R, Agbandje-McKenna M, Bothner B. 2013. Comparative Analysis of Adeno Associated Virus Capsid Stability and Dynamics. J Virol.

22. Yolken RH, Jones-Brando L, Dunigan DD, Kannan G, Dickerson F, Severance E, Sabunciyan S, Talbot CC, Prandovszky E, Gurnon JR, Agarkova I V, Leister F, Gressitt KL, Chen O, Deuber B, Ma F, Pletnikov M V, Van Etten JL. 2014. Chlorovirus ATCV-1 is part of the human oropharyngeal virome and is associated with changes in cognitive functions in humans and mice. Proc Natl Acad Sci U S A 111:16106–11.

23. Nault J-C, Datta S, Imbeaud S, Franconi A, Mallet M, Couchy G, Letouze E, Pilati C, Verret B, Blanc J-F, Balabaud C, Calderaro J, Laurent A, Letexier M, Bioulac-Sage P, Calvo F, Zucman-Rossi J. 2015. Recurrent AAV2-related insertional mutagenesis in human hepatocellular carcinomas. Nat Genet 47:1187–1193.

24. Wang JCY, Chen C, Rayaprolu V, Mukhopadhyay S, Zlotnick A. 2015. Self-Assembly of an Alphavirus Core-like Particle Is Distinguished by Strong Intersubunit Association Energy and Structural Defects. ACS Nano 9:8898–8906.

25. Cieplak M, Robbins MO. 2013. Nanoindentation of 35 Virus Capsids in a Molecular Model: Relating Mechanical Properties to Structure. PLoS One 8.

26. 2013. Structure and Physics of Viruses: An Integrated Textbook. Springer Science & Business Media.

27. Evilevitch A, Castelnovo M, Knobler CM, Gelbart WM. 2004. Measuring the force ejecting DNA from phage 1–15.

28. Ivanovska I, Wuite G, Jönsson B, Evilevitch A. 2007. Internal DNA pressure modifies stability of WT phage. Proc Natl Acad Sci U S A 104:9603–8.

29. Vliegenthart GA, Gompper G. 2006. Mechanical deformation of spherical viruses with icosahedral symmetry. Biophys J 91:834–41.

30. Snijder J, Ivanovska IL, Baclayon M, Roos WH, Wuite GJL. 2012. Probing the impact of loading rate on the mechanical properties of viral nanoparticles. Micron 1–8.

31. Klug, A and Caspar DL. 1960. The structure of small viruses. adv virus res 7:225–235.

CHAPTER 6

CONCLUDING REMARKS

The focus of this thesis has been to investigate the stability, biomechanical changes and dynamics of a tailed bacteriophage by applying multiple biophysical approaches. These biophysical parameters are important to understand the maturation of the capsid. Two viruses under study P22 and AAV are very diverse and both infects two different host: P22 infect bacteria and AAV infect humans. Our study shows that presence of metastable transitions in P22 set the foundation for the advanced quaternary interactions after expansion. These interactions results in enhanced hydrophobic core which provides the capsid stability and structural rigidity. Beside biology, advent of P22 as cargo nano-container, further asks for the biophysical characterization of the synesthetic capsid. This study is important that we have been able to put together a suite of complementary techniques that has a potential to explore the other natural and synthetic macromolecular systems. Our research on AAVs show that lipase domain activation is not mediated by complicated mechanism involving low pH and receptors. Rather, prolonged incubation is enough to circumvent the liposomal membrane to show the lipase domain activation. This study is very significant as AAVs are the vehicle for the gene transportation to treat different genetic disorders. We have been able to put together a method sensitive to detect event a trace amount of enzyme products. This LC-MS method has the potential to explore other of AAVs for understanding infection mechanism. This work also has the industrial application as lipase has been used for converting lipids to useful products for different

applications. Our set up has the ability to detect different products through efficient chromatography. Therefore, work in this thesis presented is important for many *in-vivo* and *in-vitro* applications.

REFERENCES CITED

1. Suttle C 2007. Marine viruses--major players in the global ecosystem. Nat Rev Microbiol 5:801–812.

2. Hendrix RW. 2002. Bacteriophages: Evolution of the Majority. Theor Popul Biol 61:471–480.

3. Baker ML, Jiang W, Rixon FJ, Chiu W. 2005. Common ancestry of herpesviruses and tailed DNA bacteriophages. J Virol 79:14967–70.

4. Holmes EC. 2011. What does virus evolution tell us about virus origins? J Virol 85:5247–5251.

5. Hendrix RW. 1999. Evolution: The long evolutionary reach of viruses. Curr Biol 9:914–917.

6. Duda RL, Hendrix RW, Huang WM, Conway JF. 2006. Erratum: Shared architecture of bacteriophage SPO1 and herpesvirus capsids (Current Biology (2006) 16 (R11-R13)). Curr Biol 16:440.

7. Johnson JE. 2010. Virus particle maturation: Insights into elegantly programmed nanomachines. Curr Opin Struct Biol 20:210–216.

8. Veesler D, Johnson JE. 2012. Virus maturation. Annu Rev Biophys 41:473–96.

9. Zlotnick A. 2005. Theoretical aspects of virus capsid assembly. J Mol Recognit 18:479–490.

10. Caspar DL. 1980. Movement and self-control in protein assemblies. Quasi-equivalence revisited. Biophys J 32:103–38.

11. Sarah K, Zlotnick A. 2009. The thermodynamics of virus capsid assembly. Met Enzymol. 455: 395–417.

12. Tuma R, Tsuruta H, French KH, Prevelige PE. 2008. Detection of intermediates and kinetic control during assembly of bacteriophage P22 procapsid. J Mol Biol 381:1395–406.

13. Bothner B, Taylor D, Jun B, Lee KK, Siuzdak G, Schultz CP, Schlutz CP, Johnson JE. 2005. Maturation of a tetravirus capsid alters the dynamic properties and creates a metastable complex. Virology 334:17–27.

14. Galisteo ML, King J. 1993. Conformational transformations in the protein lattice of phage P22 procapsids. Biophys J 65:227–35.

15. Wikoff WR, Liljas L, Duda RL, Tsuruta H, Hendrix RW, Johnson JE. 2000. Topologically linked protein rings in the bacteriophage HK97 capsid. Science

289:2129–2133.

16. Duda RL. 1998. Protein chainmail: Catenated protein in viral capsids. Cell 94:55–60.

17. Gertsman I, Gan L, Guttman M, Lee K, Speir JA, Duda RL, Hendrix RW, Komives EA, Johnson JE. 2009. An unexpected twist in viral capsid maturation. Nature 458:646–650.

18. Parent KN, Khayat R, Tu LH, Suhanovsky MM, Cortines JR, Teschke CM, Johnson JE, Baker TS. 2010. P22 coat protein structures reveal a novel mechanism for capsid maturation: stability without auxiliary proteins or chemical crosslinks. Structure 18:390–401.

19. Tuma R, Prevelige PE, Thomas GJ. 1998. Mechanism of capsid maturation in a double-stranded DNA virus. Proc Natl Acad Sci U S A 95:9885–9890.

20. Uchida M, Douglas T. 2013. Unravelling capsid transformations. Nat Chem 5:444–445.

21. Hendrix RW, Johnson JE. 2012. Viral Molecular Machines 726:351–363.

22. Chen D-H, Baker ML, Hryc CF, DiMaio F, Jakana J, Wu W, Dougherty M, Haase-Pettingell C, Schmid MF, Jiang W, Baker D, King J a, Chiu W. 2011. Structural basis for scaffolding-mediated assembly and maturation of a dsDNA virus. Proc Natl Acad Sci U S A 108:1355–1360.

23. Teschke CM, McGough A, Thuman-Commike P a. 2003. Penton release from P22 heat-expanded capsids suggests importance of stabilizing penton-hexon interactions during capsid maturation. Biophys J 84:2585–92.

24. Jiang W, Li Z, Zhang Z, Baker ML, Prevelige PE, Chiu W. 2003. Coat protein fold and maturation transition of bacteriophage P22 seen at subnanometer resolutions. Nat Struct Biol 10:131–5.

25. Dhillon EK, Dhillon ES, Lai AN, Linn S. 1980. Host range, immunity and antigenic properties of lamdoid coliphage HK97. J Gen Virol 50:217–220.

26. Gan L, Speir JA, Conway JF, Lander G, Cheng N, Firek BA, Hendrix RW, Duda RL, Liljas L, Johnson JE. 2006. Capsid Conformational Sampling in HK97 Maturation Visualized by X-Ray Crystallography and Cryo-EM. Structure 14:1655–1665.

27. Lee KK, Gan L, Tsuruta H, Moyer C, Conway JF, Duda RL, Hendrix RW, Steven AC, Johnson JE. 2008. Virus Capsid Expansion Driven by the Capture of Mobile Surface Loops. Structure 16:1491–1502.

28. Gertsman I, Fu C-Y, Huang R, Komives EA, Johnson JE. 2010. Critical Salt Bridges Guide Capsid Assembly, Stability, and Maturation Behavior in Bacteriophage HK97. Mol Cell Proteomics 9:1752–1763.

29. Veesler D, Quispe J, Grigorieff N, Potter CS, Carragher B, Johnson JE, Structure 20:1384–1390.

30. Duda RL, Martincic K, Xie Z, Hendrix RW. 1995. Bacteriophage HK97 head assembly. FEMS Microbiol Rev 17:41–46.

31. Bonds SI, Kang HJ, Coulibaly F, Clow F, Proft T, Baker EN. Stabilizing Isopeptide Bonds Revealed in Gram-Positive Bacterial Pilus Structure, 2007, Science.318.

32. Earnshaw W, Casjens S, Harrison SC. 1976. Assembly of the head of bacteriophage P22: X-ray diffraction from heads, proheads and related structures. J Mol Biol 104:387–410.

33. Casjens S, Adams MB, Hall C, King J. 1985. Autogenous Modulation of Bacteriophage 123:174–179.

34. Tatnall M, King J. 1981. Purification of the Coat and Scaffolding Procapsids of Bacteriophage P22 Virology 529–547.

35. Prevelige PE, Thomas D, King J. 1988. Scaffolding protein regulates the polymerization of P22 coat subunits into icosahedral shells in vitro. J Mol Biol 202:743–57.

36. Casjens S, Wyckoff E, Hayden M, Sampson L, Eppler K, Randall S, Moreno ET, Serwer P. 1992. Bacteriophage P22 portal protein is part of the gauge that regulates packing density of intravirion DNA. J Mol Biol 224:1055–1074.

37. Parker MH, Casjens S, Prevelige PE. 1998. Functional domains of bacteriophage P22 scaffolding protein. J Mol Biol 281:69–79.

38. Galisteo ML, King J. 1993. Conformational transformations in the protein lattice of phage P22 procapsids. Biophys J 65:227–35.

39. King J, Botstein D, Casjens S, Earnshaw W, Harrison S, Lenk E. *Phil. Trans.R.Soc.Lond*. B. 1976. 276, 37-49

40. Parker MH, Prevelige PE. 1998. Electrostatic interactions drive scaffolding/coat protein binding and procapsid maturation in bacteriophage P22. Virology 250:337–49.

41. Usselman RJ, Qazi S, Aggarwal P, Eaton SS, Eaton GR, Russek S, Douglas T. 2015. Gadolinium-Loaded Viral Capsids as Magnetic Resonance Imaging Contrast

Agents. Appl Magn Reson 46:349–355.

42. Patterson D, Edwards E, Douglas T. 2015. Hybrid Nanoreactors: Coupling Enzymes and Small-Molecule Catalysts within Virus-Like Particles. Isr J Chem 55:96–101.

43. Bedwell GJ, Zhou Z, Uchida M, Douglas T, Gupta A, Prevelige PE. 2015. Selective Biotemplated Synthesis of TiO2 inside a Protein Cage. Biomacromolecules 16:214–218.

44. Patterson DP, Schwarz B, Waters RS, Gedeon T, Douglas T. 2014. Encapsulation of an enzyme cascade within the bacteriophage P22 virus-like particle. ACS Chem Biol 9:359–365.

45. Patterson DP, Rynda-Apple A, Harmsen AL, Harmsen AG, Douglas T. 2013. Biomimetic antigenic nanoparticles elicit controlled protective immune response to influenza. ACS Nano 7:3036–3044.

46. Lo M, Aulabaugh A, Jin G, Cowling R, Bard J, Malamas M, Ellestad G. 2004. Evaluation of fluorescence-based thermal shift assays for hit identification in drug discovery Anal Biochem.332:153–159.

47. Vedadi M, Niesen FH, Allali-Hassani A, Fedorov OY, Finerty PJ, Wasney GA, Yeung R, Arrowsmith C, Ball LJ, Berglund H, Hui R, Marsden BD, Nordlund P, Sundstrom M, Weigelt J, Edwards AM. 2006. Chemical screening methods to identify ligands that promote protein stability, protein crystallization, and structure determination. Proc Natl Acad Sci U S A 103:15835–40.

48. Niesen FH, Berglund H, Vedadi M. 2007. The use of differential scanning fluorimetry to detect ligand interactions that promote protein stability. Nat Protoc 2:2212–21.

49. Rayaprolu V, Kruse S, Kant R, Venkatakrishnan B, Movahed N, Brooke D, Lins B, Bennett A, Potter T, McKenna R, Agbandje-McKenna M, Bothner B. 2013. Comparative Analysis of Adeno Associated Virus Capsid Stability and Dynamics. J Virol. 01415-13

50. Greenfield NJ. 2006. Using circular dichroism spectra to estimate protein secondary structure. Nat Protoc 1:2876–90.

51. Ranjbar B, Gill P. 2009. Circular dichroism techniques: biomolecular and nanostructural analyses- a review. Chem Biol Drug Des 74:101–20.

52. Kelly SM, Jess TJ, Price NC. 2005. How to study proteins by circular dichroism. Biochim Biophys Acta 1751:119–39.

53. Englander SW, Mayne L, Bai Y, Sosnick TR. 1997. Hydrogen exchange : The

modem legacy of Linderstrom-Lang Prot Sci. 6:1101–1109.

54. Tsutsui Y, Wintrode PL. 2007. Hydrogen/deuterium exchange-mass spectrometry: a powerful tool for probing protein structure, dynamics and interactions. Curr Med Chem 14:2344–58.

55. Hansma PK, Cleveland JP, Radmacher M, Walters DA, Hillner PE, Bezanilla M, Fritz M, Vie D, Hansma HG, Prater CB, Massie J, Fukunaga L, Gurley J, Elings V. 1994. Tapping mode atomic force microscopy in liquids. Appl Phys Lett 64:1738–1740.

56. Kuznetsov YG, McPherson A. 2011. Atomic Force Microscopy in Imaging of Viruses and Virus-Infected Cells. Microbiol Mol Biol Rev 75:268–285.

57. Kuznetsov YG, McPherson A. 2011. Atomic force microscopy in imaging of viruses and virus-infected cells. Microbiol Mol Biol Rev 75:268–285.

58. Kuznetsov YG, Gurnon JR, Van Etten JL, McPherson A. 2005. Atomic force microscopy investigation of a chlorella virus, PBCV-1. J Struct Biol 149:256–263.

59. Michel JP, Ivanovska IL, Gibbons MM, Klug WS, Knobler CM, Wuite GJL, Schmidt CF. 2006. Nanoindentation studies of full and empty viral capsids and the effects of capsid protein mutations on elasticity and strength. Proc Natl Acad Sci U S A 103:6184–6189.

60. Roos WH, Gertsman I, May ER, Brooks CL, Johnson JE, Wuite GJL. 2012. Mechanics of bacteriophage maturation. Proc Natl Acad Sci 109:2342–2347.

61. Roos WH, Ivanovska IL, Evilevitch a., Wuite GJL. 2007. Viral capsids: Mechanical characteristics, genome packaging and delivery mechanisms. Cell Mol Life Sci 64:1484–1497.

62. Dixon MC. 2008. Quartz crystal microbalance with dissipation monitoring: enabling real-time characterization of biological materials and their interactions. J Biomol Tech 19:151–8.

63. Rayaprolu V, Manning BM, Douglas T, Bothner B. 2010. Virus particles as active nanomaterials that can rapidly change their viscoelastic properties in response to dilute solutions. Soft Matter 6:5286.

64. Zlotnick A. 2003. Are weak protein-protein interactions the general rule in capsid assembly? Virology 315:269–274.

65. Ceres P, Zlotnick A. 2002. Weak protein-protein interactions are sufficient to drive assembly of hepatitis B virus capsids. Biochemistry 41:11525–11531.

66. Zlotnick A. 2005. Theoretical aspects of virus capsid assembly. J Mol Recognit 18:479–490.

67. Bothner B, Taylor D, Jun B, Lee KK, Siuzdak G, Schultz CP, Schlutz CP, Johnson JE. 2005. Maturation of a tetravirus capsid alters the dynamic properties and creates a metastable complex. Virology 334:17–27.

68. Prevelige PE, Thomas D, Aubrey KL, Towse S a, Thomas GJ. 1993. Subunit conformational changes accompanying bacteriophage P22 capsid maturation. Biochemistry 32:537–543.

69. Tuma R, Coward LU, Kirk MC, Barnes S, Jr PEP, Al B. 2001. Hydrogen-deuterium Exchange as a Probe of Folding and Assembly in Viral Capsids 389–396.

70. Conway JF, Wikoff WR, Cheng N, Duda RL, Hendrix RW, Johnson JE, Steven a C. 2001. Virus maturation involving large subunit rotations and local refolding. Science 292:744–748.

71. Lewis JK, Bothner B, Smith TJ, Siuzdak G. 1998. Antiviral agent blocks breathing of the common cold virus. Proc Natl Acad Sci U S A 95:6774–6778.

72. Speir J a, Bothner B, Qu C, Willits D a, Young MJ, Johnson JE. 2006. Enhanced local symmetry interactions globally stabilize a mutant virus capsid that maintains infectivity and capsid dynamics. J Virol 80:3582–91.

73. Lin J, Lee LY, Roivainen M, Filman DJ, Hogle JM, Belnap DM. 2012. Structure of the Fab-Labeled “Breathing” State of Native Poliovirus. J Virol 86:5959–5962.

74. Kale A, Bao Y, Zhou Z, Prevelige PE, Gupta A. 2013. Directed self-assembly of CdS quantum dots on bacteriophage P22 coat protein templates. Nanotechnology 24:045603.

75. Kang S, Uchida M, O’Neil A, Li R, Prevelige PE, Douglas T. 2010. Implementation of p22 viral capsids as nanoplatforms. Biomacromolecules 11:2804–9.

76. Patterson DP, Schwarz B, El-Boubbou K, van der Oost J, Prevelige PE, Douglas T. 2012. Virus-like particle nanoreactors: programmed encapsulation of the thermostable CelB glycosidase inside the P22 capsid. Soft Matter 8:10158.

77. King J, Botstein D, Casjens S, Earnshaw W, Harrison S, Lenk E. 1976. Structure and assembly of the capsid of bacteriophage P22. *Phil. Trans.R.Soc.Lond*. B. 276, 37-49.

78. Casjens S, Adams MB, Hall C, King J. 1985. Autogenous Modulation of Bacteriophage 123:174–179.

79. Tatnall M, King J. 1981. Purification of the Coat and Scaffolding Procapsids of Bacteriophage Proteins from 547:529–547.

80. Prevelige PE, Thomas D, King J. 1988. Scaffolding protein regulates the polymerization of P22 coat subunits into icosahedral shells in vitro. J Mol Biol 202:743–757.

81. Johnson JE. 1996. Functional implications of protein-protein interactions in icosahedral viruses. Proc Natl Acad Sci 93 :27–33.

82. Earnshaw W, Casjens S, Harrison SC. 1976. Assembly of the head of bacteriophage P22: X-ray diffraction from heads, proheads and related structures. J Mol Biol 104:387–410.

83. Capen CM, Teschke CM. 2000. Folding defects caused by single amino acid substitutions in a subunit are not alleviated by assembly. Biochemistry 39:1142–1151.

84. Galisteo ML, King J. 1993. Conformational transformations in the protein lattice of phage P22 procapsids. Biophys J 65:227–35.

85. Lucon J, Qazi S, Uchida M, Bedwell GJ, Lafrance B, Jr PEP, Douglas T. 2012. polymerization with high-density cargo loading. Nature Chem 4:781–788.

86. Parent KN, Khayat R, Tu LH, Suhanovsky MM, Cortines JR, Teschke CM, Johnson JE, Baker TS. 2010. P22 coat protein structures reveal a novel mechanism for capsid maturation: stability without auxiliary proteins or chemical crosslinks. Structure 18:390–401.

87. Teschke CM, McGough A, Thuman-Commike P a. 2003. Penton release from P22 heat-expanded capsids suggests importance of stabilizing penton-hexon interactions during capsid maturation. Biophys J 84:2585–92.

88. Speir J a, Munshi S, Wang G, Baker TS, Johnson JE. 1995. Structures of the native and swollen forms of cowpea chlorotic mottle virus determined by X-ray crystallography and cryo-electron microscopy. Structure 3:63–78.

89. Hendrix RW, Johnson JE. 2012. Viral Molecular Machines 726:351–363.

90. Wikoff WR, Liljas L, Duda RL, Tsuruta H, Hendrix RW, Johnson JE. 2000. Topologically linked protein rings in the bacteriophage HK97 capsid. Science 289:2129–2133.

91. Duda RL. 1998. Protein chainmail: Catenated protein in viral capsids. Cell 94:55–60.

92. Roos WH, Gertsman I, May ER, Brooks CL, Johnson JE, Wuite GJL. 2012. Mechanics of bacteriophage maturation. Proc Natl Acad Sci 109:2342–2347.

93. Rayaprolu V, Kruse S, Kant R, Venkatakrishnan B, Movahed N, Brooke D, Lins B, Bennett A, Potter T, McKenna R, Agbandje-McKenna M, Bothner B. 2013. Comparative Analysis of Adeno Associated Virus Capsid Stability and Dynamics. J Virol.

94. Kuznetsov YG, McPherson A. 2011. Atomic force microscopy in imaging of viruses and virus-infected cells. Microbiol Mol Biol Rev 75:268–285.

95. Roos WH, Ivanovska IL, Evilevitch a., Wuite GJL. 2007. Viral capsids: Mechanical characteristics, genome packaging and delivery mechanisms. Cell Mol Life Sci 64:1484–1497.

96. Tuma R, Prevelige PE, Thomas GJ. 1998. Mechanism of capsid maturation in a double-stranded DNA virus. Proc Natl Acad Sci U S A 95:9885–90.

97. Wang L, Lane LC, Smith DL. 2001. Detecting structural changes in viral capsids by hydrogen exchange and mass spectrometry. Protein Sci 10:1234–1243.

98. Kang S, Poliakov A, Sexton J, Renfrow MB, Jr PEP. 2008. Probing Conserved Helical Modules of Portal Complexes by Mass Spectrometry-based Hydrogen / Deuterium Exchange 772–784.

99. Kang S, Prevelige PE. 2005. Domain study of bacteriophage p22 coat protein and characterization of the capsid lattice transformation by hydrogen/deuterium exchange. J Mol Biol 347:935–48.

100. Hernando-Pérez M, Lambert S, Nakatani-Webster E, Catalano CE, de Pablo PJ. 2014. Cementing proteins provide extra mechanical stabilization to viral cages. Nat Commun 5:4520.

101. Kelley LA, Mezulis S, Yates CM, Wass MN, Sternberg MJE. 2015. The Phyre2 web portal for protein modeling, prediction and analysis. Nat Protoc 10:845–858.

102. Xu D, Zhang Y. 2011. Improving the physical realism and structural accuracy of protein models by a two-step atomic-level energy minimization. Biophys J 101:2525–2534.

103. Pettersen EF, Goddard TD, Huang CC, Couch GS, Greenblatt DM, Meng EC, Ferrin TE. 2004. UCSF Chimera - A visualization system for exploratory research and analysis. J Comput Chem 25:1605–1612.

104. Niesen FH, Berglund H, Vedadi M. 2007. The use of differential scanning fluorimetry to detect ligand interactions that promote protein stability. Nat Protoc

2:2212–21.

105. Rayaprolu V, Kruse S, Kant R, Venkatakrishnan B, Movahed N, Brooke D, Lins B, Bennett A, Potter T, McKenna R, Agbandje-McKenna M, Bothner B. 2013. Comparative Analysis of Adeno Associated Virus Capsid Stability and Dynamics. J Virol.

106. Zhang Z, Greene B, Thuman-Commike P a, Jakana J, Prevelige PE, King J, Chiu W. 2000. Visualization of the maturation transition in bacteriophage P22 by electron cryomicroscopy. J Mol Biol 297:615–26.

107. Zandi R, Reguera D. 2005. Mechanical properties of viral capsids. Phys Rev E - Stat Nonlinear, Soft Matter Phys 72.

108. Canady M a, Tihova M, Hanzlik TN, Johnson JE, Yeager M. 2000. Large conformational changes in the maturation of a simple RNA virus, nudaurelia capensis omega virus (NomegaV). J Mol Biol 299:573–584.

109. RF G, CN P. 1974. Urea and guanidine hydrochloride denaturation curves. J Biol Chem 249:5388–5393.

110. Pace CN, Vanderburg KE. 1979. Determining globular protein stability: guanidine hydrochloride denaturation of myoglobin. Biochemistry 18:288–292.

111. Monera OD, Kay CM, Hodges RS. 1994. Protein denaturation with guanidine hydrochloride or urea provides a different estimate of stability depending on the contributions of electrostatic interactions. Protein Sci 3:1984–1991.

112. England JL, Haran G. 2011. Role of solvation effects in protein denaturation: from thermodynamics to single molecules and back. Annu Rev Phys Chem 62:257–277.

113. Tuma R, Prevelige PE, Thomas GJ. 1998. Mechanism of capsid maturation in a double-stranded DNA virus. Proc Natl Acad Sci U S A 95:9885–9890.

114. Asghar A, Buzari B, Pavelkic V, Gopcevic K, Petkovic M, Bordbar A. 2013. Thermochimica Acta Thermal denaturation of pepsin at acidic media : Using DSC , MALDI-TOF MS and PAGE techniques. Thermochim Acta 568:165–170.

115. Lanman J, Tuma R, Prevelige PE. 1999. Identification and characterization of the domain structure of bacteriophage P22 coat protein. Biochemistry 38:14614–23.

116. Chen D-H, Baker ML, Hryc CF, DiMaio F, Jakana J, Wu W, Dougherty M, Haase-Pettingell C, Schmid MF, Jiang W, Baker D, King J a, Chiu W. 2011. Structural basis for scaffolding-mediated assembly and maturation of a dsDNA virus. Proc Natl Acad Sci U S A 108:1355–1360.

117. Mateu MG. 2012. Mechanical properties of viruses analyzed by atomic force microscopy: A virological perspective. Virus Res 168:1–22.

118. Llauro A, Guerra P, Irigoyen N, Rodriguez JF, Verdaguer N, De Pablo PJ. 2014. Mechanical stability and reversible fracture of vault particles. Biophys J 106:687–695.

119. Lazarus A, Florijn HCB, Reis PM. 2012. Geometry-induced rigidity in nonspherical pressurized elastic shells. Phys Rev Lett 109:1–5.

120. Bai Y, Milne JS, Mayne L, Englander SW. 1993. Primary structure effects on peptide group hydrogen exchange. Proteins 17:75–86.

121. Nguyen TT, Bruinsma RF, Gelbart WM. 2005. Elasticity theory and shape transitions of viral shells. Phys Rev E - Stat Nonlinear, Soft Matter Phys 72:1–19.

122. Tuma R, Tsuruta H, Benevides JM, Prevelige PE, Thomas GJ. 2001. Characterization of subunit structural changes accompanying assembly of the bacteriophage P22 procapsid. Biochemistry 40:665–74.

123. Reddy VS, Giesing H a, Morton RT, Kumar a, Post CB, Brooks CL, Johnson JE. 1998. Energetics of quasiequivalence: computational analysis of protein-protein interactions in icosahedral viruses. Biophys J 74:546–558.

124. Carrillo-Tripp M, Shepherd CM, Borelli IA, Venkataraman S, Lander G, Natarajan P, Johnson JE, Brooks CL, Reddy VS. 2009. VIPERdb2: an enhanced and web API enabled relational database for structural virology. Nucleic Acids Res 37:D436–42.

125. Lanman J, Tuma R, Prevelige PE. 1999. Identification and characterization of the domain structure of bacteriophage P22 coat protein. Biochemistry 38:14614–23.

126. Schwartz R, Shor PW, Prevelige PE, Berger B. 1998. Local Rules Simulation of the Kinetics of Virus Capsid Self-Assembly. Biophys J 75:2626–2636.

127. Moerman PG, van der Schoot P, Kegel WK. 2016. Kinetics versus Thermodynamics in Virus Capsid Polymorphism. J Phys Chem B acs.jpcb.6b01953.

128. Parent KN, Doyle SM, Anderson E, Teschke CM. 2005. Electrostatic interactions govern both nucleation and elongation during phage P22 procapsid assembly. Virology 340:33–45.

129. Parker MH, Stafford WF, Prevelige PE. 1997. Bacteriophage P22 scaffolding protein forms oligomers in solution. J Mol Biol 268:655–65.

130. Hendrix RW. 1999. Evolution: The long evolutionary reach of viruses. Curr Biol 9:914–917.

131. Veesler D, Johnson JE. 2012. Virus maturation. Annu Rev Biophys 41:473–96.

132. Zlotnick A. 2005. Theoretical aspects of virus capsid assembly. J Mol Recognit 18:479–490.

133. Tuma R, Tsuruta H, French KH, Prevelige PE. 2008. Detection of intermediates and kinetic control during assembly of bacteriophage P22 procapsid. J Mol Biol 381:1395–406.

134. Bothner B, Taylor D, Jun B, Lee KK, Siuzdak G, Schultz CP, Schlutz CP, Johnson JE. 2005. Maturation of a tetravirus capsid alters the dynamic properties and creates a metastable complex. Virology 334:17–27.

135. Galisteo ML, King J. 1993. Conformational transformations in the protein lattice of phage P22 procapsids. Biophys J 65:227–35.

136. Wikoff WR, Liljas L, Duda RL, Tsuruta H, Hendrix RW, Johnson JE. 2000. Topologically linked protein rings in the bacteriophage HK97 capsid. Science 289:2129–2133.

137. Duda RL. 1998. Protein chainmail: Catenated protein in viral capsids. Cell 94:55–60.

138. Gertsman I, Gan L, Guttman M, Lee K, Speir JA, Duda RL, Hendrix RW, Komives EA, Johnson JE. 2009. An unexpected twist in viral capsid maturation. Nature 458:646–650.

139. Galisteo ML, King J. 1993. Conformational transformations in the protein lattice of phage P22 procapsids. Biophys J 65:227–35.

140. Parent KN, Khayat R, Tu LH, Suhanovsky MM, Cortines JR, Teschke CM, Johnson JE, Baker TS. 2010. P22 coat protein structures reveal a novel mechanism for capsid maturation: stability without auxiliary proteins or chemical crosslinks. Structure 18:390–401.

141. Tuma R, Prevelige PE, Thomas GJ. 1998. Mechanism of capsid maturation in a double-stranded DNA virus. Proc Natl Acad Sci U S A 95:9885–9890.

142. Zlotnick A. 2003. Are weak protein-protein interactions the general rule in capsid assembly? Virology 315:269–274.

143. Uchida M, Douglas T. 2013. Unravelling capsid transformations. Nat Chem 5:444–445.

144. Roos WH, Ivanovska IL, Evilevitch a., Wuite GJL. 2007. Viral capsids: Mechanical characteristics, genome packaging and delivery mechanisms. Cell Mol Life Sci

64:1484–1497.

145. Kuznetsov YG, McPherson A. 2011. Atomic force microscopy in imaging of viruses and virus-infected cells. Microbiol Mol Biol Rev 75:268–285.

146. Roos WH, Gertsman I, May ER, Brooks CL, Johnson JE, Wuite GJL. 2012. Mechanics of bacteriophage maturation. Proc Natl Acad Sci 109:2342–2347.

147. Kuznetsov YG, Gurnon JR, Van Etten JL, McPherson A. 2005. Atomic force microscopy investigation of a chlorella virus, PBCV-1. J Struct Biol 149:256–263.

148. Kuznetsov YG, McPherson A. 2011. Atomic Force Microscopy in Imaging of Viruses and Virus-Infected Cells. Microbiol Mol Biol Rev 75:268–285.

149. Michel JP, Ivanovska IL, Gibbons MM, Klug WS, Knobler CM, Wuite GJL, Schmidt CF. 2006. Nanoindentation studies of full and empty viral capsids and the effects of capsid protein mutations on elasticity and strength. Proc Natl Acad Sci U S A 103:6184–6189.

150. Earnshaw W, Casjens S, Harrison SC. 1976. Assembly of the head of bacteriophage P22: X-ray diffraction from heads, proheads and related structures. J Mol Biol 104:387–410.

151. Casjens S, Adams MB, Hall C, King J. 1985. Autogenous Modulation of Bacteriophage 123:174–179.

152. Parker MH, Casjens S, Prevelige PE. 1998. Functional domains of bacteriophage P22 scaffolding protein. J Mol Biol 281:69–79.

153. Parker MH, Prevelige PE. 1998. Electrostatic interactions drive scaffolding/coat protein binding and procapsid maturation in bacteriophage P22. Virology 250:337–49.

154. Prevelige PE, Thomas D, King J. 1988. Scaffolding protein regulates the polymerization of P22 coat subunits into icosahedral shells in vitro. J Mol Biol 202:743–57.

155. Teschke CM, McGough A, Thuman-Commike P a. 2003. Penton release from P22 heat-expanded capsids suggests importance of stabilizing penton-hexon interactions during capsid maturation. Biophys J 84:2585–92.

156. Lucon J, Qazi S, Uchida M, Bedwell GJ, Lafrance B, Jr PEP, Douglas T. 2012. polymerization with high-density cargo loading. Nat. Chem 4:781–788.

157. Dixon MC. 2008. Quartz crystal microbalance with dissipation monitoring: enabling real-time characterization of biological materials and their interactions. J Biomol

Tech 19:151–8.

158. Rodahl M, Höök F, Krozer A, Brzezinski P, Kasemo B. 1995. Quartz crystal microbalance setup for frequency and Q-factor measurements in gaseous and liquid environments. Rev Sci Instrum 66:3924–3930.

159. Arnau A. 2008. A Review of Interface Electronic Systems for AT-cut Quartz Crystal Microbalance Applications in Liquids. Sensors 8:370–411.

160. Rodahl M, Kasemo B. 1996. A simple setup to simultaneously measure the resonant frequency and the absolute dissipation factor of a quartz crystal microbalance. Rev Sci Instrum 67:3238–3241.

161. Bradshaw BL. 2000. Understanding piezoelectric quartz crystals, www.rfdesign.com, August.

162. Dutta AK, Belfort G. 2007. Adsorbed gels versus brushes: viscoelastic differences. Langmuir 23:3088–94.

163. Voinova M V, Rodahl M, Jonson M, Kasemo B. Viscoelastic Acoustic Response of Layered Polymer Films at Fluid-Solid Interfaces : Viscoelastic Acoustic Response of Layered Polymer Films at Fluid-Solid Interfaces : Continuum Mechanics Approach. Applied Physics report, 97-34.

164. Wang S-H, Shen C-Y, Weng T-C, Lin P-H, Yang J-J, Chen I-F, Kuo S-M, Chang S-J, Tu Y-K, Kao Y-H, Hung C-H. 2010. Detection of cartilage oligomeric matrix protein using a quartz crystal microbalance. Sensors (Basel) 10:11633–43.

165. Rayaprolu V, Manning BM, Douglas T, Bothner B. 2010. Virus particles as active nanomaterials that can rapidly change their viscoelastic properties in response to dilute solutions. Soft Matter 6:5286.

166. Liu H, Qu C, Johnson JE, Case D a. 2003. Pseudo-atomic models of swollen CCMV from cryo-electron microscopy data. J Struct Biol 142:356–363.

167. Voinova M V, Rodahl M, Jonson M, Kasemo B. 1999. Viscoelastic acoustic response of layered polymer films at fluid-solid interfaces: continuum mechanics approach. Phys Scr 59:391–396.

168. Bandey HL, Robert Hillman a., Brown MJ, Martin SJ. 1997. Viscoelastic characterization of electroactive polymer films at the electrode/solution interface. Faraday Discuss 107:105–121.

169. Johannsmann D. 1999. Viscoelastic analysis of organic thin films on quartz resonators. Macromol Chem Phys 516:501–516.

170. Larsson C, Rodahl M, Höök F. 2003. Characterization of DNA immobilization and subsequent hybridization on a 2D arrangement of streptavidin on a biotin-modified lipid bilayer supported on SiO2. Anal Chem 75:5080–5087.

171. Höök F, Kasemo B, Nylander T, Fant C, Sott K, Elwing H. 2001. Variations in coupled water, viscoelastic properties, and film thickness of a Mefp-1 protein film during adsorption and cross-linking: a quartz crystal microbalance with dissipation monitoring, ellipsometry, and surface plasmon resonance study. Anal Chem 73:5796–804.

172. Zandi R, Reguera D. 2005. Mechanical properties of viral capsids. Phys Rev E - Stat Nonlinear, Soft Matter Phys 72.

173. Liu SX, Kim J-T. 2009. Application of Kevin–Voigt Model in Quantifying Whey Protein Adsorption on Polyethersulfone Using QCM-D. J Assoc Lab Autom 14:213–220.

174. Malmström J, Agheli H, Kingshott P, Sutherland DS. 2007. Viscoelastic modeling of highly hydrated laminin layers at homogeneous and nanostructured surfaces: Quantification of protein layer properties using QCM-D and SPR. Langmuir 23:9760–9768.

175. Binazadeh M, Zeng H, Unsworth LD. 2013. Effect of peptide secondary structure on adsorption and adsorbed film properties. Acta Biomater 9:6403–13.

176. Chen D-H, Baker ML, Hryc CF, DiMaio F, Jakana J, Wu W, Dougherty M, Haase-Pettingell C, Schmid MF, Jiang W, Baker D, King J a, Chiu W. 2011. Structural basis for scaffolding-mediated assembly and maturation of a dsDNA virus. Proc Natl Acad Sci U S A 108:1355–1360.

177. O'Neil A, Reichhardt C, Johnson B, Prevelige PE, Douglas T. 2011. Genetically programmed in vivo packaging of protein cargo and its controlled release from bacteriophage P22. Angew Chemie - Int Ed 50:7425–7428.

178. Patterson D, Edwards E, Douglas T. 2015. Hybrid Nanoreactors: Coupling Enzymes and Small-Molecule Catalysts within Virus-Like Particles. Isr J Chem 55:96–101.

179. Kang S, Uchida M, O'Neil A, Li R, Prevelige PE, Douglas T. 2010. Implementation of p22 viral capsids as nanoplatforms. Biomacromolecules 11:2804–9.

180. Lubarsky G V., Davidson MR, Bradley RH. 2007. Hydration-dehydration of adsorbed protein films studied by AFM and QCM-D. Biosens Bioelectron 22:1275–1281.

181. Usselman RJ, Qazi S, Aggarwal P, Eaton SS, Eaton GR, Russek S, Douglas T. 2015. Gadolinium-Loaded Viral Capsids as Magnetic Resonance Imaging Contrast

Agents. Appl Magn Reson 46:349–355.

182. Bedwell GJ, Zhou Z, Uchida M, Douglas T, Gupta A, Prevelige PE. 2015. Selective Biotemplated Synthesis of TiO2 inside a Protein Cage. Biomacromolecules 16:214–218.

183. Patterson DP, Schwarz B, Waters RS, Gedeon T, Douglas T. 2014. Encapsulation of an enzyme cascade within the bacteriophage P22 virus-like particle. ACS Chem Biol 9:359–365.

184. Kale A, Bao Y, Zhou Z, Prevelige PE, Gupta A. 2013. Directed self-assembly of CdS quantum dots on bacteriophage P22 coat protein templates. Nanotechnology 24:045603.

185. Buller RM, Rose JA. 1978. Characterization of adenovirus-associated virus-induced polypeptides in KB cells. J Virol 25:331–8.

186. Rose J a, Maizel J V, Inman JK, Shatkin a J. 1971. Structural proteins of adenovirus-associated viruses. J Virol 8:766–770.

187. Sonntag F, Bleker S, Leuchs B, Fischer R, Kleinschmidt JA. 2006. Adeno-associated virus type 2 capsids with externalized VP1/VP2 trafficking domains are generated prior to passage through the cytoplasm and are maintained until uncoating occurs in the nucleus. J Virol 80:11040–54.

188. Hoque M, Ishizu K, Matsumoto A, Han SI, Arisaka F, Takayama M, Suzuki K, Kato K, Kanda T, Watanabe H, Handa H. 1999. Nuclear transport of the major capsid protein is essential for adeno-associated virus capsid formation. J Virol 73:7912–5.

189. Coura R dos S, Nardi NB. 2008. A role for adeno-associated viral vectors in gene therapy. Genet Mol Biol 31:1–11.

190. Pugh EN, Ph D, Mingozzi F, Bennicelli J, Banfi S, Marshall KA, Testa F, Arruda VR, Konkle B, Stone E, Sun J, Jacobs J, Osso LD, Hertle R, Ma J, Redmond TM, Zhu X, Hauck B, Zelenaia O, Volpe NJ, Mcdonnell JW, Auricchio A, High KA, Bennett J. 2008. Safety and Efficacy of Gene Transfer for Leber's Congenital Amaurosis.

191. Daya S, Berns KI. 2008. Gene therapy using adeno-associated virus vectors. Clin Microbiol Rev 21:583–93.

192. Samulski RJ, Muzyczka N. 2014. AAV-Mediated Gene Therapy for Research and Therapeutic Purposes. Annu Rev Virol 1:427–451.

193. Daya S, Berns KI. 2008. Gene therapy using adeno-associated virus vectors. Clin Microbiol Rev 21:583–593.

194. Li C, Bowles DE, van Dyke T, Samulski RJ. 2005. Adeno-associated virus vectors: potential applications for cancer gene therapy. Cancer Gene Ther 12:913–25.

195. Summerford C, Samulski RJ. 1998. Membrane-associated heparan sulfate proteoglycan is a receptor for adeno-associated virus type 2 virions. J Virol 72:1438–1445.

196. Kaludov N, Brown KE, Walters RW, Chiorini JA, Kaludov N, Brown KE, Walters RW, Zabner J. 2001. and AAV5 Both Require Sialic Acid Binding for Hemagglutination and Efficient Transduction but Differ in Sialic Acid Linkage Specificity Adeno-Associated Virus Serotype 4 (AAV4) and AAV5 Both Require Sialic Acid Binding for Hemagglutination and Efficient 4:6884–6893.

197. Walters RW, Yi SM, Keshavjee S, Brown KE, Welsh MJ, Chiorini J a, Zabner J. 2001. Binding of adeno-associated virus type 5 to 2,3-linked sialic acid is required for gene transfer. J Biol Chem 276:20610–6.

198. Seisenberger G, Ried MU, Endreß T, Büning H, Hallek M, Bräuchle Ch. 2001. Real-Time Single-Molecule Imaging of the Infection Pathway of an Adeno-Associated Virus. Science (80-) 294:1929–1933.

199. Bartlett JS, Wilcher R, Samulski RJ. 2000. Infectious entry pathway of adeno-associated virus and adeno-associated virus vectors. J Virol 74:2777–2785.

200. Hansen J, Qing K, Srivastava A. 2001. Adeno-associated virus type 2-mediated gene transfer: altered endocytic processing enhances transduction efficiency in murine fibroblasts. J Virol 75:4080–90.

201. Duan D, Yue Y, Yan Z, Yang J, Engelhardt JF. 2000. Endosomal processing limits gene transfer to polarized airway epithelia by adeno-associated virus. J Clin Invest 105:1573–1587.

202. Seisenberger G, Ried MU, Endress T, Büning H, Hallek M, Bräuchle C. 2001. Real-time single-molecule imaging of the infection pathway of an adeno-associated virus. Science 294:1929–1932.

203. Sonntag F, Bleker S, Leuchs B, Fischer R, Kleinschmidt J a. 2006. Adeno-associated virus type 2 capsids with externalized VP1/VP2 trafficking domains are generated prior to passage through the cytoplasm and are maintained until uncoating occurs in the nucleus. J Virol 80:11040–54.

204. Suikkanen S, Antila M, Jaatinen A, Vihinen-Ranta M, Vuento M. 2003. Release of canine parvovirus from endocytic vesicles. Virology 316:267–280.

205. Farr G a, Zhang L, Tattersall P. 2005. Parvoviral virions deploy a capsid-tethered lipolytic enzyme to breach the endosomal membrane during cell entry. Proc Natl

Acad Sci U S A 102:17148–17153.

206. Canaan S, Z??dori Z, Ghomashchi F, Bollinger J, Sadilek M, Moreau ME, Tijssen P, Gelb MH. 2004. Interfacial Enzymology of Parvovirus Phospholipases A2. J Biol Chem 279:14502–14508.

207. Van Vliet K, Blouin V, Agbandje-McKenna M, Snyder RO. 2006. Proteolytic Mapping of the Adeno-associated Virus Capsid. Mol Ther 14:809–821.

208. Popa-Wagner R, Porwal M, Kann M, Reuss M, Weimer M, Florin L, Kleinschmidt J a. 2012. Impact of VP1-Specific Protein Sequence Motifs on Adeno-Associated Virus Type 2 Intracellular Trafficking and Nuclear Entry. J Virol 86:9163–9174.

209. Bleker S, Pawlita M, Kleinschmidt JA. 2006. Impact of Capsid Conformation and Rep-Capsid Interactions on Adeno-Associated Virus Type 2 Genome Packaging Impact of Capsid Conformation and Rep-Capsid Interactions on Adeno-Associated Virus Type 2 Genome Packaging. J Virol 80:810–820.

210. Kronenberg S, Böttcher B, Der CW Von, Bleker S, Kleinschmidt J a, Bo B, Lieth CW Von Der. 2005. A Conformational Change in the Adeno-Associated Virus Type 2 Capsid Leads to the Exposure of Hidden VP1 N Termini A Conformational Change in the Adeno-Associated Virus Type 2 Capsid Leads to the Exposure of Hidden VP1 N Termini 79:5296–5303.

211. Carter BJ, Rose JA. 1972. Adenovirus-Associated Virus Multiplication 10:9–16.

212. Johnson FB, Ozer HL, Hoggan MD. 1971. Structural proteins of adenovirus-associated virus type 3. J Virol 8:860–63.

213. Becerra SP, Koczot F, Fabisch P, Rose J a. 1988. Synthesis of adeno-associated virus structural proteins requires both alternative mRNA splicing and alternative initiations from a single transcript. J Virol 62:2745–2754.

214. Cassinotti P, Weitzand M, Tratschin JD. 1988. Organization of the adeno-associated virus (AAV) capsid gene: Mapping of a minor spliced mRNA coding for virus capsid protein. Virology 167:176–184.

215. Panteghini M, Pagani F, Bonora R. 1993 Clinical and Analytical Evaluation of a Continuous Enzymatic Method for Measuring Pancreatic Lipase Activity. Clin Chem 39/2, 304-308

216. Jette JF, Ziomek E. 1994. Determination of lipase activity y a Rhodamine-Triglycerid-Agarose Assay. Anal Biochem 219, 256-260

217. Hendrickson HS. 1994. Fluorescence-based assays of lipases, phospholipases, and other lipolytic enzymes. Anal Biochem.

218. Negre-Salvayre A, Abouakil N, Lombardo D, Salvayre R. 1990. Hydrolysis of fluorescent pyrene-acyl esters by human pancreatic carboxylic ester hydrolase and bile salt-stimulated lipase. Lipids 25:428–434.

219. Negre-Salvayre A, Dagan A, Gatt S, Salvayre R. 1993. Use of pyrenemethyl laurate for fluorescence-based determination of lipase activity in intact living lymphoblastoid cells and for the diagnosis of acid lipase deficiency. Biochem J 294 (Pt 3:885–891.

220. Wilton DC. 1991. A continuous fluorescence-displacement assay for triacylglycerol lipase and phospholipase C that also allows the measurement of acylglycerols. Biochem J 276 (Pt 1:129–133.

221. Briquet-Laugier V, Ben-Zeev O, Doolittle MH. 1999. Determining lipoprotein lipase and hepatic lipase activity using radiolabeled substrates. Methods Mol Biol 109:81–94.

222. Hao G, Yang L, Mazsaroff I, Lin M. 2007. Quantitative Determination of Lipase Activity by Liquid Chromatography-Mass Spectrometry. J Am Soc Mass Spectrom 18:1579–1581.

223. Kim J, Jung J, Reyes JL, Kim Y, Kim S, Chung K, Kim JA, Lee M, Lee Y, Kim VN, Park C. 2006. NIH Public Access 42:84–94.

224. DiMattia M, Govindasamy L, Levy HC, Gurda-Whitaker B, Kalina A, Kohlbrenner E, Chiorini JA, McKenna R, Muzyczka N, Zolotukhin S, Agbandje-McKenna M. 2005. Production, purification, crystallization and preliminary X-ray structural studies of adeno-associated virus serotype 5. Acta Crystallogr Sect F Struct Biol Cryst Commun 61:917–921.

225. Lane MD, Nam HJ, Padron E, Gurda-Whitaker B, Kohlbrenner E, Aslanidi G, Byrne B, McKenna R, Muzyczka N, Zolotukhin S, Agbandje-McKenna M. 2005. Production, purification, crystallization and preliminary X-ray analysis of adeno-associated virus serotype 8. Acta Crystallogr Sect F Struct Biol Cryst Commun 61:558–561.

226. Kaludov N, Padron E, Govindasamy L, McKenna R, Chiorini J a, Agbandje-McKenna M. 2003. Production, purification and preliminary X-ray crystallographic studies of adeno-associated virus serotype 4. Virology 306:1–6.

227. Mah C, Fraites JTJ, Zolotukhin I, Song S, Flotte TR, Dobson J, Batich C, Byrne BJ. 2002. Improved Method of Recombinant AAV2 Delivery for Systemic Targeted Gene Therapy. Mol Ther 6:106–12.

228. Zolotukhin S, Potter M, Zolotukhin I, Sakai Y, Loiler S, Fraites TJ, Chiodo VA, Phillipsberg T, Muzyczka N, Hauswirth WW, Flotte TR, Byrne BJ, Snyder RO.

2002. Production and purification of serotype 1, 2, and 5 recombinant adeno-associated viral vectors. Methods 28:158–67.

229. Neuenschwander PF, Fiore MM, Morrisseys JH. 1993. Factor VII Autoactivation proceeds via Interaction of Distinct Protease-Cofactor and Zymogen-Cofactor Complexes. J Biol Chem 268:21489–21492.

230. Brooke D, Movahed N, Bothner B. 2015. Universal buffers for use in biochemistry and biophysical experiments. AIMS Biophys 2:336–342.

231. V??cha R, Berkowitz ML, Jungwirth P. 2009. Molecular model of a cell plasma membrane with an asymmetric multicomponent composition: Water permeation and ion effects. Biophys J 96:4493–4501.

232. Andoh Y, Okazaki S, Ueoka R. 2013. Molecular dynamics study of lipid bilayers modeling the plasma membranes of normal murine thymocytes and leukemic GRSL cells. Biochim Biophys Acta - Biomembr 1828:1259–1270.

233. Wu P, Xiao W, Conlon T, Hughes J, Agbandje-McKenna M, Ferkol T, Flotte T, Muzyczka N. 2000. Mutational analysis of the adeno-associated virus type 2 (AAV2) capsid gene and construction of AAV2 vectors with altered tropism. J Virol 74:8635–8647.

234. Rayaprolu V, Kruse S, Kant R, Venkatakrishnan B, Movahed N, Brooke D, Lins B, Bennett A, Potter T, McKenna R, Agbandje-McKenna M, Bothner B. 2013. Comparative Analysis of Adeno Associated Virus Capsid Stability and Dynamics. J Virol.

235. Douar A, Poulard K, Stockholm D, Danos O. 2001. Intracellular Trafficking of Adeno-Associated Virus Vectors : Routing to the Late Endosomal Compartment and Proteasome Degradation Intracellular Trafficking of Adeno-Associated Virus Vectors : Routing to the Late Endosomal Compartment and Proteasome Degra. Society 75:1824–1833.

236. Xiao P-J, Samulski RJ. 2012. Cytoplasmic trafficking, endosomal escape, and perinuclear accumulation of adeno-associated virus type 2 particles are facilitated by microtubule network. J Virol 86:10462–73.

237. Li C, He Y, Nicolson S, Hirsch M, Weinberg MS, Zhang P, Kafri T, Samulski RJ. 2013. Adeno-associated virus capsid antigen presentation is dependent on endosomal escape. J Clin Invest 123:1390–1401.

238. Lux K, Goerlitz N, Schlemminger S, Goldnau D, Endell J, Leike K, Kofler M, Finke S, Hallek M, Perabo L, Kofler DM. 2005. Green Fluorescent Protein-Tagged Adeno-Associated Virus Particles Allow the Study of Cytosolic and Nuclear Trafficking Green Fluorescent Protein-Tagged Adeno-Associated Virus Particles

Allow the Study of Cytosolic and Nuclear Trafficking †. Society 79:11776–11787.

239. Gao G, Vandenberghe LH, Alvira MR, Lu Y, Calcedo R, Zhou X, Wilson JM. 2004. Clades of Adeno-associated viruses are widely disseminated in human tissues. J Virol 78:6381–8.

240. Zincarelli C, Soltys S, Rengo G, Rabinowitz JE. 2008. Analysis of AAV serotypes 1-9 mediated gene expression and tropism in mice after systemic injection. Mol Ther 16:1073–1080.

241. Wu Z, Asokan A, Samulski RJ. 2006. Adeno-associated Virus Serotypes: Vector Toolkit for Human Gene Therapy. Mol Ther 14:316–327.

242. Asokan A, Schaffer D V, Jude Samulski R. 2012. The AAV Vector Toolkit: Poised at the Clinical Crossroads. Mol Ther 20:699–708.

243. Wu P, Phillips MI, Bui J, Terwilliger EF. 1998. Adeno-associated virus vector-mediated transgene integration into neurons and other nondividing cell targets. J Virol 72:5919–5926.

244. Fisher KJ, Jooss K, Alston J, Yang Y, Haecker SE, High K, Pathak R, Raper SE, Wilson JM. 1997. Recombinant adeno-associated virus for muscle directed gene therapy. Nat Med 3:306–312.

245. Xiao X, Li J, Samulski RJ. 1996. Efficient long-term gene transfer into muscle tissue of immunocompetent mice by adeno-associated virus vector. J Virol 70:8098–108.

246. Castle MJ, Gershenson ZT, Giles AR, Holzbaur ELF, Wolfe JH. 2014. Adeno-associated virus serotypes 1, 8, and 9 share conserved mechanisms for anterograde and retrograde axonal transport. Hum Gene Ther 25:705–20.

247. DiMattia MA, Nam HJ, Van Vliet K, Mitchell M, Bennett A, Gurda BL, McKenna R, Olson NH, Sinkovits RS, Potter M, Byrne BJ, Aslanidi G, Zolotukhin S, Muzyczka N, Baker TS, Agbandje-McKenna M. 2012. Structural insight into the unique properties of adeno-associated virus serotype 9. J Virol 86:6947–6958.

248. Foust KD, Nurre E, Montgomery CL, Hernandez A, Chan CM, Kaspar BK, Curtis M, Kaspar BK. 2009. Intravascular AAV9 preferentially targets neonatal-neurons and adult-astrocytes in CNS. Nat Biotechnol 27:59–65.

249. Gauss GH, Benas P, Wiedenheft B, Young M, Douglas T, Lawrence CM. 2006. Structure of the DPS-like protein from Sulfolobus solfataricus reveals a bacterioferritin-like dimetal binding site within a DPS-like dodecameric assembly. Biochemistry 45:10815–27.

250. Lawson DM, Artymiuk PJ, Yewdall SJ, Smith JM, Livingstone JC, Treffry A,

Luzzago A, Levi S, Arosio P, Cesareni G. 1991. Solving the structure of human H ferritin by genetically engineering intermolecular crystal contacts. Nature 349:541–4.

251. Caspar DLD, Klug A. 1962. Physical principles in the construction of regular viruses. Cold Spring Harb Symp Quant Biol 27th:1–24.

252. Johnson JE, Speir J a. 1997. Quasi-equivalent viruses: a paradigm for protein assemblies. J Mol Biol 269:665–75.

253. Ivanovska IL, de Pablo PJ, Ibarra B, Sgalari G, MacKintosh FC, Carrascosa JL, Schmidt CF, Wuite GJL. 2004. Bacteriophage capsids: tough nanoshells with complex elastic properties. Proc Natl Acad Sci U S A 101:7600–7605.

254. Gibbons M, Klug W. 2007. Nonlinear finite-element analysis of nanoindentation of viral capsids. Phys Rev E 75:1–11.

255. Roos WH, Wuite GJL. 2009. Nanoindentation Studies Reveal Material Properties of Viruses. Adv Mater 21:1187–1192.

256. Rydell GE, Dahlin AB, Höök F, Larson G. 2009. QCM-D studies of human norovirus VLPs binding to glycosphingolipids in supported lipid bilayers reveal strain-specific characteristics. Glycobiology.

257. Rayaprolu V, Manning BM, Douglas T, Bothner B. 2010. Virus particles as active nanomaterials that can rapidly change their viscoelastic properties in response to dilute solutions. Soft Matter 6:5286.

258. da Silva AK, Kavanagh O V, Estes MK, Elimelech M. 2011. Adsorption and aggregation properties of norovirus GI and GII virus-like particles demonstrate differing responses to solution chemistry. Environ Sci Technol 45:520–6.

259. Nguyen TH, Elimelech M. 2007. Adsorption of plasmid DNA to a natural organic matter-coated silica surface: Kinetics, conformation, and reversibility. Langmuir 23:3273–3279.

260. Nguyen TH, Chen KL. 2007. Role of divalent cations in plasmid DNA adsorption to natural organic matter-coated silica surface. Environ Sci Technol 41:5370–5375.

261. Nguyen TH, Elimelech M. 2007. Plasmid DNA adsorption on silica: Kinetics and conformational changes in monovalent and divalent salts. Biomacromolecules 8:24–32.

262. Keller CA, Kasemo B. 1998. Surface specific kinetics of lipid vesicle adsorption measured with a quartz crystal microbalance. Biophys J 75:1397–1402.

263. Cho NJ, Cho SJ, Kwang HC, Glenn JS, Frank CW. 2007. Employing an amphipathic viral peptide to create a lipid bilayer on Au and TiO2. J Am Chem Soc 129:10050–10051.

264. Schofield AL, Rudd TR, Martin DS, Fernig DG, Edwards C. 2007. Real-time monitoring of the development and stability of biofilms of Streptococcus mutans using the quartz crystal microbalance with dissipation monitoring. Biosens Bioelectron 23:407–413.

265. Wittmer CR, Phelps JA, Saltzman WM, Van Tassel PR. 2007. Fibronectin terminated multilayer films: Protein adsorption and cell attachment studies. Biomaterials 28:851–860.

266. Rayaprolu V, Manning BM, Douglas T, Bothner B. 2010. Virus particles as active nanomaterials that can rapidly change their viscoelastic properties in response to dilute solutions. Soft Matter 6:5286.

267. Selzer L, Kant R, Wang JCY, Bothner B, Zlotnick A. 2015. Hepatitis B virus core protein phosphorylation sites affect capsid stability and transient exposure of the C-terminal domain. J Biol Chem 290:28584–28593.

268. Gao G, Vandenberghe LH, Alvira MR, Lu Y, Calcedo R, Zhou X, Wilson JM. 2004. Clades of Adeno-associated viruses are widely disseminated in human tissues. J Virol 78:6381–8.

269. Rayaprolu V, Kruse S, Kant R, Venkatakrishnan B, Movahed N, Brooke D, Lins B, Bennett A, Potter T, McKenna R, Agbandje-McKenna M, Bothner B. 2013. Comparative Analysis of Adeno Associated Virus Capsid Stability and Dynamics. J Virol.

270. Yolken RH, Jones-Brando L, Dunigan DD, Kannan G, Dickerson F, Severance E, Sabunciyan S, Talbot CC, Prandovszky E, Gurnon JR, Agarkova I V, Leister F, Gressitt KL, Chen O, Deuber B, Ma F, Pletnikov M V, Van Etten JL. 2014. Chlorovirus ATCV-1 is part of the human oropharyngeal virome and is associated with changes in cognitive functions in humans and mice. Proc Natl Acad Sci U S A 111:16106–11.

271. Nault J-C, Datta S, Imbeaud S, Franconi A, Mallet M, Couchy G, Letouze E, Pilati C, Verret B, Blanc J-F, Balabaud C, Calderaro J, Laurent A, Letexier M, Bioulac-Sage P, Calvo F, Zucman-Rossi J. 2015. Recurrent AAV2-related insertional mutagenesis in human hepatocellular carcinomas. Nat Genet 47:1187–1193.

272. Wang JCY, Chen C, Rayaprolu V, Mukhopadhyay S, Zlotnick A. 2015. Self-Assembly of an Alphavirus Core-like Particle Is Distinguished by Strong Intersubunit Association Energy and Structural Defects. ACS Nano 9:8898–8906.

273. Cieplak M, Robbins MO. 2013. Nanoindentation of 35 Virus Capsids in a Molecular Model: Relating Mechanical Properties to Structure. PLoS One 8.

274. 2013. Structure and Physics of Viruses: An Integrated Textbook. Springer Science & Business Media.

275. Evilevitch A, Castelnovo M, Knobler CM, Gelbart WM. 2004. Measuring the force ejecting DNA from phage 1–15.

276. Ivanovska I, Wuite G, Jönsson B, Evilevitch A. 2007. Internal DNA pressure modifies stability of WT phage. Proc Natl Acad Sci U S A 104:9603–8.

277. Vliegenthart GA, Gompper G. 2006. Mechanical deformation of spherical viruses with icosahedral symmetry. Biophys J 91:834–41.

278. Snijder J, Ivanovska IL, Baclayon M, Roos WH, Wuite GJL. 2012. Probing the impact of loading rate on the mechanical properties of viral nanoparticles. Micron 1–8.

279. Klug, A and Caspar DL. 1960. The structure of small viruses. adv virus res 7:225–235.

APPENDICES

APPENDIX A

SUPPORTING INFORMATION FOR CHAPTER 2

SUPPLEMENTARY MATERIAL

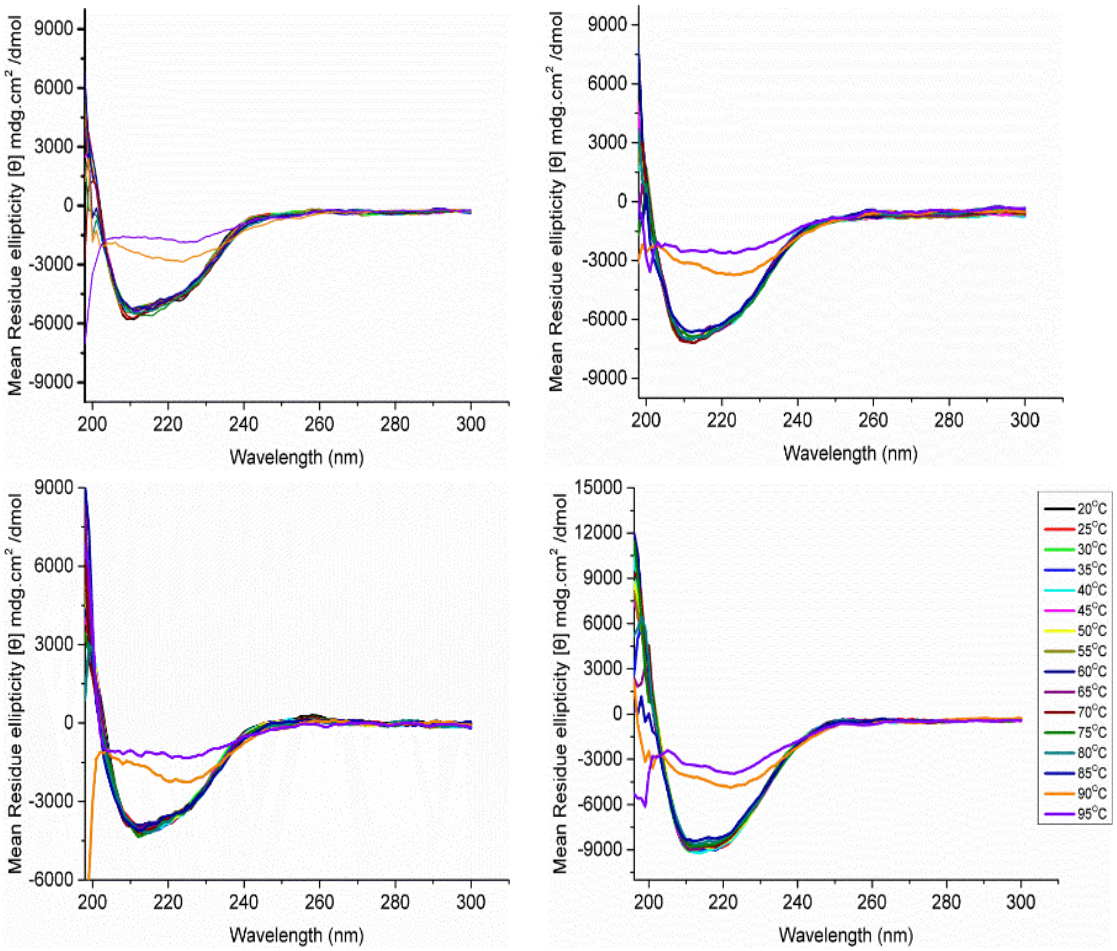


Figure S1. It shows the circular dichroic thermal scan spectra of (A) procapsid (B) empty shell (C) expanded shell (D) wiffle ball. Samples were heated in the temperature range of 25°C to 95°C. CD scans exhibited of all four morphological forms showed single structural transition until loss of secondary structure at 90°C.(x axis represents change in circular dichroic signal and y axis represents scan wavelength).

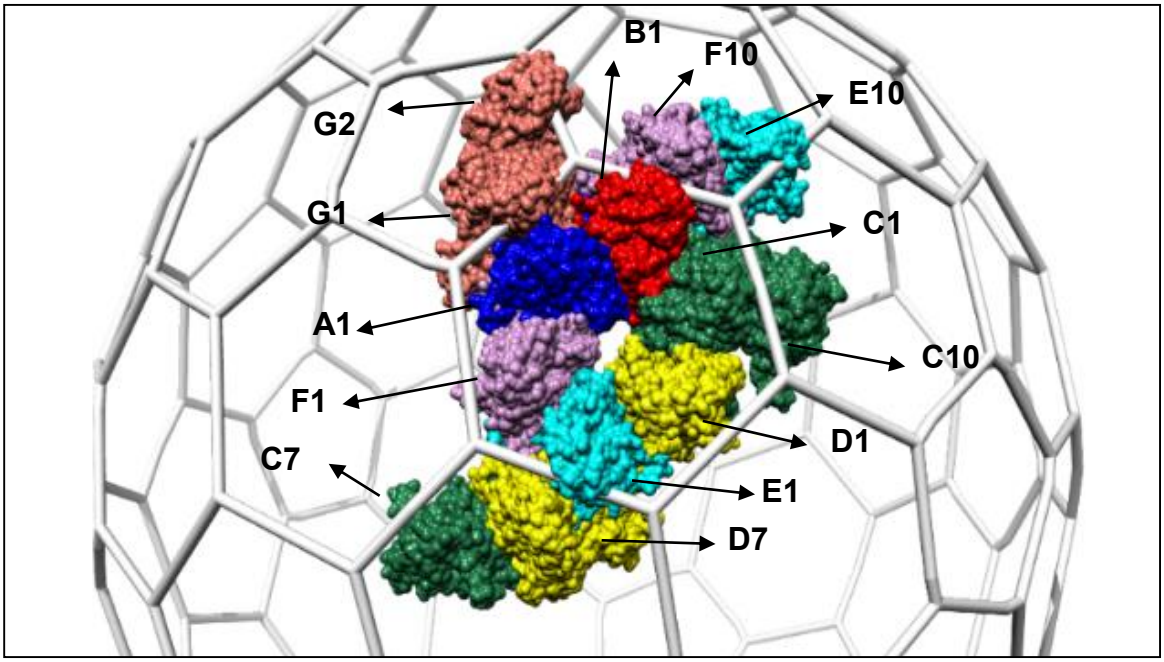


Figure S2. Labeled P22 neighboring subunits for SESA calculations

Table S1. Intersubunit buried surface area

Symmetry axis	Subunit 1	PC	EX	Subunit 2	PC	EX
I-2	C1	1148.22	332.02	C10	1151.47	310.46
I-3	D1	262.969	505.019	D7	283.142	425.298
I-5	G1	1348.18	1911.49	G2	1460.82	2298.40
Q-2	E1	997.019	188.97	D7	1179.03	172.29
	B1	1125.25	197.29	F2	1322.85	220.49
	A1	1159.67	247.074	G1	1150.9	263.945
Q-3	F1	308.59	688.05	G1	191.68	594.11
	B1	159.33	636.43	C10	158.38	509.38
	C7	223.87	648.40	E1	199.51	620.98
	A1	251.33	553.93	G2	258.45	704.04
	C1	204.06	629.46	E2	231.81	551.28
	A1	249.203	626.21	F2	205.487	703.34
Q-5	A1	1197.59	1810.48	B1	1346.28	1933.91
	E1	1333.16	2017.19	D1	1002.25	1864.95
Q-6	B1	1833.42	1934.82	C1	1846.60	1924.52
	A1	1905.57	1938.19	F1	1652.05	2048.31
	C1	1716.15	1835.94	D1	1809.69	2358.46
	E1	1476.11	2115.61	F1	1620.95	2209.07

Symmetry axis	Subunit 1	PC	WB	Subunit 2	PC	WB
I-2	C1	500.30	0	C10	559.73	0
I-3	D1	781.83	1248.94	D7	643.40	967.50
I-5	G1	708.90	0	G2	628.80	0.00
Q-2	D7	802.73	0	E1	753.14	0
	B1	653.61	0	F2	627.74	0
	A1	586.57	0	G1	579.26	0
Q-3	F1	861.99	0	G1	730.34	0
	B1	937.76	1287.87	C10	652.88	1154.79
	C7	947.33	1186.48	E1	712.97	916.62
	A1	665.97	0	G2	921.32	0
	B1	702.24	975.88	E2	807.88	1094.35
	A1	838.92	988.65	F2	650.76	951.26
Q-5	A1	375.26	1038.94	B1	312.57	919.61
	E1	174.73	1001.91	D1	234.20	1181.05
Q-6	B1	899.68	1158.21	C1	740.23	1113.13
	A1	844.40	606.82	F1	880.23	740.01
	C1	702.97	1193.29	D1	716.40	1085.57
	E1	697.71	1254.61	F1	671.58	1019.15

Table S2. Association energy calculation for P22 models

A.

		2xyy (PC)	2xyh (EX)
Interface	**Symmetry**	**Association energy (kcal/mol)**	**Association energy (kcal/mol)**
A1-F1	Q-6	-3	-20.4
E1-F1	Q-6	-11	-25.4
A1-B1	Q-6	-3.5	-25.8
C1-D1	Q-6	-4.1	-17.6
G1-G2	I-5	-8.6	-35.5
B1-C1	Q-6	-6.6	-19.5
D1-E1	Q-6	-4.8	-19.7
Sum		**-41.6**	**-163.9**

B.

		3iyi (PC)	3iyh (WB)
Interface	**Symmetry**	**Association energy (kcal/mol)**	**Association energy (kcal/mol)**
A1-F1	Q-6	-1.7	-5.7
A1-F2	Q-3	-7.2	-13.8
E1-F1	Q-6	-0.5	-17.1
B1-C1	Q-6	-4.4	-17.2
B1-E2	Q-3	-12.7	-23.6
D1-D7	I-3	-5.5	-24.1
B1-C10	Q-3	-14.2	-24.6
C7-E1	Q-3	-13.9	-28.7
Sum		**-60.1**	**-154.8**

APPENDIX B

SUPPORTING INFORMATION FOR CHAPTER 4

SUPPLEMENTARY MATERIAL

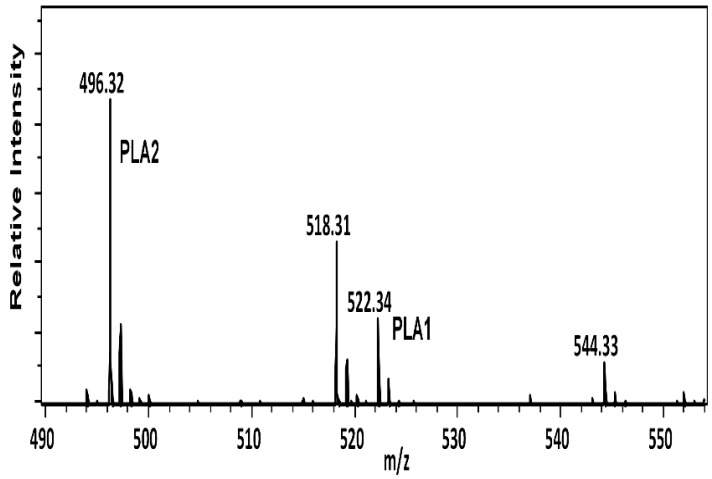


Figure S1. ESI-MS spectrum of mixed lipase products generated by heat activated AAV2 lipase domain.

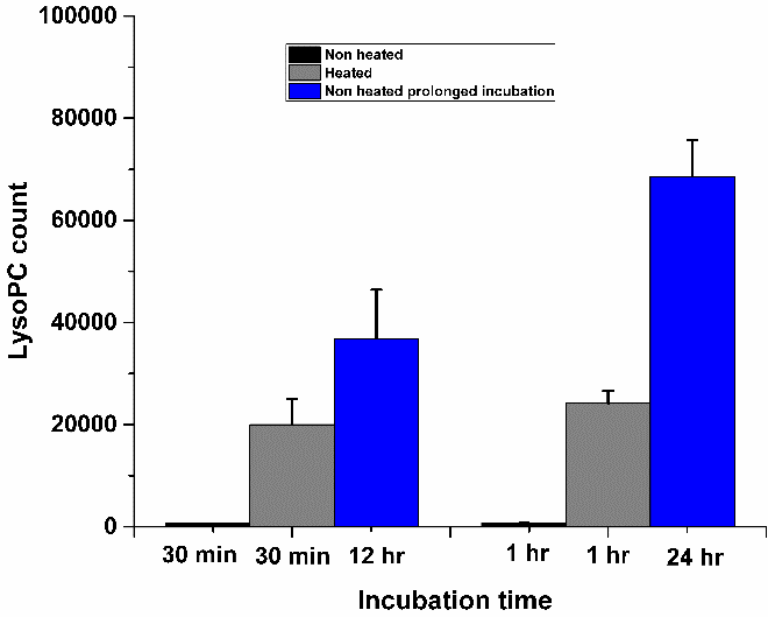


Figure S2. Comparison of lipase activity of AAV9 in non-heat, heat induced, and prolonged incubation with liposome conditions. Integrated area of lysoPC is plotted versus incubation time.

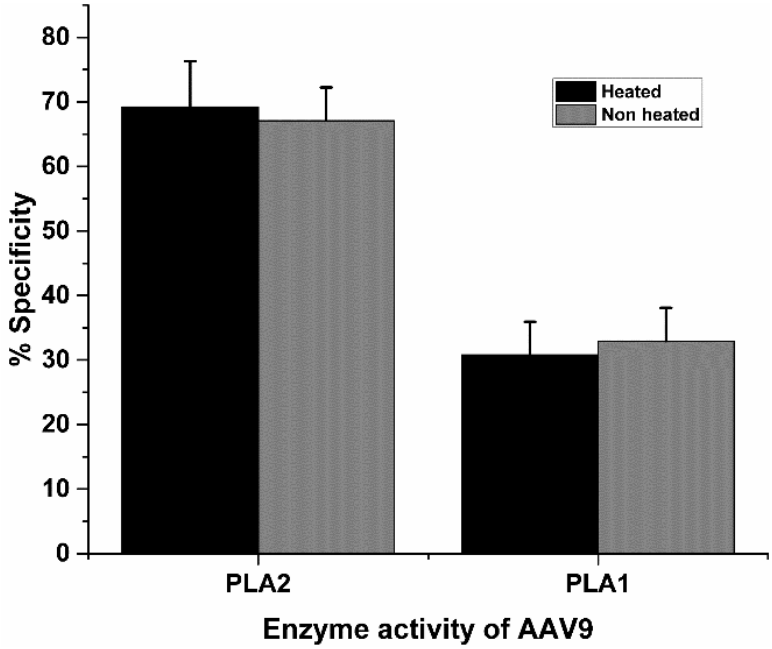


Figure S3. Comparison of the % specificity of the cleaved product generated by heat activated and non-heated activated (prolonged incubation) AAV9 lipase. Both specific PLA2 and non-specific PLA1 products are observed.

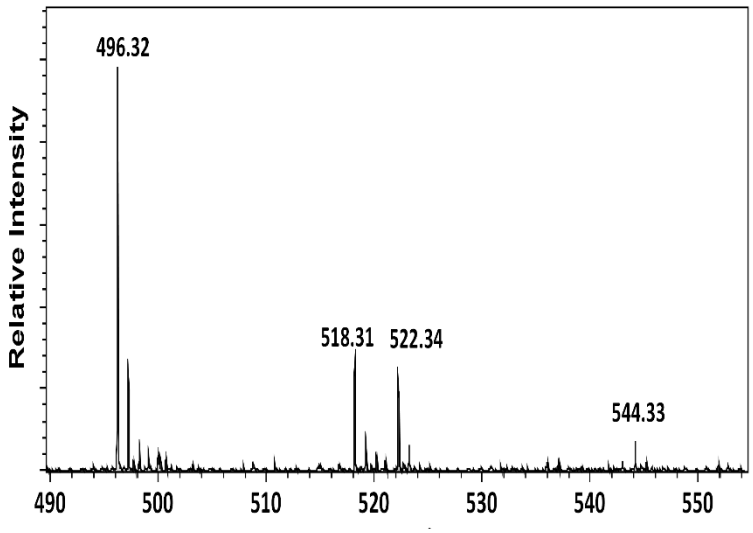


Figure S4. ESI-MS spectrum of mixed lipase products generated by heat activated AAV9 lipase.